



**SHOCK WAVE DYNAMICS OF NOVEL ALUMINIZED DETONATIONS
AND EMPIRICAL MODEL FOR TEMPERATURE EVOLUTION
FROM POST-DETONATION COMBUSTION FIREBALLS**

DISSERTATION

J. Motos Gordon, Lieutenant Colonel, USAF

AFIT/DS/ENP/10-S03

**DEPARTMENT OF THE AIR FORCE
AIR UNIVERSITY**

AIR FORCE INSTITUTE OF TECHNOLOGY

Wright-Patterson Air Force Base, Ohio

APPROVED FOR PUBLIC RELEASE; DISTRIBUTION UNLIMITED

The views expressed in this dissertation are those of the author and do not reflect the official policy or position of the United States Air Force, Department of Defense, or the United States Government.

AFIT/DS/ENP/10-S03

SHOCK WAVE DYNAMICS OF NOVEL ALUMINIZED DETONATIONS
AND EMPIRICAL MODEL FOR TEMPERATURE EVOLUTION
FROM POST-DETONATION COMBUSTION FIREBALLS

DISSERTATION

Presented to the Faculty

Graduate School of Engineering and Management

Air Force Institute of Technology

Air University

Air Education and Training Command

In Partial Fulfillment of the Requirements for the

Degree of Doctor of Philosophy

J. Motos Gordon, B.S., M.Mtl.E.

Lieutenant Colonel, USAF

March 2011

APPROVED FOR PUBLIC RELEASE; DISTRIBUTION UNLIMITED

SHOCK WAVE DYNAMICS OF NOVEL ALUMINIZED DETONATIONS
AND EMPIRICAL MODEL FOR TEMPERATURE EVOLUTION
FROM POST-DETONATION COMBUSTION FIREBALLS

J. Motos Gordon, B.S., M.Mtl.E.
Lieutenant Colonel, USAF

Approved:

Glen P. Perram, PhD (Chairman)

Date

Kevin C. Gross, PhD (Member)

Date

Charles E. Browning, PhD (Member)

Date

Accepted:

M. U. Thomas
Dean, Graduate School of Engineering
and Management

Date

Abstract

Optical forensics of explosion events can play a vital role in investigating the chain of events leading up to the explosion by possibly identifying key spectral characteristics and even molecules in the post-detonation fireball that may serve as the fingerprint for a particular explosive type used. This research characterizes the blast wave and temperature evolution of an explosion fireball in order to improve the classification of aluminized conventional munitions based on a single explosive type such as RDX.

High speed 4 kHz visible imagery is collected for 13 field detonations of aluminized novel munitions to study fireball and shock wave dynamics. The 238 μ s temporal resolution visible imagery and the 12 ms temporal resolution FTS spectra are the data sets upon which shock wave dynamics and the time dependence of the fireball temperature are studied, respectively. The Sedov-Taylor point blast theory is fitted to data where a constant release ($s = 1$) of energy upon detonation suggests shock energies of 0.5–8.9 MJ corresponding to efficiencies of 2–15 percent of the RDX heats of detonation with blast dimensionalities indicative of the spherical geometry observed in visible imagery. A drag model fit to data shows initial shock wave speeds of Mach 4.7–8.2 and maximum fireball radii ranging from 4.3–5.8 m with most of the radii reached by 50 ms upon detonation. Initial shock speeds are four times lower than theoretical maximum detonation speed of RDX and likely contributes to the low efficiencies. An inverse correlation exists between blast wave energy and overall aluminum or liner content in the test articles. A two-color best fit Planckian is used to extract temperature profiles from

collected Fourier-transform spectrometer spectra. The temperatures decay from initial values of 1290–1850 K to less than 1000 K within 1 s after detonation. A physics-based low-dimensionality empirical model is developed to represent the temperature evolution of post-detonation combustion fireballs. Using a radiative cooling term and a secondary combustion term, the model is able to reduce 82 data points down to five fit parameters. The fit-derived heat of combustion has a 96% correlation with the calculated heat of combustion but has a slope of 0.49 suggesting that only half of the theoretical heat of combustion is realized. Initial temperature is not a good discriminator of detonation events but heat of combustion holds promise as a potential variable for event classification. This model and corresponding analyses might improve the ability of sensing platforms to identify explosive types and sources.

I dedicate this dissertation to my wife, daughter, sister, mom, dad, Nanay & Tatay, Grandma & Grandpa, Tita Clemen, Tita Lita, and God. Thank you for all your love, support, and sacrifices. I will never forget where I came from, how I got here, and how lucky I am to have you all in my life.

Acknowledgments

I wish to thank my wife and daughter for their incredible love and support and for always believing in me. Although I was not always at home, their love, smiles, laughter, encouragement, and snacks were always with me. I know deep in my heart that I could not have succeeded without them. I am indebted to Dr. Glen Perram for his guidance, support, and patience in getting me through the trials and tribulations of this program. He has been a towering example in the academic arena and life in general and has also given me a new-found respect for the power of experience and scientific intuition. I extend my gratitude to the other committee members, Dr. Charlie Browning and Dr. Kevin Gross, for their invaluable support and assistance. I am grateful to Dr. Gross for guiding me through the dizzying and oft painful nexus that is Matlab and physics. I am appreciative of our many discourses both light and weighty whether they be at the airport, office, or field. Dr. Bill Baker is to be thanked for helping me understand the mathematical insights in this work. Thanks are extended to AFIT technician Greg Smith for his expert troubleshooting skills during the signatures acquisition of the tests and to AFRL's Wayne Richards for letting us observe his detonation tests and allowing me to collect some free photons that he "wasn't going to use anyway." My fellow students (among them Joel Anderson, Monte Anderson, Spencer Bowen, Chris Rice, Dean Roberts, Bryan Steward, and Cliff Sulham) are to be thanked not only for their help, but for their kind friendship as well. To the Giants upon whose proverbial shoulders we can all stand, thank you for letting me see another layer of beauty that is underneath all things great and small.

J. Motos Gordon

Table of Contents

	Page
Abstract	iv
Dedication	vi
Acknowledgments	vii
Table of Contents.....	viii
List of Figures	xi
List of Tables.....	xv
List of Acronyms	xvi
I. Introduction.....	1
Document Preview	4
II. Background.....	6
1. Classification of Detonation Events.....	6
2. Phenomenology of an Explosion	15
III. Temporally-Resolved Infrared Spectra from Detonation of Advanced Munitions	21
Overview	21
1. Introduction	21
2. Experimental	24
3. Analysis.....	28
4. Conclusions	35

	Page
IV. Fireball and Shock Wave Dynamics in the Detonation of Aluminized Novel Munitions	36
Overview	36
1. Introduction	36
2. Experimental	40
3. Image Processing.....	43
4. Results and discussion	46
4.1. Shock wave analysis	46
4.2. Influence of liner and aluminum on detonation energy.....	55
4.3. Fireball dynamics	60
5. Concluding remarks	63
V. Evolution of Fireball Temperature after the Detonation of Aluminized RDX	65
Overview	65
1. Introduction	65
2. Experimental setup and explosive materials	67
3. Results	73
3.1. Spectra	73
3.2. Temperature dynamics	78
3.3. Fireball Rise.....	84
4. Conclusions	88
VI. High Speed Spectral Measurements of IED Detonation Fireballs	90
Overview	90
1. Introduction	90
2. Experimental	93
3. Results and Discussion.....	96
4. Conclusions	104

	Page
VII. Conclusion.....	105
1. Summary of Key Findings	105
2. Concluding Discussion of Key Findings	107
3. Future Efforts	108
Appendix A. Empirical Model Fit to Data	110
Appendix B. Gross Radiative Transfer Spectral Model Fit to Data	117
Appendix C. Theory	122
1. Spectrometer Basics	122
2. Source of Blackbody Radiation	124
3. Shock Wave Phenomenon	126
Appendix D. Sample Calculation	130
1. Heat of Detonation (RDX only HE)	130
2. Heat of Combustion (PE-Al Liner + RDX-Al-wax HE).....	131
Bibliography	133
Vita	139

List of Figures

Figure	Page
1. Aerial view of the AWEF test range. The blast arena where the test items were detonated is highlighted by the concentric rings at the top of the inset schematic.....	25
2. Left to right, the ABB-Bomem MR-254 FTS, CI Systems ColoRad radiometer, and pair of Phantom 5.1 and 7.1 cameras. Each is peering through a hole from behind thick iron armor shielding. A plywood roof was subsequently installed to shield the instruments from heating via direct sunlight, thereby minimizing the effects of self-emission in the InSb channel of the FTS and the InSb and HgCdTe channels of the radiometer.....	25
3. Overview of the radiometric, spectro-radiometric, and high-speed imagery collected from an aluminized RDX fireball. <i>Top-left panel:</i> Band-integrated radiometric response of the InSb channel of the CI Systems ColoRad radiometer. <i>Top-right panel:</i> Same band-integrated radiometric profile shown on a log-log scale. Open circles indicated the times corresponding to the spectra and imagery shown in the bottom panels. <i>Bottom-left panel:</i> Time-evolution of the MWIR spectra captured by the ABB-Bomem MR-254 FTS. <i>Bottom-right panel:</i> Color imagery captured by the Phantom v7.1 camera. A majority of the pixels illuminated in the first frame were saturated.....	27
4. Time-resolved spectral data cubes for the first 0.5 s of a low-Al (a) and high-Al (b) RDX detonation fireball. Effects of detector response (gain) have been accounted for and the scale for the ordinate axis is the same in both plots.....	29
5. Normalized spectra corresponding to RDX containing low (—) and high (—) aluminum content at (<i>top</i>) 0.2 s and at (<i>bottom</i>) 0.6 s. At early times, both spectra are dominated by continuum radiation from the soot. As time progresses, the high-Al RDX exhibits more selective emission near 2100, 3200, and 4950 cm ⁻¹	32
6. (<i>top</i>) Peak-normalized emissivity-area and (<i>bottom</i>) temperature curves for the low-Al and high-Al RDX fireballs obtained by fitting a Planckian distribution to spectral regions free from selective emission (4400–4700 and 5800–6500 cm ⁻¹).....	33
7. Schematic of the Advanced Warhead Experimentation Facility (AWEF).	40

Figure	Page
8. Weight fractions for: (○) liner, (□) aluminum in both liner and HE, (●) RDX, and (■) binder.....	42
9. (a) Visible image for event E8 13 ms after detonation with 8 bit scale for intensity. (b) Image processed by taking the \log_{10} of the frame-differenced image. (c) Intense pixels of the fireball (gray) and dark pixels of the soot (black) within the rectangular windowed selection. (d) Histogram of the image showing 8-bit digital number range ($1-2^8$) of gray-scale pixel intensity levels of various features.....	44
10. Fireball from event E7 at: (a) $t = 0.30$ s with a fireball radius of 6.13 m and (b) at $t = 0.35$ s, with a rise relative to the blast origin of 13.5m.....	45
11. A fit of the (—) blast model and (---) exponential drag model to the (●) shock front radius, R_s , and (○) fireball radius, R_f , for event E7. The annotated mid-field region indicates the general range of data points within which the Sedov-Taylor blast theory model was fit. Note the approximate time and corresponding distance at which the shock wave detaches from the fireball.....	47
12. Log-log plot of shock expansion and the two-parameter power law fit for events (□) E11, (*) E13, and (○) E15 showing relative spread of the blast model fits for $t=0-20$ ms.....	50
13. Dependence of shock parameters: (●) energy efficiency, η , and (○) dimensionality, n , on fraction of weight allocated to high explosive for constant energy release, $s = 1$	55
14. Dependence of shock parameters: (●) energy efficiency, η , and (○) energy release factor, s , on fraction of weight allocated to high explosive for spherical expansion, $n = 3$	56
15. Scaling of detonation energy with (●) HE and (○) aluminum weight fractions for (a) $s = 1$ and (b) $n = 3$	58
16. Influence of aluminum content for events with (●) no liner and (○) 17–22% liner by weight.....	59
17. (●) Initial velocity and (○) stopping distance for the emissive fireball.....	62
18. Temporal evolution of fireball : (○) radius and (●) loft height at longer times. The fireball rise begins to approach a constant rate beginning at approximately 0.25 s.....	63

Figure	Page
19. (a) Temporally-resolved spectra for event E9, and (b) the FTS observed spectral intensity (\blacksquare) of event E9 at 0.28 s after detonation. Two spectral regions: 2500–2700 and 4500–4700 cm^{-1} , of continuum radiation are indicated for the two-color temperature determination. A fit of the observed spectra (—) to the radiative transfer model of Eq. (15) yields fit residuals of $\sim 3.7\%$, except in the vicinity of the CO_2 4.3 μm band.....	73
20. Comparison of temperature profiles derived from: (---) the spectral model of Eq. (15) and (—) the two-color Planckian method for events: (—) E9, (—) E4 and (—) E17.....	76
21. Ratio of band integrated intensities for the regions 2500–2700 and 4500–4700 cm^{-1} as a function of temperature. The intensity ratio for event E9 specifies a temperature of $T = 1828 \text{ K}$. Linearity of the relationship implies the fractional error in temperature is the same as the relative error in the observed intensity ratio, assuming blackbody behavior within the first 1 s after detonation.....	77
22. (\blacksquare) Temperature profile observed for event E9 and (—) fit of the numerical solution to Eq. (17) yielding the fit parameters provided in Table 10.....	79
23. Scatter plot between empirical model predicted initial temperature and initial temperature predicted from thermodynamic properties. Lack of correlation suggests initial temperature is not a good variable for event classification.....	81
24. Correlation between predicted and observed heats of combustion with slope of 0.49 ± 0.1 and correlation coefficient of $r = 0.96$	82
25. Dependence of observed heat of combustion on fraction of volume allocated to the liner, indicating correlation of $r = 0.93$	82
26. Scatter plot illustrating no significant relationship between combustion fit parameters and efficiency for converting heat of detonation into shock expansion.....	83
27. Relationship between lofting rate and (\square) T_o and (\bullet) combustion fit parameters.....	86

Figure	Page
28. Unobstructed line-of-sight view of the test range from the instrumentation, matched to an overhead schematic of the site.....	92
29. Sequence at ground-zero showing signal obscuration immediately after detonation. Optical attenuation from dust resulted in relatively weak infrared signatures reaching the FTS at the standoff distance of 1.5 km...	97
30. Raw spectra from the two infrared FTS channels for Event 4a. (The spectral response of the individual detectors have not been removed from the data.) The real and imaginary components are denoted Re and Im, respectively. <i>Top panel</i> : LWIR (left) and MWIR (right) spectra immediately after detonation. <i>Bottom panel</i> : LWIR (left) and MWIR (right) spectra 122ms after detonation.....	99
31. Waterfall plots of the un-calibrated MWIR (InSb) spectra for Event 4a (left panel) and Event 5 (right panel). Again, note the rapid decrease in relative intensity of the Event 4a HME. While the spectra are un-calibrated, both events were collected under identical instrument conditions, permitting relative intensity comparisons.....	99
32. Comparison of measured signatures for the same detonation event (Event4a –10 kg of a specific HME). <i>Top-left panel</i> : visible image from witness camera. <i>Top-right panel</i> : MWIR FLIR thermal image. <i>Bottom-left panel</i> : Time sequence of MWIR FTS spectra. <i>Bottom-right panel</i> : comparison of integrated intensity and its semi-log equivalent from InSb channel of radiometer.....	103
33. General schematic of a typical Michelson interferometer.....	123
34. Early Planckian behavior of a detonation event. Note the circular reticle in the bottom plot of the integrated intensity indicating the temporal location of the above Planckian spectra.....	125
35. Typical compressive stress-strain curve to very high stress level.....	126
36. Pressure wave (or shock wave) at high pressure.....	127

List of Tables

Table	Page
1. Summary of previous research.....	7
2. Listing of some constituent materials and nominal quantities for 22 test items.....	23
3. Composition of test articles.....	41
4. Meteorological conditions	43
5. Fit parameters from shock expansion and fireball drag.....	49
6. Interpretation of shock dynamics.....	51
7. Interpretation of fireball dynamics.....	60
8. Composition of test articles.....	68
9. Thermodynamic properties of test articles.....	68
10. Fit parameters for numerical solution to Eq. (17).....	80
11. Comparison of fit parameters to thermodynamic predictions.....	85
12. Summary of manufactured HMEs and AFIT's data acquisition instruments. The peak temperature and time-to-peak columns were based on an analysis of calibrated, high-speed radiometric measurements made by the CI Systems radiometer.....	94

List of Acronyms

Acronym	Description
AFIT	Air Force Institute of Technology
AFRL	Air Force Research Laboratory
Al	Aluminum
ALE3D	Arbitrary Lagrangian-Eulerian 3-Dimensional
AWEF	Advanced Warhead Experimentation Facility
BB	Blackbody
CHAS	Chemical and Hydrodynamic Analysis Schemes
CVIF	Circular Variable Interference Filter
ENE	Enhanced Novel Explosive
FORTTRAN	Formula Translator
FOV	Field-Of-View
FTIR	Fourier Transform Infrared Spectroscopy
FTS	Fourier Transform Spectrometer / Spectroscopy
GP	General Purpose
HE	High Explosive
HME	Homemade Explosive
IED	Improvised Explosive Device
IR	Infrared
IVIE	Intense Visible and Infrared Emission
LWIR	Long-wave Infrared
MWIR	Mid-wave Infrared
MCT	Mercury-Cadmium-Telluride; HgCdTe
MODTRAN	Moderate Transmission
NFTU	Naturally-Fragmenting Test Unit
NIR	Near Infrared
OPD	Optical Path Difference
PDC	Post-Detonation Combustion
PDPC	Post-Detonation Particulate Cloud
PLEXUS	Phillips Laboratories Expert User Software
RDX	Research Development Explosive
RMSE	Root Mean Square Error
SPIE	International Society of Optical Engineering
TMD	Theoretical Maximum Density
Chemical	Common Name
C ₃ H ₆ N ₆ O ₆	RDX, Cyclo-1,3,5-Trimethylene-2,4,6-Trinitramine
C ₂ H ₄	Polyethylene
C ₂₅ H ₅₂	Paraffin wax
HgCdTe	MCT, Mercury-Cadmium-Telluride
InGaAs	Indium-Gallium-Arsenide
InSb	Indium-Antimonide
TNT	Trinitrotoluene

SHOCK WAVE DYNAMICS OF NOVEL ALUMINIZED DETONATIONS
AND EMPIRICAL MODEL FOR TEMPERATURE EVOLUTION
FROM POST-DETONATION COMBUSTION FIREBALLS

I. Introduction

The explosion of a conventional munition represents an intense visible and infrared emission (IVIE) event. The emitted radiation are signatures that can reveal a wealth of information regarding the explosion. Visible signatures can provide clues about the extent of the fireball and even the energy of the explosion [60]. Richer still, infrared spectral signatures can harbor information such as the type or class of explosive, the constituents of the explosive, the temperature of the detonation, and also the energy released. It is little wonder, then, that such IVIE event signatures are increasingly becoming the cornerstone of recent efforts in the optical forensic and classification of battlespace detonation events.

Robust classification of detonation events is predicated on the fundamental understanding of the physical phenomenology involved. However, methods are needed that do not require large amounts of time or extensive computational resources such as those found in ab initio chemical and hydrodynamic analysis schemes (CHAS) like the CHEETAH or Arbitrary Lagrangian-Eulerian 3-Dimensional (ALE3D) codes from Lawrence Livermore National Laboratory. For optical forensics, a departure from CHAS to phenomenological models is desired. Recently, feature discrimination techniques and physics-based models have been able to differentiate between disparate explosive types

and configurations and even static versus air-dropped munitions. Despite recent advances, the ability to differentiate between spectral features from very similar classes of explosives (i.e., RDX-based) has proven difficult. An additional avenue to the classification effort is needed.

The incorporation of chemical kinetic phenomena into the classification scheme may provide the key to higher fidelity discrimination of spectral features. The data used in the present research are the most temporally rich infrared spectral signatures available to date on the field detonation of conventional munitions. As such, these signatures offer the possibility of exploring the kinetics between spectral features and event classification.

A phenomenological model has recently been developed by Gross [28] to describe the observed spectra of the detonation fireball event. The Gross spectral model's ability to identify and extract spectral features is fairly robust. It provides fireball emissive area, temperature, particulate absorption coefficient, as well as H_2O and CO_2 concentrations. The present work is part of a research effort to gain a greater understanding of the chemical kinetic picture of a detonation event by bringing several physics-based models to bear on the problem. The 12 ms temporal resolution Fourier-transform infrared spectrometer (FTS) spectra as well as the 238 μs temporal resolution visible imagery are the data sets upon which shock wave dynamics and the time dependence of the fireball temperature are studied in the present research.

This research effort will develop and use a new low-dimensionality physics-based empirical model to characterize the temporal temperature evolution of post-detonation combustion fireballs to further understand the chemical kinetic picture of explosions for improved event classification. While identification and extraction of spectral features has

been studied previously, the time dependence of the fireball temperature and its relation to chemical kinetic reaction rates has not been incorporated into current classification schemes. The present research is an important step towards the leveraging of chemical kinetic phenomenology to help address the problems of event classification.

Temporally-Resolved Infrared Spectra from the Detonation of Advanced Munitions

The first part of this work involves the collection of visible and infrared signatures of field detonation events and their initial analysis. Conditions of the test event and test articles as well as equipment calibration are discussed. The current spectral model is used to provide a first-look at the spectral intensity, emissive area, temperature profile, and overall behavior of the fireball. Visible imagery is used to provide an initial look at the fireball and shock wave behavior of the detonation events. The resulting data and analysis were accepted for publication [26] and presented at the SPIE Defense, Security, Sensing Conference in April 2009 and are presented in Chapter III.

Fireball and Shockwave Dynamics in the Detonation of Aluminized Novel Munitions

The next step in understanding the temporal dependence of temperature involves the analysis of the explosion fireball and shock wave from high speed visible imagery. The drag model and Sedov-Taylor point blast model are used to analyze the fireball and shock wave fronts, respectively. Fireball size and rate of ascent is studied and shock wave analysis provides an estimate of the blast wave energy, dimensionality, and energy release profile. The key results of this phase of the present research are the estimates of the fireball area and the energy conversion efficiency as this latter quantity may be related to the post-detonation combustion of an explosion event. Results from this analysis are presented in Chapter IV.

Evolution of Fireball Temperature after the Detonation of Aluminized RDX

Lastly, a new low-dimensionality, physics-based empirical model is created that is able to characterize the temporally-resolved temperature profiles of post-detonation combustion fireballs. It uses radiative cooling and exponential combustion source terms to reduce 56–82 data points down to only five fit parameters. This new model introduces the possible role of chemical reaction rates into the classification picture and is an approach that has not been done to date. Correlations to physical quantities and phenomena further bolster confidence in the model fit parameters. Coupled with the current spectral model, this empirical model and its physics-based approach might be used to examine future, and even previous, spectral signatures to enhance the kinetic picture of field detonation events and consequently improve current classification schemes. The empirical model analysis of the post-detonation combustion fireball is presented in Chapter V.

High Speed Spectral Measurements of IED Detonation Fireballs

As an extension to the present work, homemade explosive detonation signatures are collected and analyzed. High speed mid-wave thermal imagers augment the standard visible, radiometric and FTS data set. Rapid signal attenuation from ground dust ejecta severely limits the spectral analysis with the early times offering the only robust means within which to characterize the detonation fireball. Findings were accepted for publication [27] and presented at the SPIE Defense, Security, and Sensing Conference in April 2010 and are presented in Chapter VI.

II. Background

Detonation fireball phenomena and the detection of their spectral signatures are both complex subjects. A quick review of some key fundamental concepts essential to understanding the detonation event is discussed in Appendix C. This chapter reviews the relevant previous research on the extraction, identification, and classification of spectral features of high explosive (HE) detonation events and also provides an overview of the phenomenology of an explosion.

1. Classification of Detonation Events

In the past 30 years, numerous studies have been performed to examine and extract spectral features from explosion events. Recent efforts have been focused on the development of analytical models and classification schemes to improve the optical forensics of battlefield detonation events. Table 1 details previous work in this area and is followed by narrative summaries of the respective approaches and findings.

A 1980 study by Herr, Stone, and Urevig [34] from The Aerospace Corporation for Sandia National Laboratory looked at the long-wave infrared (LWIR) spectroscopy of HE detonations. A total of 19 detonations ranging from 18 kg to 100 kg of C-4 or plastic bonded explosive LX-O7(90% HMX, 10% Vitron) HE were observed. The containment materials used were bare charges, aluminum, steel, and uranium. The fielded spectrometer was designed by Aerospace Corporation and had both an imager and a spectrometer [34, p. 4] that employed a 60-element mercury-cadmium-telluride (MCT) detector array that covered the 4–14 μm spectral range. Only 12 of the 60 MCT array elements were used for the tests. The instrument was also fitted with a circular variable interference filter (CVIF) that converted the imager into a multi-detector

spectrophotometer. Its scan rate was 0.5–1 Hz at a spectral resolution ($\Delta\lambda/\lambda$) of 0.01.

Using the CVIF and the MCT detector array, they concluded the following:

Table 1. Summary of previous research on characterization of detonation fireballs

Year/Ref.	Instrumentation							Main Features						Methodology						
	CVIF	FTS (MR-154/-254)	Grating Spectrometer	Radiometer	High Speed Video	IR Imaging Camera	Visible CCD Camera -XL1	Feature at 2100-2200 cm ⁻¹	Detonation Zone	Spectral Radiance Profile	Fireball T(t) Profile	Fireball Area Profile	Soot / H ₂ O-CO ₂ conc.	Probable Time to Peak	Infrared Region	Overlap analysis	Fractional Field-of-View	Fisher & Bayesian Analysis	Nonlinear Regression Fit	Dimensionally Reduction
1980 [34]	●					●		●			●				L					
1981 [51]	●			●	F	●									L					
2000 [46]		● ¹						●	●		●	●			M	●				
2001 [3]		● ¹									●				M		●			
2003 [47]		● ¹						●			●	●			M	●				
2003 [18]		● ¹				●	●			●		●			M	●				
2003 [29]		● ¹								●					M				●	●
2004 [20]						●								●	N			●		
2005 [19]						●	●							●	N			●		
2005 [31]		● ¹						●							M				●	●
2005[17]						●	●							●	N			●		
2007 [32]		● ¹	●	●		●	●			●	●	●	●		M	●			●	●
2007 [28]		● ^{1,2}		●	D	●				●	●	●	●		M	●			●	●
2008 [30]		● ¹						●		●	●	●	●		M	●			●	●

●¹— MR-154 FTS ●²— MR-254 FTS ●^{1,2}— MR-154 & MR-254

D — Digital (Phantom) F—Film L—LWIR M—MWIR N—NIR

1. A temperature profile was recorded for an 18 kg bare charge at 11.1 μm wavelength with 16 ms temporal resolution. They extrapolated the maximum temperature at 840K from the available data. They observed a fluctuation in the initial part of the temperature and attributed this to “acoustically induced mixing of the fireball reaction zone by the returned ground shockwave” [34, p.46]. After 200 ms, the “cooling rate matched a theoretical T^4 radiation law profile suggesting radiative cooling is the major loss mechanism” [34, p.48].

2. A broad emission spectrum centered at 1095 cm^{-1} that dominated each spectrum was ascribed to atmospheric dust stirred up by the detonation or already present in the atmosphere. Several features were observed near $10\mu\text{m}$ (1000 cm^{-1}) which were attributed to CO_2 emission.
3. An intense emission feature was observed at 2150 cm^{-1} which was most predominant in the steel or uranium confined test items. This feature was assigned to the CO transition.
4. Spatial investigations of the spectroscopy led to the conclusion that the basic chemistry on the fractional-second timescale does not vary appreciably with position in the fireball. Only the intensity of the background emission varies.
5. A very interesting feature occurs at 870 cm^{-1} and is tentatively assigned to hydrogen peroxide (H_2O_2) or possibly nitric acid (HNO_3).

A 1981 study called Mini-Puff by Rogers et al. [51] at Sandia National Laboratory followed-up the earlier work by Herr et al. [34] and observed LWIR spectra from 23 HE detonations. Herr et al. used C-4, TNT, 9501, and 9502 explosive materials while Rogers et al. only used TNT and 5901 in their tests. They used the same instruments as the previous study but with a modified CVIF capable of 10 Hz scan rates and the inclusion of a broadband radiometer in the instrument suite. Rogers et al. described the detonation event as consisting of an initial burn phase attributed to the HE detonation and a subsequent afterburn likely commensurate with the combustion of an under-oxidized HE upon completion of the burn phase. Containment materials were steel and aluminum at two different thicknesses. They used the broadband radiometer to determine spectral radiance and they used high-speed film to characterize shock-front as a function of time. However, given the quality of their film data they determined that radiometric technique was a simpler method to characterize fireball size using time to the burn peak. They concluded their study with the following key points [51, p. 78-80]:

1. The radiometers indicated that the radiance of the afterburn phase was not consistent from shot to shot. They attribute this to the randomness of the turbulent mixing from the atmosphere. However, the burn phase “appears to be consistent, well-behaved, and probably subject to reasonably good theoretical interpretation...and therefore thought to be more fruitful in yielding information about the type of high explosive material and/or the containment material than spectra of the afterburn” [51, p. 78].
2. Absorption features, likely from NH_3 , were observed in all 7.00 to 12.42 μm spectra where C-4 was the HE and were not observed in the spectra of other HE materials.
3. Observations of water vapor and CO_2 in emission did not correlate with explosive material, containment material, or peak temperature of the afterburn.
4. The array spectrometer appears to be particularly well suited to the task of spectral measurement of explosive detonations.
5. They mentioned that the spectral radiance from a particular molecular species depends upon more than just the quantity and temperature of the respective molecular species. It strongly depends on the surrounding molecules and background (which might be the other products of the HE detonation). In other words, a quantity of gas at a certain temperature will not have any detectable spectral signature if the background is a blackbody at the same temperature.
6. The relative radiance of the burn and afterburn phases depends strongly on the type of HE material. The combustion of oxygen-rich HE materials is nearly complete during the burn phase and its radiance at the peak of burn phase is thus stronger than the afterburn phase. On the other hand, oxygen-poor HE materials such as TNT and C-4 are not fully combusted at the burn phase but are so in the afterburn phase. Thus, their afterburn radiance is as bright as or brighter than the burn phase radiance and also lasts much longer.
7. The peak radiance during both the burn and afterburn is reduced by containment.
8. The time of the radiance peak in the afterburn is also delayed by containment.
9. Based on a limited statistical sample of identical test items, it appears that the peak radiance of the burn phase was consistent from shot to shot, but the afterburn was extremely inconsistent. This was ascribed to the randomness in the turbulent mixing with ambient air.

The Air Force Institute of Technology (AFIT) fielded rapid-scan Fourier-transform spectrometers, radiometers, and high-speed imagers to various test ranges to remotely collect post-detonation combustion (PDC) signatures from detonations of various $C_yH_wN_xO_yAl_z$ -based high explosives. From 1998 to the present, the focus of prior research by AFIT and others has been on interpreting the spectral signatures for the purpose of understanding event phenomenology. What follows is a brief summary of key findings and conclusions of these prior studies.

Orson, Bagby, and Perram [47] observed 56 detonation events during the RADIANT BRASS tests and used temperature, fireball area, and spectral temporal overlap to discriminate between explosion types. They found that emissive area provided a more sensitive signature of the detonation events than did the temperature profile. However, it was their use of the degree of temporal overlap as a function of frequency between detonation events that provided a very sensitive discriminator of these events [47; 46, p.67]. They concluded that “temporally and spectrally resolved infrared emissions from bomb detonations provide unique signatures that may be utilized to classify event type and conditions”.

In his Master’s thesis, Orson used the time evolution of band integrated radiance or intensity to characterize detonation signatures. He defined these temporal profiles or patterns as mode one (an initial spike followed by a smaller maximum and then a gradual decay) and mode two (no presence of an initial spike, only a maximum followed by a gradual decay). He concluded with six observations paraphrased below regarding the RADIANT BRASS detonation signatures [46, p. 85]:

1. Event signatures for small-sized (45.4-181.4 kg), type A explosive (C-4: 91% RDX, 9% Plasticizer) were repeatable. Event signatures for large sized (>272 kg), type B explosive (H-6: 45.1% RDX, 29.2% TNT, 21 Aluminum, 4.7% Wax), no conclusive statement about repeatability could be made.
2. Spectral signatures produced by air dropped ordnance are not uniform within a 360 degree viewing angle of the detonation zone; implying the detonation zone is anisotropic.
3. All detonation signatures can be primarily described as decaying gray bodies where the gray body is a function of wavenumber.
4. The distinctive emission during afterburn in the 2100–2200 cm^{-1} frequency range discriminates between explosive A and explosive B. This same frequency range showed discrimination between explosive A, B, and C (100% RDX). His overlap analysis supports the conclusion that higher frequency spectra better discriminate look angle and explosive type.
5. A medium-framing rate (20 Hz – 50 Hz) is adequate to temporally distinguish bombs in the battlespace.
6. The collective information from conclusions 1–5 above indicates that identification of explosives and event conditions in the battlespace is possible.

Bagby's Master's thesis [3] followed-up the work of Orson. Bagby used the RADIANT BRASS 3B subset of data which consisted of only the 23 statically detonated events and did not include the air-dropped munitions. He used PLEXUS and MODTRAN to account for atmospheric transmittance and proceeded to write FORTRAN and Mathematica codes to computationally characterize the temperature profiles and fractional field-of-view (FOV) profiles of the detonations. He used the time evolution patterns from Orson's work to examine the temperature evolution of the explosion events. His analysis verified Orson's assumption of treating detonation events as decaying graybodies. Bagby found "large type B detonations were clearly identifiable by distinct afterburn feature in the temperature profile at approximately 0.5 s after bomb initiation" and that they "consistently displayed the afterburn feature from 0.75 to 1.00 s

in the temperature profile...followed by a steady decay out to 5 s” [3, p. 65]. From the FOV profiles, he showed that type B explosive events indicated a peak value corresponding with event initiation followed immediately by a distinct drop-off and steady value. On the other hand, type A explosive events showed a steady profile without an initial peak. Root mean squared error (RMSE) analysis showed the same time mode as its associated temperature profile. [3, p. 69]

Gross, Perram, and Tuttle [31] took a subset of 15 of the 56 observed detonations acquired by Orson et al. from the RADIANT BRASS tests and attempted to model infrared spectral intensity. They found that in the midwave IR, an attenuation-modified, single temperature Planckian distribution adequately models the spectral intensity to within a few percent on average. They found that fit residuals for a non-Planckian, strong spectral emission in the 2000–2200 cm⁻¹ window “was the best feature for graphically discriminating between the two classes of air dropped munitions” that were composed of two chemical compositions. They concluded that the key to the classification problem was better understanding of the non-Planckian behavior due to emissions from select molecules. They developed a simple and robust method for estimating the atmospheric transmittance function and reduced the dimensionality of the data to a set of two time-dependent fit parameters [T(t) and εA(t)] while preserving much of the original fidelity. They modeled the observed detonation spectral intensity as [31]:

$$I_{obs}(\tilde{\nu}, t) = \tau(\tilde{\nu})[\varepsilon A(t)] \frac{2hc^2\tilde{\nu}^3}{e^{hc\tilde{\nu}/k_B T(t)} - 1}$$

In the BRILLIANT FLASH I field tests, Dills, Perram, and Gustafson [19, 20] used near infrared (NIR) visual imagery to classify the detonations of TNT and four other

enhanced explosives mixtures, using only the 50 kg test items. Since no physical models existed for their data, they instead opted to use a second-order polynomial to fit the most common feature in the observed data: the downward curvature of the plots. Using Fisher discrimination techniques, they took fourteen extracted features from the data and determined the best ones to distinguish the five explosives types. They found that the three features that can “optically classify two of the five types of explosive materials...are the most probable time (to peak area) and the two fit coefficients that describe the decay of fireball size with a second-order polynomial” [20].

Dills et al. [19] then augmented their previous study by using visual imagery from the same tests that were conducted in BRILLIANT FLASH I. Specifically, they used the red, green, and blue imaging chips in a Canon XL1 video camera and applied the same statistical approach. They once again used Fisher linear discriminant techniques and Bayesian decision boundaries on several factors including the various explosive classes and features such as fireball size and time to peak of the fireball size in order to find the best discriminator for event classification. Using these statistical tools on key image features of the detonation resulted in probability densities that could be exploited to find differences between certain explosive types. From their imagery data, they concluded that “the single best feature for classification between uncased conventional TNT and ENE materials is the time to peak of the fireball size in the infrared...yielding approximately 90% accuracy in robust testing of explosive type probability densities,” regardless of whether the weight of the explosive is known. Additionally, “maximum fireball size gave similar performance in the blue band of the visual imagery.”

In a subsequent study, Gross, Wayman, and Perram [32] analyzed IR spectra collected from BRILLIANT FLASH II test detonations of uncased charges of TNT and several kinds of improvised explosive devices (IEDs) which they termed enhanced novel explosives (ENEs). They characterized the observed spectra using time-resolved fit parameters and derived quantities for the fireball size, temperature, gray particulate (i.e., soot) absorption coefficient and transmission value, gaseous by-product concentrations, total quantity of hydrogen and carbon compared with expected values, and the ratio of hydrogen and carbon amounts compared with theory. Comparing their fits to NIR imagery obtained from another study, they concluded that “fireball size can be estimated from a well-calibrated, non-imaging FTS”. Further, they found that R (the ratio of H:C concentration) was a useful discriminant as it could provide information about the HE starting material. Using R , they were also able to differentiate between TNT and ENE explosives. However, they found that R was not able to easily discriminate between ENEs with similar H:C ratios in their HE material. They concluded that the values for ENE explosives “display interesting kinetic behavior suggesting that R conveys more information than just the limiting thermodynamic behavior”. This last conclusion is of great interest for this present research as it suggests a possible avenue of approach. In short, their simple physics-based phenomenological fireball model “affords a high-fidelity dimensionality reduction and provides key features useful for discriminating between explosives which differ in chemical composition”.

Gross and Perram [30] best summarize the recent advances in understanding the phenomenology of high explosive fireballs by detailing the interrelations between all the techniques and methods developed thus far. A significant outcome of these prior studies

was the development of a low-dimensional physics-based model that is capable of describing with high fidelity the observed spectra in terms of a temperature, size, and handful of by-product concentrations (primarily H₂O, CO₂, and soot) [28, 32]. The model affords significant reduction in the spectral dimensionality with ~500–2000 points being replaced by 5–7 parameters. Using this model against time-resolved spectra (8 Hz at $\Delta\tilde{\nu} = 1.93 \text{ cm}^{-1}$) collected in the BRILLIANT FLASH II field experiment, estimates of the hydrogen-to-carbon ratio $R = \text{H:C}$ were made from the spectra of several high explosives and were in agreement with the stoichiometry of the starting material. Additionally, the fireball cooling rate $\partial T/\partial t$ was highly correlated with the mass of the explosive. By reducing the dimensionality of the spectral datacube to a handful of “orthogonal features” (from an information content perspective), Gross et al. [28-32] demonstrated that high-explosive classification is possible with mid-wave infrared (MWIR) spectral signatures.

2. Phenomenology of an Explosion

To paraphrase from Baum et al. [5, p. 6], an explosion is a process of rapid physical and chemical transformation of a system into mechanical work, accompanied by the change of its potential energy. The work is a result of the rapid expansion of gases already present or produced by the explosion. The ability of chemical systems to rapidly transform into mechanical work in an explosion is determined by three factors: the exothermicity of the process, the high rate of its propagation, and the presence of gaseous reaction products.

An explosion produces energy through a process called oxidation. Fuel burning and an explosive detonating are both examples of oxidation. The heat of reaction results during oxidation because the internal energy of the final product molecules is lower than

the internal energy of the reactant molecules. Accordingly, the exothermicity of the enthalpy of the reaction, ΔH_{rxn} , results because the enthalpy of the product mixture is less than the enthalpy of the reactant mixture. The heat of reaction is a criterion of the efficiency of the explosive and is its most important characteristic [5, p. 6]. The heat of reaction (or detonation or combustion) per unit weight of reactant (fuel plus oxidizer) is greatest when there is just enough oxidizer to burn all the fuel to its most highly oxidized products and the thermal energy of the reaction can result in temperatures of several thousand degrees [14, p. 19]. Using a simplifying assumption that RDX is the only explosive constituent, an estimate from RDX stoichiometry alone gives a heat of reaction on the order of 5.6 MJ/kg with detonation temperatures ranging from 1300–1800K.

The distinguishing characteristic of an explosive over normal chemical reactions of, say, ordinary fuels is its extremely high rate of energy evolution. The linear rate of propagation of the explosion through an explosive charge is typically between 2000-9000 m/sec. In the case of RDX at its theoretical maximum density (TMD) of 1.81 g/cm³, its detonation velocity is 8800 m/sec [14, p. 79]. The transformation from reactants to products can occur within hundred-thousandths or even millionths of a second. Explosions progress to products so rapidly that it can be viewed as an almost instantaneous evolution of energy into the space occupied by the explosive itself. The combustion of ordinary fuels, on the other hand, is slow and energy dissipation can take place through thermal conduction or radiation. [5, p. 7-10]

Upon explosion, highly compressed products are the agents that cause the transformation from chemical potential energy to mechanical work. The maximum pressure during the explosion of condensed explosives attains hundreds of thousands

atmospheres [5, p. 10]. For RDX at TMD with a detonation velocity of 8.8 km/s, its estimated detonation pressure is 35 GPa or about 350,000 atmospheres [14, p.80]. Assuming a typical steel case strength of about 0.34 GPa (~ 50 KSI) [45, p. 70], the detonation pressure for RDX at TMD is two orders of magnitude greater than the case strength. It is this intense pressure that easily overcomes the hoop stress of the steel casing of a conventional munition and subsequently breaks and fragments the bomb during explosions.

An explosion can be divided into three basic processes: combustion, explosion, and detonation. Typically, when a conventional munition is exploded it first undergoes a detonation process, then a general explosion process, and finally a combustion process.

Combustion proceeds comparatively slowly and varies from centimeters per second to several meters per second. Combustion rate varies with external pressure and increases greatly with increased pressure. Thus, a confined combustion will produce a faster burn rate than open air combustion [5, p. 13]. In the present research, combustion analysis is performed on an open air combustion system but the initial detonation is semi-confined inside a mild steel tube 0.41 m in length and open at one end.

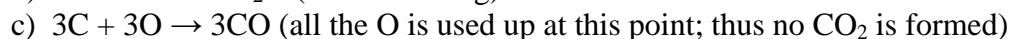
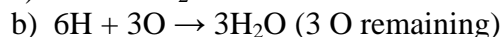
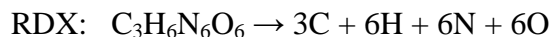
An explosion is defined by a rapid jump in pressure at the explosion site, a changing rate of propagation measuring thousands of meters per second, and a relative independence from external factors such as pressure. Near the vicinity of the explosion, physical damage results from the sudden impact of fast-moving gases on surrounding objects or the propulsion of projectiles by these expanding gases. [5]

Detonation can be looked upon as an explosion moving at a constant rate (in contrast to an explosion which has a changing rate of propagation). In other words,

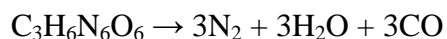
detonation is the stationary form of an explosion. Detonation is the fastest possible rate of explosion for a given explosive at certain given conditions and propagates at faster than the speed of sound in the given material. The maximum destructive effect of an explosion is achieved during detonation. [5]

The propagation of explosion and detonation differ from combustion by the following: combustion propagates through thermal conductivity, diffusion, and radiation, while explosion and detonation propagate by compression of the substance by a shock wave. [5, p. 14]

A fireball is a part of the combustion process. To arrive at this conclusion, let us examine the combustion of a typical explosive. Most explosives are made up of carbon, hydrogen, nitrogen, and oxygen and are called CHNO explosives with their formulas written as $C_wH_xN_yO_z$. During the detonation of an explosive, the breakdown of the reactant molecule can undergo a series of elementary reactions whereby it can dissociate into its separate constituent atoms and even recombine to form intermediate species. These reactions can propagate through the presence of radicals such as H^+ or OH^- in the reaction and release energy in the process. Since myriad elementary reactions can occur in a detonation, it is often convenient to represent the process using an overall stoichiometric relation. In the case of RDX this is written as [14, p. 22]:



Thus the stoichiometry of the overall detonation reaction is,



Any free carbon or CO acts as fuels themselves. In the case of RDX above, there are 3 moles of CO left to act as fuel. After the detonation reaction is complete, the products may be free to expand into air and begin the combustion process. As they do this, they mix with the oxygen in the air, burst into flame, and burn to CO₂ when the proper mixture with the air is reached. This reaction is the fireball that is of interest in the present research and it is this fireball that contains the spectral emissions that are essential for the classification of the explosion event. [14, p. 23]

Although it is a facet of the post-detonation combustion process, this fireball is what is referred to as the detonation fireball. Some general key aspects of the fireball will now be discussed.

Upon detonation of the aluminized explosive in the current research, the fireball rapidly expands to a diameter of about 5 m in roughly 50 ms, increases slightly, and then gradually levels off and remains fairly constant in size. Depending on the aluminum content and explosive and liner weight, initial temperatures range from 1300–1800K within the first 50 ms with some peaking to 2400 K within a few microseconds upon detonation. The combustion lasts for about 2–3 s, of which only the first second remains fully within the FTS field-of-view in this work and is thus of interest from an FTS signature collection perspective. The first 0.02 s of the event is dominated by detonation processes. At this early point in time, the fireball exhibits blackbody behavior and is considered optically thick due to the fact that the Planckian distribution of spectral intensity dominates and masks the spectral features from selective emitters such as CO₂ and H₂O. There is then a short delay during which vortices in the explosion bring in

oxygen from the ambient air to mix with the remaining fuel in the explosion. At this point, combustion processes begin to dominate. Afterburning then ensues which produces additional heat from combustion as well as a subsequent secondary maximum in the temperature profile. This secondary maximum or “hump” indicates the point at which the carbonaceous soot and hydrocarbon fuel are consumed. Eventually, temperature, as well as emissive area begins to decay as energy loss mechanisms, such as radiative cooling, once again dominate and the temperature profile of the fireball begins to exhibit radiative cooling behavior as the combustion concludes. As the particulate detonation by-products are consumed during the afterburn, the fireball becomes less opaque and molecular emission bands become apparent in the infrared spectrum. Thus, feature extraction becomes possible when the blackbody behavior diminishes and selective emissions become detectable. Understanding this phenomenology, we can begin to study field detonations.

III. Temporally-Resolved Infrared Spectra from the Detonation of Advanced Munitions

Overview

A suite of instruments including a 100 kHz four-channel radiometer, a rapid scanning Fourier-transform infrared spectrometer, and two high-speed visible imagers was used to observe the detonation of several novel insensitive munitions being developed by the Air Force Research Laboratory. The spectral signatures exhibited from several different explosive compositions are discernable and may be exploited for event classification. The spectra are initially optically thick, resembling a Planckian distribution. In time, selective emission in the outer edges or wings of atmospheric absorption bands becomes apparent, and the timescale and degree to which this occurs is correlated with aluminum content in the explosive formulation. By analyzing the high-speed imagery in conjunction with the time-resolved spectral measurements, it may be possible to interpret these results in terms of soot production and oxidation rates. These variables allow for an investigation into the chemical kinetics of explosions and perhaps reveal other phenomenology not yet readily apparent. With an increased phenomenological understanding, a model could be created to explain the kinetic behavior of the temperature and by-product concentration profiles and thus improve the ability of military sensing platforms to identify explosive types and sources.

1. Introduction

The ability to quickly identify and classify an explosive type and employ theater assets to further survey or neutralize its source is of great concern for battlefield

commanders. A key to the identification and classification steps is a robust sensing platform able to efficiently characterize detonation signatures. An important prerequisite is understanding of event phenomenology so that an effective, small, low-power sensor can be developed. For this purpose, our research group has fielded rapid-scan Fourier-transform spectrometers, radiometers, and high-speed imagers to various test ranges to remotely collect post-detonation combustion (PDC) signatures from detonations of various $C_vH_wN_xO_yAl_z$ -based high explosives (HEs). To date, the focus has been on interpreting the spectral signatures for the purpose of understanding event phenomenology. A significant outcome was the development of a low-dimensional physics-based model that was capable of describing with high fidelity the observed spectra in terms of a temperature, size, and handful of by-product concentrations (primarily H_2O , CO_2 , and soot). The model affords significant reduction in the spectral dimensionality with ~ 500 – 2000 points being replaced by 5–7 parameters. Using this model against time-resolved spectra (8 Hz at $\Delta\tilde{\nu} = 1.93 \text{ cm}^{-1}$) collected in the BRILLIANT FLASH II field experiment, estimates of the hydrogen-to-carbon ratio $R = H:C$ were made from the spectra of several high-explosives and were in agreement with the stoichiometry of the starting material. Additionally, the fireball cooling rate $\partial T/\partial t$ was highly correlated with the mass of the explosive. By reducing the dimensionality of the spectral data cube to a handful of “orthogonal features” (from an information content perspective), we verified that high-explosive classification is possible with midwave infrared (MWIR) spectral signatures.

The various explosive classes examined during the BRILLIANT FLASH II test exhibited large differences in HE stoichiometry. Distinguishing different explosives with

similar relative amounts of hydrogen and carbon will be more difficult, given that their PDC in the oxygen-rich atmosphere will tend to produce H₂O and CO₂ in similar relative quantities. However, upon detonation, different explosives will proceed to final products through different reaction pathways, and the fireball's temporal signature may be sensitive to these differences, particularly at early times when the combustion processes are more representative of the initial conditions. In Fourier-transform spectroscopy (FTS), temporal and spectral resolutions are approximately inversely related, and our previous PDC measurements have favored spectral resolution so that emitting species could be more easily identified. This has made it difficult to study the global kinetic processes at work in the fireball. By degrading the resolution of previous spectral measurements with post-processing, it was found that a four-times reduction in resolving power ($\Delta\tilde{\nu} = 7.71 \text{ cm}^{-1}$) had a minimal impact in the precision of temperature, size, and by-product concentrations derived from the model. Thus, improving temporal resolution by degrading resolving power could lead to improved understanding of the kinetic aspect of fireball phenomenology.

Table 2. Listing of some constituent materials and nominal quantities for 22 test items.

EXPLOSIVE			LINER		TEST ITEM	INSTRUMENTATION	
HE Type	HE RDX Content	HE Al Content	Liner Al Content	Liner Volume %	Final Test Item Al Content	FTS Resolution (Temporal / Spectral)	Phantom Camera Frame Rate (frames/s)
A	Low	High	Low	w	None	82 Hz at 16 cm ⁻¹	10,000
B	Medium	Low	Medium	x	Low	54 Hz at 8 cm ⁻¹	
C	High	None	High	y	Medium		
				z	High		

To begin studying the kinetic piece of the fireball problem in greater detail, measurements of fireballs arising from various HEs fashioned from aluminized RDX

were recently made at a test range at Eglin Air Force Base. By using a faster interferometer operating at $\Delta\tilde{\nu} = 3.86$ or 7.71 cm^{-1} , spectra were acquired at rates of 55 or 82 Hz. A four-channel 100 kHz radiometer and two high-speed visible cameras provide band-integrated intensities and imagery to augment the FTS measurements. This chapter presents an overview of the test and a summary of initial findings discovered in the early stages of this ongoing research effort.

2. Experimental

The Reactive Liner Naturally Fragmenting Test Unit (NFTU) field tests were developed to meet Department of Defense (DOD) Insensitive Munition (IM) requirements of General Purpose (GP) warheads. The IM requirement is part of an effort to improve fielding, storage, and safety of current inventory GP bombs by reducing their sensitivity to ship-board and munitions storage fires as well as sympathetic detonations. The tests were conducted over 15 April – 1 May 2008 at the Advanced Warhead Experimentation Facility (AWEF) of the Air Force Research Laboratory (AFRL) at Eglin Air Force Base, Florida. A factorial Design-of-Experiments was conducted by AFRL engineers to examine the main effects and interactions of the various liner and explosive types. Thirteen optical signatures were successfully collected out of 22 scheduled detonations. These detonations were comprised of three distinct types of liners and three distinct types of explosives and their various combinations. Table 2 summarizes some important test parameters. The liners were melt-cast thermoplastic materials with aluminum content varying from low to high and arranged along the inside walls of a

warhead. The explosives were RDX-based (cyclotrimethylene-trinitramine, $C_3H_6N_6O_6$) melt-cast formulations also with varying aluminum content from none to high.

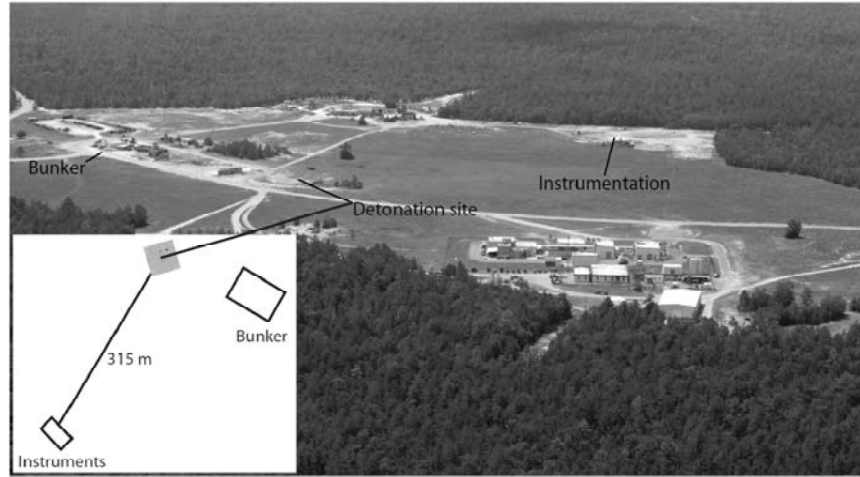


Figure 1. Aerial view of the AWEF test range. The blast arena where the test items were detonated is highlighted by the concentric rings at the top of the inset schematic.



Figure 2: Left to right, the ABB-Bomem MR-254 FTS, CI Systems ColoRad radiometer, and pair of Phantom 5.1 and 7.1 cameras. Each is peering through a hole from behind thick iron armor shielding. A plywood roof was subsequently installed to shield the instruments from heating via direct sunlight, thereby minimizing the effects of self-emission in the InSb channel of the FTS and the InSb and HgCdTe channels of the radiometer.

The following is a brief overview of the reactive liner NFTU tests. Figure 1 provides a birds-eye view of the test range. The instrument suite was placed on a stable concrete pad approximately 335 m from the center of the blast arena and was the only location at the AWEF that had a direct, unobstructed line-of-sight to the target at a safe standoff distance. All equipment was remotely triggered from within the hardened command and control center. Time-resolved infrared spectra were collected using an ABB-Bomem MR-254 FTS operated at 82 Hz with a nominal spectral resolution of 16 cm^{-1} ($\Delta\tilde{\nu} = 7.71\text{ cm}^{-1}$) using InSb ($1800\text{--}10,000\text{ cm}^{-1}$) and InGaAs ($5600\text{--}10,000\text{ cm}^{-1}$) detectors. A few events were collected at 8 cm^{-1} (3.86 cm^{-1}) resolution at a rate of 55 Hz. The interferograms were over-sampled at half-HeNe wavelengths putting the Nyquist frequency at $15,802\text{ cm}^{-1}$ which is well beyond the response of the InSb and InGaAs detectors. The interferometer was fitted with 76 mrad optics providing a 24 m diameter field-of-view (FOV) at the target. Bore-sighted video indicated that the fireballs consistently under-filled the FOV. Figure 2 shows additional instruments that were deployed to record other aspects of the incoming optical signatures. A CI Systems ColoRad four-channel radiometer using InSb, InGaAs, HgCdTe, and Si detectors, each with a distinct narrow optical density filter, collected broadband intensity spectra at 100 kHz. Phantom 5.1 and Phantom 7.1 high-speed digital video cameras operating between 2000–8000 fps were used to study fireball growth and characterize shockwave dynamics. A Canon XL-1 digital video camera served as a witness camera and the audio channel was used to measure the time for the pressure wave to reach the location of the equipment.

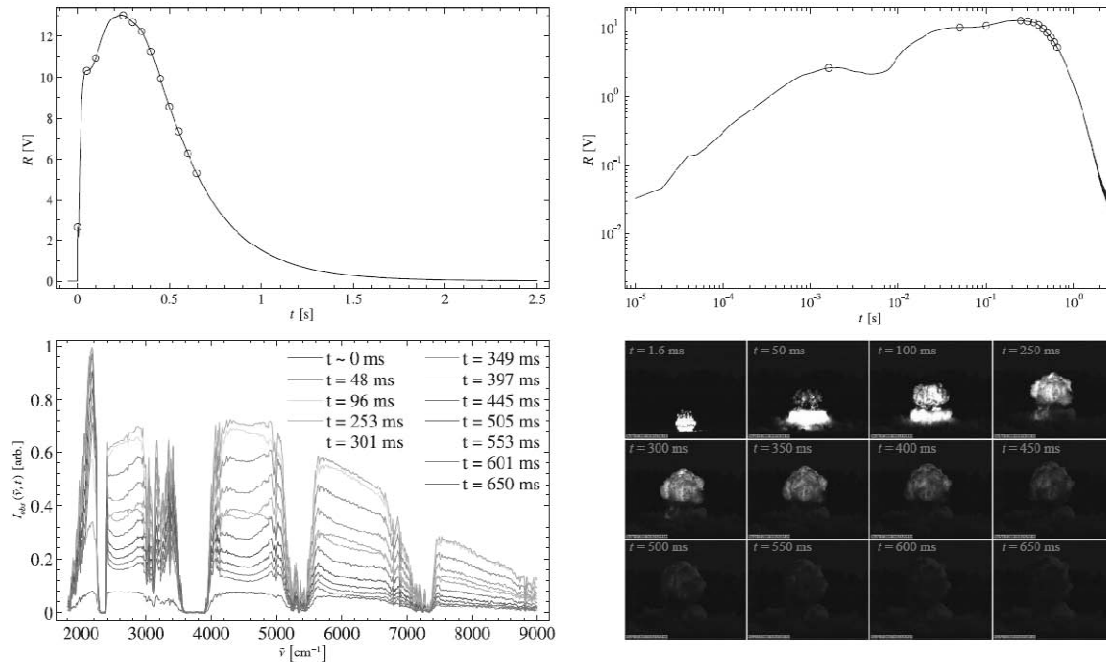


Figure 3. Overview of the radiometric, spectro-radiometric, and high-speed imagery collected from an aluminized RDX fireball. *Top-left panel:* Band-integrated radiometric response of the InSb channel of the CI Systems ColoRad radiometer. *Top-right panel:* Same band-integrated radiometric profile shown on a log-log scale. Open circles indicated the times corresponding to the spectra and imagery shown in the bottom panels. *Bottom-left panel:* Time-evolution of the MWIR spectra captured by the ABB-Bomem MR-254 FTS. *Bottom-right panel:* Color imagery captured by the Phantom v7.1 camera. A majority of the pixels illuminated in the first frame were saturated.

A low-temperature (10°C below ambient to 80°C) wide-area blackbody (BB) source and a high-temperature (1250°C) cavity blackbody source were used to calibrate the FTS detector several times each day. The calibration measurements were performed before and after each detonation optical signature was collected. The wide-area BB was placed within a few centimeters of the FTS entrance aperture and thus over-filled the FOV. Several low-temperature blackbody measurements were made, enabling an accurate determination of both detector response (gain) and instrument self-emission (offset) between $1750\text{--}3000\text{ cm}^{-1}$. Instrument self emission was important between 1750--

2500 cm^{-1} . The high-temperature cavity BB source was used to extend the detector response to 10,000 cm^{-1} . The path between the FTS and the cavity BB source was approximately 6 m. When calibrating against the cavity BB, the field stop of the FTS was minimized to cover an area only slightly larger than the BB source aperture in order to minimize the contribution of background radiation. The cavity BB was shielded from direct sunlight to minimize reflection of solar radiation off of the faceplate and promote a stable temperature. Given the precautions taken in the cavity BB measurements, it was reasonable to assume that the only source of photons beyond 3000 cm^{-1} was from the cavity, enabling a relative measure of the detector response (gain) via division by the appropriate Planckian distribution. In other words, both instrument self emission and background radiation (i.e., radiation generated by or reflected from the warm faceplate of the BB) could be ignored above 3000 cm^{-1} . An absolute scale for the relative gain curve between 3000–10,000 cm^{-1} was established by comparison with the gain curve already determined via the wide-area source where they overlap near 3000 cm^{-1} .

3. Analysis

Figure 3 presents an overview of the data collected by our primary suite of instruments for the detonation of an aluminized RDX explosive. The un-calibrated band-integrated response of the InSb channel on the CI-Systems radiometer are shown in the top two panels, and spectra and visible imagery at select times are provided in the bottom panel. In the MWIR, the duration of the event is approximately 2 s, and decays to e^{-3} of the peak response in ~ 1.25 s. The top-right panel provides the same information on a log-log plot so that the full dynamic range of both the temporal and intensity axes can be

visualized. There are two distinct time scales, the first associated with the initial and rapid detonation (0–5 ms), and the second associated with the post-detonation combustion (5–1500 ms). The initial detonation is a combustion reaction occurring under extreme conditions, with stored oxygen serving as the oxidizing materials. The fireball rapidly expands, and near the end of the initial detonation, the radiant emissions in the MWIR begin to decrease (cooling by expansion). Visible imagery indicates that luminous emissions near the top of the fireball have substantially decreased, appearing dark and sooty. At the same time turbulent eddies can be seen forming. The primary shock wave then reflects off the ground and proceeds back through the fireball causing shock heating and with it re-ignition of the non-luminous sooty regions and enhanced (brighter) combustion throughout.

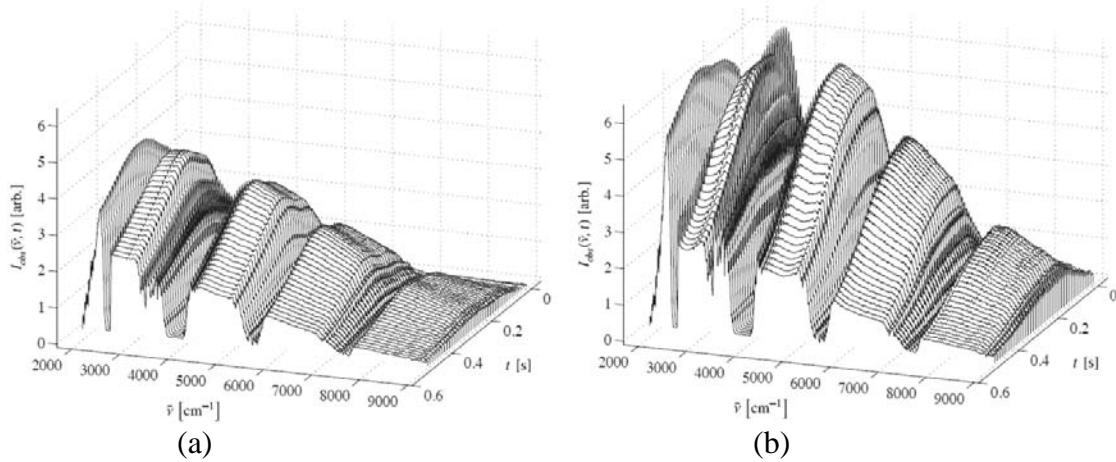


Figure 4. Time-resolved spectral data cubes for the first 0.5 s of a low-Al (a) and high-Al (b) RDX detonation fireball. Effects of detector response (gain) have been accounted for and the scale for the ordinate axis is the same in both plots.

This post-detonation combustion process continues as atmospheric oxygen is brought into the fireball through turbulent mixing. Visible imagery indicates that the fireball reaches a peak area after about 200–300 ms and remains at about the same size, although the morphology changes and its center-of-mass increases in height with time. The complex interplay of fluid dynamics and combustion chemistry produce a fireball that is both highly luminous in some regions and a sooty black in others, resulting in an interesting temporal variation of the total, band-integrated intensity, particularly at early times. The band-integrated intensity reaches a maximum at approximately 250 ms, after which cooling by radiative emission and turbulent mixing with air cause the signal to decay back to ambient conditions within a few seconds.

At early times ($0 \leq t \leq 150$ ms), the spectra indicate an optically-thick fireball with continuum emission from soot masking out selective emission from gaseous by-products. At these times, the only strong spectral features are due to absorption by atmospheric water and carbon dioxide. Shortly after the peak total emission occurs ($t \sim 250$ ms), moderate amounts of selective emission are observed in the wings of strong atmospheric absorption bands, likely due to radiant emission from hot H_2O (3200–4200, 5600–6000 cm^{-1}) and CO_2 (2200–2450, 4800–5200 cm^{-1}) within the fireball. As atmospheric oxygen is made available through turbulent mixing, the carbonaceous soot can be oxidized to CO and then to CO_2 , leading to a less thick (i.e., slightly more transparent) fireball. Similar spectral features have been observed in TNT detonation fireballs and understood in terms of the simple phenomenological model briefly described in the introduction and discussed more thoroughly in the references [28–32, 47]. Preliminary results of fitting this spectral model to the data (not shown) have been

fair, capturing the gross features of the spectral variation in the data. However, the fit residuals exhibit small, but non-negligible systematic errors and improvements to the model will be investigated in future work.

Two events, a low-Al and a high-Al RDX formulation, are now analyzed in greater detail. Figure 4 presents time-resolved spectral data cubes for the first 500 ms for each type. The radiant emissions from the high-Al formulation are brighter in the MWIR. Continuum radiation from soot dominates the spectral emissions from both fireballs. At later times, the high-Al RDX fireball begins to exhibit selective emission in the wings of the atmospheric absorption bands. To facilitate a comparison of the relative spectral features, normalized fireball spectra corresponding to both formulations are displayed in Figure 5 at an early ($t \sim 200$ ms) and later ($t \sim 600$ ms) time. At 200 ms, both spectra appear Planckian in nature. By 600 ms, the differences in the spectral features are pronounced. The low-Al formulation is still strongly dominated by continuum emission, whereas the high-Al fireball exhibits much stronger selective radiation. This may indicate a relationship between the aluminum content in the explosive mixture and soot production and oxidation processes in the fireball, since oxidation of soot is necessary to make the fireball optically thin enough to observe emissions from gaseous combustion by-products such as H_2O and CO_2 .

Soot chemistry can be indirectly studied—in an approximate way—by examination of the continuum emission. This can be achieved by fitting a single-temperature Planckian intensity distribution to the regions of spectra in which molecular line emission is unimportant and continuum radiation from hot particulate matter

dominates. To this end, the following model was used to make estimates of the temperature T and emissivity-area product $\varepsilon_s A$:

$$I_{obs}(\tilde{\nu}, t) = \tau(\tilde{\nu}) \varepsilon_s A(t) B(\tilde{\nu}, T(t))$$

where τ accounts for atmospheric absorption and B is the Planckian distribution for radiance. The model was fit to the spectral regions $4400\text{--}4700\text{ cm}^{-1}$ and $5800\text{--}6500\text{ cm}^{-1}$ for times up to approximately 1 s. At longer times, the spectrum was too noisy to extract

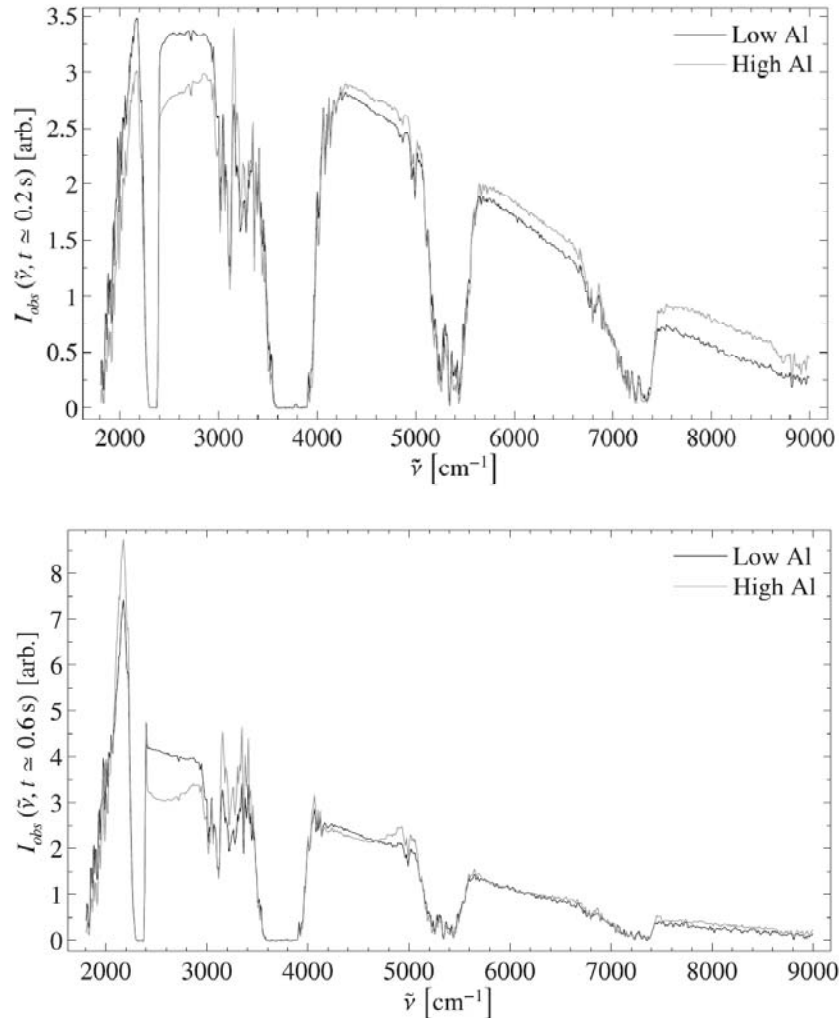


Figure 5. Normalized spectra corresponding to RDX containing low (—) and high (—) aluminum content at (top) 0.2 s and at (bottom) 0.6 s. At early times, both spectra are dominated by continuum radiation from the soot. As time progresses, the high-Al RDX exhibits more selective emission near 2100, 3200, and 4950 cm^{-1} .

reliable fit parameters. Figure 6 presents the results of estimating T and $\varepsilon_s A$ from the time-resolved spectra corresponding to both the low-Al and high-Al RDX formulations. Error bars are occasionally displayed so that the trending of fit uncertainty can be assessed. The $\varepsilon_s A$ curves are normalized by the peak area.

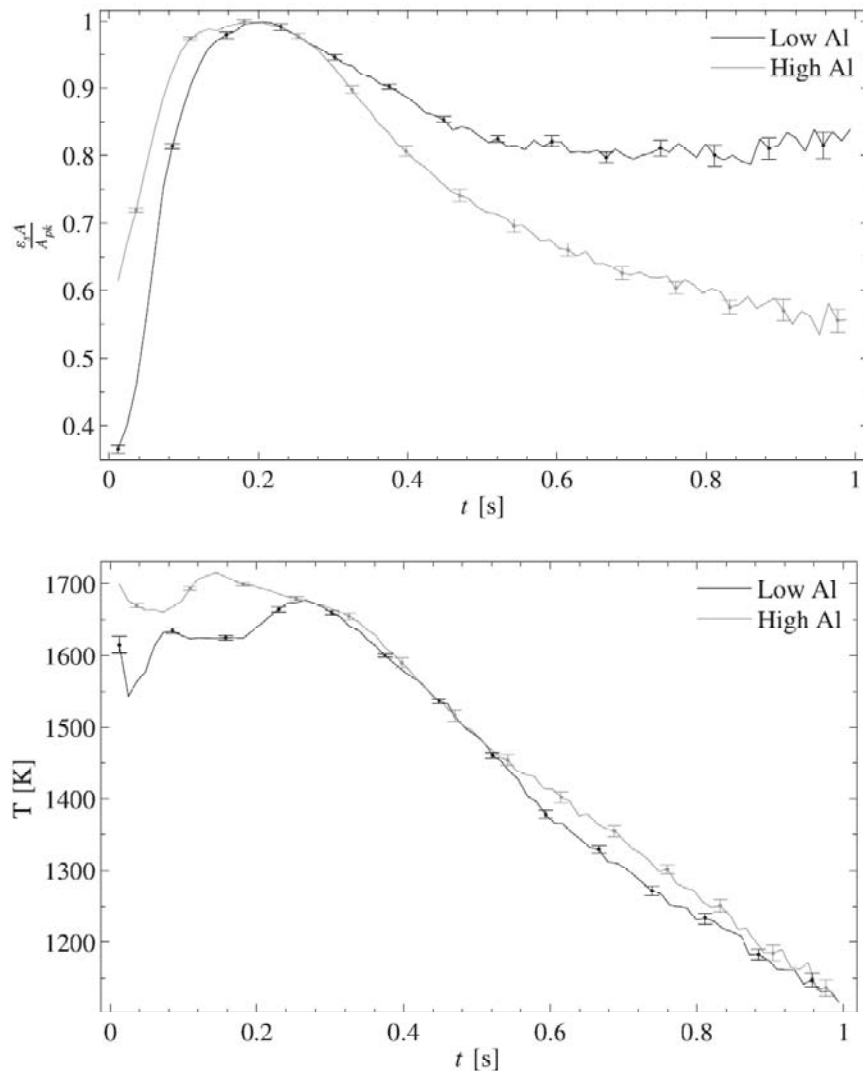


Figure 6. (top) Peak-normalized emissivity-area and (bottom) temperature curves for the low-Al and high-Al RDX fireballs obtained by fitting a Planckian distribution to spectral regions free from selective emission (4400–4700 and 5800–6500 cm^{-1}).

We noted previously that the fireball reaches its maximum size around 200–300 ms, and this is approximately the same time at which MWIR emissions reach their peak total intensity (*cf.* Figure 3). Additionally, imagery also suggests sooty fireballs and the spectral emissions dominated by continuum radiation and absent of line emission corroborate this observation. Given this, an initial emissivity of one is assumed, and the initial rise in the normalized $\epsilon_s A$ curve is due to the fireball's expansion. Imagery also suggests that the fireball area remains approximately constant (or continues to grow slightly), so that the subsequent decay in $\epsilon_s A$ is likely due to a decrease in ϵ_s . At times after the peak, the normalized $\epsilon_s A$ curves may reveal differences in the kinetics of soot production and oxidation in the low-Al and high-Al formulations. Two possible explanations for the larger decrease in $\epsilon_s A$ for the high-Al formulation may be (1) that its soot oxidation rates are higher at later times or (2) that its soot production rates are lower at earlier times. Both possibilities (or a combination thereof) could lead to the high-Al formulation having a more optically thin fireball at later times. Note that the two explosive charges feature different aluminum content in both the explosive mixture and the reactive liner. To assess which (if any) variable is more influential in the observed results, it will be necessary to examine spectral data from formulations in which the aluminum content of the reactive liner and/or HE material is fixed. There are likely other possible explanations for the observed behavior (e.g., the differences observed are to within the natural variance of a large number of measurements), and at this point, nothing definitive can be stated regarding soot production and consumption mechanisms and rates. This is a challenging topic posing both theoretical difficulties and experimental challenges under ideal laboratory conditions [44]. Moving to the harsh and highly non-

ideal environment of a detonation fireball exploded in an uncontrolled environment only exacerbates the problem. What is significant here is that proper interpretation of the time-resolved spectra will be highly valuable in the development of a simplified “zeroth-order” kinetic fireball model.

The temperature profiles for the low-Al and high-Al formulations are similar. Differences are more profound at earlier times, but are also significant between 600–900 ms. The high-Al formulation exhibits a higher temperature both early on and at later times, and this is not inconsistent with the additional heat release that would presumably accompany the enhanced soot oxidation possibly occurring at later times in this fireball.

4. Conclusions

A recent field experiment has resulted in the collection of a rich set of radiometric, spectro-radiometric, and high-speed imagery measurements of various aluminized RDX high explosive detonation fireballs. The improved temporal resolution of the spectral measurements will benefit the development of a highly-simplified global kinetic model for detonation fireballs. Variations in aluminum content substantially alter the fireball chemistry, and a proper interpretation of the time-resolved spectral emissions is key to understanding the kinetic behavior of the by-products. Combining imagery analysis with simple Planckian fits to the spectral data indicate a possible correlation between the aluminum content in the high explosive with soot production and oxidation rates.

IV. Fireball and Shock Wave Dynamics in the Detonation of Aluminized Novel Munitions

Overview

High speed 4 kHz visible imagery from 13 field detonations of aluminized RDX munitions with varying liner compositions are collected to study shock wave and fireball dynamics. The Sedov-Taylor point blast model is fitted to shock front temporal history data and blast wave characteristics are interpreted by varying the energy release factor, s , and blast dimensionality, n . Assuming a constant release of energy, $s = 1$, the Sedov-Taylor model establishes a near spherical expansion with dimensionality of $n = 2.2\text{--}3.1$ and shock energies of 0.5–8.9 MJ. These shock energies correspond to efficiencies of 2–15 percent of the RDX heats of detonation. A drag model for the size of the fireball yields an average radius of 5.1 m that is consistent with the luminous fireball size in visible imagery, and initial shock speeds of Mach 4.7–8.2. Initial shock speeds are a factor of 3–4 times smaller than RDX theoretical maximum speed and may help explain the low efficiencies observed. Shock energy decreases as high explosive is traded for liner or aluminum content. The post-detonation combustion plume after 0.25 s reveals a fairly constant rate of ascent and may be tied to buoyancy phenomenon. Test article confinement, cylindrical geometry, and non-homogeneity between the liner and explosive fill and atmospheric conditions are likely contributors to non-ideal behavior.

1. Introduction

The classification of battlespace combustion events from visible and infrared signatures requires new field data, simplified phenomenological models, and the correlation of key features with event characteristics. Despite the inherent variability in

radiant intensity of post-detonation fireballs, we have demonstrated a connection between mid infrared spectral signatures associated with H_2O and CO_2 combustion products and the stoichiometry of significantly different high explosive (HE) materials [30]. More recently, a suite of radiometers, imagers, and spectrometers was deployed to collect signatures from RDX-based explosives with variations only in aluminum content and liner composition [26]. We hope to extend classification to these additional events by developing correlations between spectral features and imagery signatures. In particular, the evolving temperature of the post-detonation combustion fireball might be related to detonation shock wave dynamics since higher detonation efficiency may suggest less material available in the afterburn phase of the explosion event. In this chapter we characterize the shock wave dynamics, size of the soot, combustion and detonation product volume, and rate for fireball lofting.

Shock wave analysis is found in a multitude of applications ranging from pulsed laser deposition to bomb detonations to astrophysical events. Cox [15] and Raymond [50] apply shock analysis to interstellar phenomena by modeling a gas as it interacts with a shock front from a supernova remnant. Atomic spectral emissions are studied assuming the gas undergoes thermal and density fluctuations followed by ionization and subsequent recombination of hydrogen ions and electrons [15]. Astrophysical time scales enable the presumption of a steady state flow of similarly affected gases thus allowing a temporal integration of the spectrum vice a spatially integrated one. Characteristics of the shock wave and the propagation medium can then be reckoned from analysis of the spectral lines. Dokuchaev [21] analytically derives the behavior of a time-dependent spherical shock wave in astrophysical scales by assuming the shock wave to be continuously

pumped or injected by a constant-luminosity central source through some radiative mechanism like those found in stellar phenomena such as the early phase of a supernova explosion. For the present work, however, methodologies and techniques from pulsed laser ablation and bomb explosion analyses in literature are used.

By monitoring the strength and propagation speed of detonation shock waves, the energy released in the explosive event can be inferred using blast wave models from Sedov [54], Taylor [60], and Zel'dovich [66] similar to work done in [22, 36, and 43]. The remaining energy from the heat of detonation may be available for secondary combustion driving the fireball temperature dynamics.

Shock wave propagation, size of the emissive fireball, and maximum extent of detonation products evolve differently and a characterization of the detachment of the shock front from the fireball is not well modeled in simplified empirical models [2, 38, 64-65]. Dispersal of particulate materials is likely controlled by the initial velocity and subsequent drag [22]. One might anticipate that the initial velocity matches the shock propagation, but the effective drag coefficient and maximum extent of the fireball is harder to predict. Correlation of fireball size as determined from imagery and spectra may depend on spectral band and are poorly understood [19, 30]. The present work characterizes visible fireball size and shock propagation.

The effect of aluminum content in condensed high explosives has been studied in some detail [7, 10, 13, 23- 24, 41, 64]. However, the precise influence of aluminum on shock dynamics is not completely understood. Studies show its influence is limited to short time scales, preferably in the presence of oxygen, if it is

to support propagation of the shock front due to the liberation of chemical energy during the reaction [7]. Gilev and Anisichkin [23] use electrical conductivity measurements during an explosion to suggest that the reaction of aluminum with the detonation products occur within a microsecond time span immediately upon detonation. Analyzing the solid residue after a detonation in an explosion chamber, they conclude that since a thin oxide layer quickly forms around the aluminum particles, this effectively inhibits further reaction of the bulk aluminum with other species resulting in the majority of the aluminum additive acting as inert non-participants in the detonation. They further conclude that the thermal effect from the aluminum additives in their tests is 5–14% of the HE energy. Their tests also show that smaller aluminum particle size resulted in more fraction of reacted aluminum. Work by Lefrancois et al. [41] on the effect of nanometric aluminum additives to HEs suggests that particles on the order of 100 nm in size do not add to the ballistics performance of RDX-AP HEs. They also attribute this to the presence of a thin 3 nm layer of Al_2O_3 on the surface of the aluminum particles. However, they found that reflected blast waves and reflected impulse are strengthened by these metallic nanoscale additives. They attribute these results to the long time thermal transfer from the hot aluminum particles to the gaseous detonation products occurring during hundreds of microseconds to a few milliseconds. Other studies [9-10] suggest the performance benefits of aluminum may lie in timescales well beyond the detonation. The impact of aluminum on the size of the emissive fireball is largely unexplored [11, 48]. A factorial design of experiments was conducted in

the present work to study the effect of aluminum content in the high explosive and liner.

2. *Experimental*

Thirteen aluminized novel munitions varying in high explosive content from 6.3 to 16.9 kg and liners of 2.8–10.7 kg were detonated at the Air Force Research Laboratory's Advanced Warhead Experimentation Facility (AWEF) in Florida, U.S.A. Figure 7 depicts the observation geometry at the test site. The test article is centered within concentric rings of instrumented pressure probes and Celotex bundles arranged at 3.05 m increments from the center. A corner of a concrete blast test pad proved to be the longest-standoff, unobstructed, zero-elevation observation site at the AWEF. The presence of the tree line behind the test arena was fortuitous for shock front tracking because it provided good contrast during digital image processing.

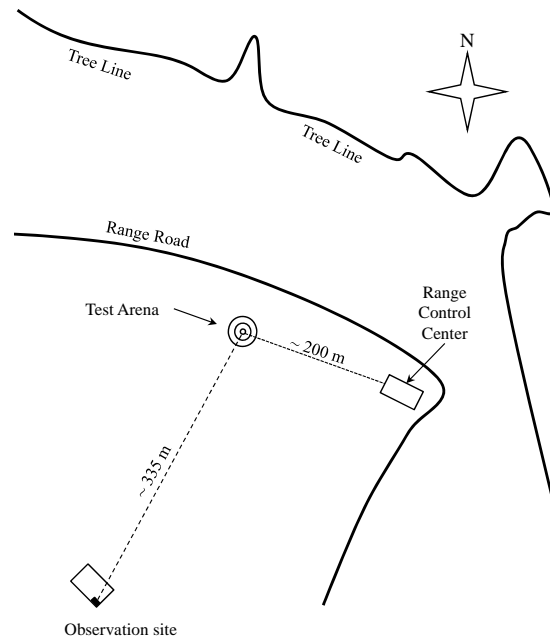


Figure 7. Schematic of the Advanced Warhead Experimentation Facility (AWEF).

The test article consists of a 0.4064 m cylindrical tube of mild steel with an inner and outer diameter of 17.8 and 20.3 cm, respectively. For this length-to-diameter value of $L/D > 2$, the “work done by the pressure at the end of the charge” can be represented by some work function that approaches a constant value. [14, p. 297] The test article is filled with cyclotrimethylene-trinitramine ($C_3H_6N_6O_6$, RDX)-based aluminized HE or a combination of explosive and reactive liner in varying amounts according to Table 3. The events in Table 3 and subsequent tables in this chapter are listed from most to least amount of HE weight in the test articles. The event nomenclature, E#, denotes chronological order in the test sequence.

Table 3. Composition of test articles

Event	High Explosive (HE)			Liner			Total Munition		Weight Fractions				
	Weight (kg)	RDX (kg)	Al (kg)	Weight (kg)	Volume (%)	Al (kg)	Weight (kg)	Total Al (kg)	Liner	RDX	HE	Binder	Al
E13	16.92	10.83	3.38	0.00	0	0.00	16.92	3.38	0.00	0.64	1.00	0.16	0.20
E5	16.74	10.88	3.01	0.00	0	0.00	16.74	3.01	0.00	0.65	1.00	0.17	0.18
E10	15.84	13.14	0.00	0.00	0	0.00	15.84	0.00	0.00	0.83	1.00	0.17	0.00
E8	15.83	13.14	0.00	0.00	0	0.00	15.83	0.00	0.00	0.83	1.00	0.17	0.00
E4	13.42	8.72	2.42	2.78	20	1.53	16.20	3.95	0.17	0.54	0.83	0.14	0.24
E17	13.37	8.69	2.41	2.78	20	1.53	16.15	3.94	0.17	0.54	0.83	0.14	0.24
E12	12.69	10.53	0.00	3.56	20	2.67	16.25	2.67	0.22	0.65	0.78	0.13	0.16
E16	12.67	10.52	0.00	3.56	20	2.67	16.24	2.67	0.22	0.65	0.78	0.13	0.16
E7	12.65	10.50	0.00	2.78	20	1.53	15.43	1.53	0.18	0.68	0.82	0.14	0.10
E11	9.75	7.21	0.88	6.23	40	4.05	15.98	4.93	0.39	0.45	0.61	0.10	0.31
E6	6.75	4.39	1.22	10.65	60	7.99	17.40	9.20	0.61	0.25	0.39	0.07	0.53
E15	6.69	4.35	1.20	8.33	60	4.58	15.02	5.78	0.55	0.29	0.45	0.08	0.39
E3	6.31	5.24	0.00	8.33	60	4.58	14.64	4.58	0.57	0.36	0.43	0.07	0.31

The total device weight is nearly constant so that the fraction of the weight allocated to liner and aluminum decreases as the high explosive weight increases, as illustrated in Figure 8. The average aluminum particle size is 23 μm . Test articles without liners were lined with a very thin layer (0.1 mm) of an asphaltic hot-melt to prevent contact between

the metal casing and the high explosive. The test article is capped at the bottom with a 1.27 cm steel plate bolted to the cylinder and capped at the top with a detonation train consisting of RP-80 Exploding Bridge Wire, A-5 booster (2.54 cm diameter by 2.54 cm thick, ~ 110 g), Comp-B booster (5 cm diameter by 5 cm thick, ~ 120 g), and Comp-B booster (20 cm diameter by 2.52 cm thick, ~1.5 kg).

A suite of instruments consisting of a four-band radiometer, an FTIR spectrometer, an audio-visual witness camera, and Phantom v5.1 and v7.1 high-speed digital cameras collected signatures from an unobstructed standoff distance of 335 m. For the present research, 8-bit grayscale, 768 x 384 pixel visible signatures from the Phantom v5.1 are used as the primary data set. The images are collected at 3000 and 4200 frames per second (fps) with an effective horizontal field-of-view (FOV) of about 70 m, or 91 cm/pixel. Exposure times range from 50–240 μ s to prevent saturation and produce well-contrasted gray-scale images.

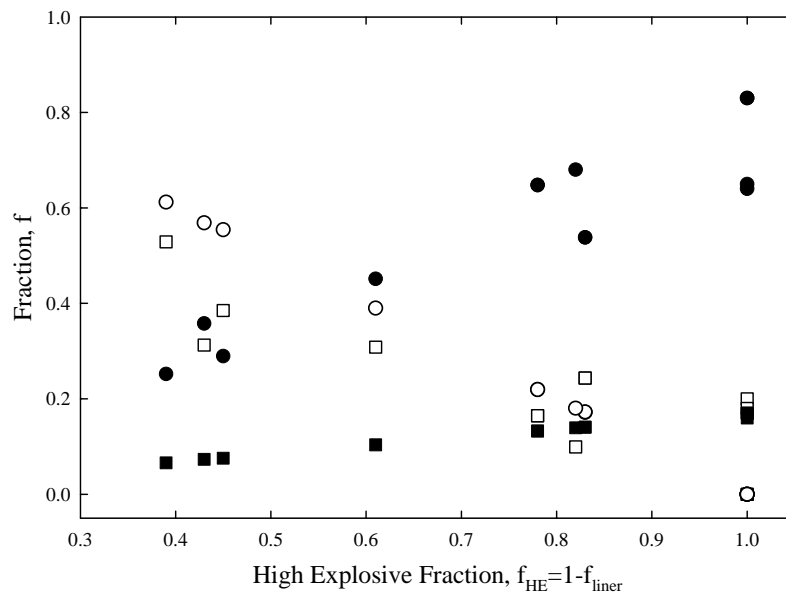


Figure 8. Weight fractions for: (○) liner, (□) aluminum in both liner and HE, (●) RDX, and (■) binder.

The field tests were conducted during a two-week period in April 2008. Table 4 highlights meteorological conditions for each test. Relative humidity of 26–57% and wind speeds of 0–16.3 mph were recorded. Relative humidity for events E3 and E4 were not recorded so the value for event E5 (taken the same day) was used in order to estimate the atmospheric density. Large variations in wind speed or wind direction for a given event are attributed to wind gusts recorded at the range control center weather station. A characteristic length scale (l_o) and time scale (τ_o) are defined by Eq. (5) and Eq. (6), respectively.

Table 4. Meteorological conditions

Event	Julian Date	Atmospheric Conditions				Wind		Scales	
		Temperature (K)	Pressure (psi)	R Humidity (%)	Density (kg/m ³)	Speed (mph)	Direction	Midfield, l_o (m)	τ_o (ms)
E13	2008121	292	14.83	26.00	1.22	3.3	N	1.25	0.14
E5	2008107	288	14.90	26.00	1.24	0	-----	1.24	0.14
E10	2008120	284	14.84	34.00	1.25	1.1-8.2	NE/N/NW	1.32	0.15
E8	2008108	286	14.89	32.00	1.25	6.7	SE	1.32	0.15
E4	2008107	274	14.94	NR	1.31	0-9.8	S/SE	1.13	0.13
E17	2008122	295	14.82	50.00	1.20	7.8-8.5	S	1.16	0.13
E12	2008121	276	14.85	26.00	1.29	6.7	S/SW	1.21	0.14
E16	2008122	280	14.83	52.00	1.27	12.7-14.3	S/SE	1.22	0.14
E7	2008108	277	14.91	33.00	1.29	7.1	SE	1.21	0.14
E11	2008120	291	14.83	31.00	1.22	4.9-16.3	NW/W	1.09	0.12
E6	1008108	276	14.91	43.00	1.30	4.6	E/SE	0.90	0.10
E15	2008122	280	14.83	57.00	1.27	10.2-10.5	SW/S/SE	0.91	0.10
E3	2008107	275	14.94	NR	1.30	4.0-9.0	NE/E/SE	0.96	0.11

3. Image Processing

A single image from event E8 at 13 ms after detonation is illustrated in Figure 9. The fireball and particulate cloud have expanded to a radius of about 5.6 m. In this frame, the image is dominated by dark soot with a small bright region representing post-detonation combustion. High speed fragments can also be seen intercepting the dirt just outside the fireball volume. Tracking of the shock wave front is made possible by frame-

differencing images that are three to five frames apart. [25] Figure 9b illustrates this difference on a logarithmic scale. The shock wave front and secondary reflected shock is readily observed. The displacement of the shock front from the detonation origin, R_s , is determined to within about 1 pixel at a temporal resolution of 0.24–0.33 ms. The shock front is nearly hemispherical, with an ellipticity of $\varepsilon = 0.95$. The location of the shock wave front, R_s , is tracked along an angle of about 15 degrees relative to the ground. This line of observation was chosen as it provided the best contrasted images for the greatest number of image frames. As will be discussed in § 4.1, ground effects do not influence the behavior of the shock front dimensionality along this line of observation. The detonation point of origin is defined as the center of the steel test article.

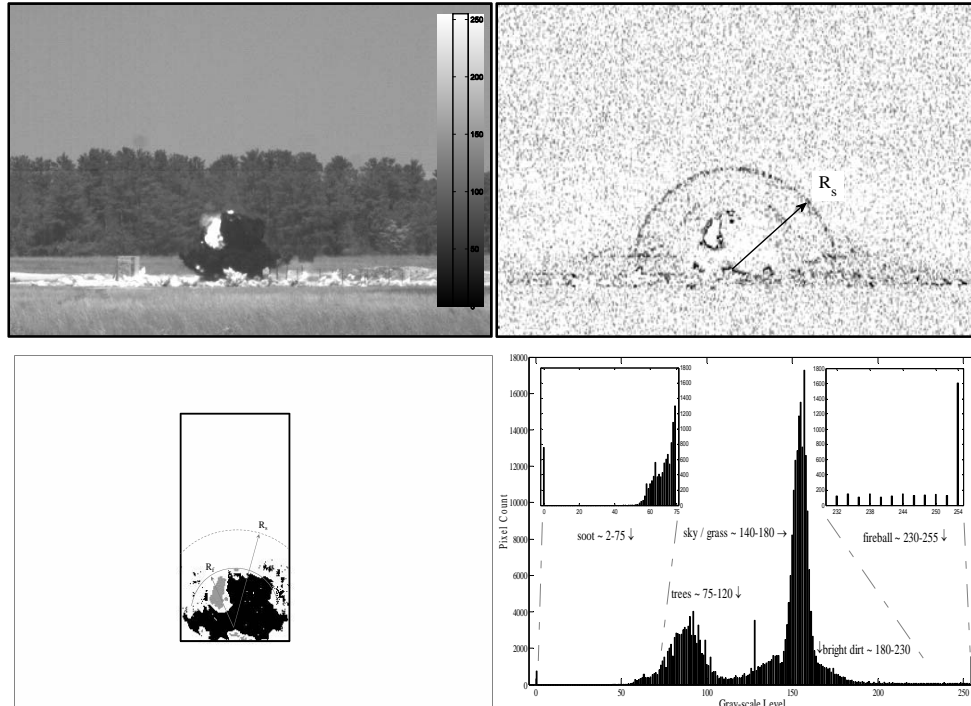


Figure 9. (a) Visible image for event E8 13 ms after detonation with 8 bit gray scale for intensity. (b) Image processed by taking the \log_{10} of the frame-differenced image. (c) Intense pixels of the fireball (gray) and dark pixels of the soot (black) within the rectangular windowed selection. (d) Histogram of the image showing 8-bit digital number range ($1-2^8$) of gray-scale pixel intensity levels of various features.

Figure 9c highlights the emissive pixels of the fireball (gray) and pixels with soot (black), illustrating the maximum extent of the fireball, R_f . The shock front is well detached from the emissive fireball and soot cloud at 13 ms after detonation. The shock has propagated to $R_s = 10.1$ m, well beyond the maximum extent of the fireball, $R_f = 5.6$ m. Figure 9d depicts a histogram of the 8-bit digital number gray-scale of the original image. Note that the pixels of interest (fireball and soot) are located in the wings of the histogram and easily separable from the majority of the pixels in the image constituting grass, trees, and sky. The radius of the fireball front, R_f , is defined from the detonation point of origin to the maximum extent of the fireball edge along an angle similar to that used to track the shock front, R_s .

For each detonation event, the first 20–30 frames are individually analyzed to obtain the most accurate tracking of the luminous fireball growth. Elapsed time is recorded by taking the difference of the embedded time stamps between successive frames. After the shock wave detaches from the fireball, only every fifth or tenth succeeding frame is analyzed for fireball and shock wave radii.



Figure 10. Fireball from event E7 at: (a) $t = 0.30$ s with a fireball radius of 6.13 meters and (b) at $t = 0.35$ s, with a rise relative to the blast origin of 13.5 m.

Much later in the development of the fireball, the emissive area rises and flattens, as shown for event E7 in Figure 10. At $t = 0.35$ s, the fireball size has grown to a radius of more than 6.1 m and risen to a maximum height of greater than 13 m. Ellipticity for event E7's post-detonation particulate cloud (PDPC) or plume cloud at $t = 0.35$ s is $\varepsilon = 0.72$ compared to its shock wave ellipticity of $\varepsilon = 0.95$ at $t = 0.01$ s.

4. Results and discussion

Shock wave analysis is accomplished using the Sedov-Taylor model where blast dimensionality, rate of energy release, and blast energy can be examined. The post-detonation combustion fireball is analyzed using a drag model.

4.1 Shock wave analysis

The radius of the shock front, R_s , and fireball, R_f , for event E7 are illustrated as functions of time in Figure 11. The shock front detaches from the fireball at about 4 ms. The fireball reaches a maximum radius of about 5 m shortly after detachment. The shock approaches a constant speed, near the speed of sound, $M = 1.06$, at $t = 30$ ms.

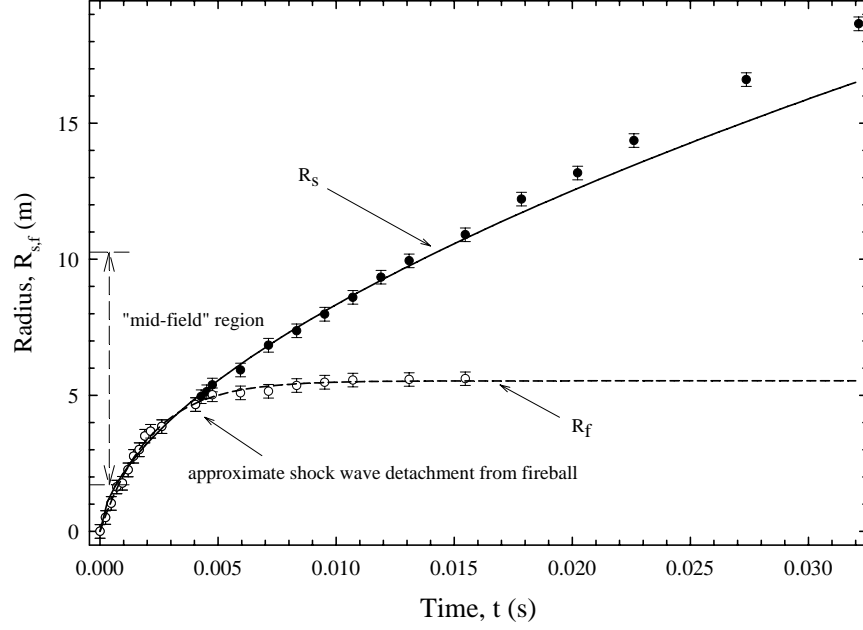


Figure 11. A fit of the (—) blast model and (---) exponential drag model to the (●) shock front radius, R_s , and (○) fireball radius, R_f , for event E7. The annotated mid-field region indicates the general range of data points within which the Sedov-Taylor blast theory model was fit. Note the approximate time and corresponding distance at which the shock wave detaches from the fireball.

The Sedov-Taylor blast model [54, 60] is used to further characterize the propagation of the shock wave:

$$R_s(t) = a t^b \quad (1)$$

where

$$b = (s + 2)/(n + 2) \quad (2)$$

n = expansion dimensionality ($n = 1$ planar, $n = 2$ cylindrical, and $n = 3$ spherical)

s = factor relating rate of energy release ($s = 0$ instantaneous, $s = 1$ constant rate)

The energy released in the detonation, E_d , is characterized, via a length scale, l_o , a time scale, τ_o , and the atmospheric mass density, ρ , as [8, 53-54]:

$$a = \left(\frac{E_d / (\tau_o^s l_o^{3-n})}{\rho} \right)^{1/(n+2)} \quad (3)$$

For $n = 3$, $s = 0$, the length and time scales do not contribute to the interpretation of the energy released. For $n = 3$, $s = 1$, the factor E_d/τ_o may be interpreted as the rate of energy release. Applicability of the Sedov-Taylor expression is limited to the mid field as described in Eq. (4), where the shock has expanded to displace a mass of air exceeding the mass of the explosive, m , but the pressure differential across the shock is still significant compared to the ambient background pressure, P [43]:

$$\left(\frac{3m}{2\pi\rho}\right)^{\frac{1}{3}} \ll R_s \ll \left(\frac{\Delta H_d}{P}\right)^{\frac{1}{3}} \quad (4)$$

A reflected wave can produce a stronger Mach wave when combined with the initial shock wave [4, p. 13]. The test articles in the present work are sufficiently elevated above the ground surface such that the ground-reflected shock front has not yet combined with the initial shock during the temporal regime that the Sedov-Taylor blast model is fitted to the shock front data. The Sedov-Taylor model is thus still applicable to the present analysis. Examination of high speed visible imagery confirms that in the mid-field region, only the initial shock wave front is being modeled by the Sedov-Taylor model. From Eq. (3), a length scale is necessary for the proper interpretation of the energy and may be defined as the beginning of the mid field:

$$l_o = \left(\frac{3m}{2\pi\rho}\right)^{\frac{1}{3}} \quad (5)$$

The use of the device length (0.4064 m) as the length scale results in low derived detonation energies, E_d . Using Eq. (7) and Eq. (8), the corresponding efficiencies are also low and never exceed 6% when the $s = 1$ (constant energy release) condition is assumed.

The beginning of the mid field is thus the preferred characteristic length scale in the interpretation of energy released. The corresponding time to reach the mid field, τ_o , assuming the ideal detonation wave velocity for RDX at theoretical maximum density (TMD), $v_{RDX} = 8.8$ km/s [14], is

$$\tau_o = l_o / v_{RDX} \quad (6)$$

For pure RDX at TMD of 1.81 g/cm³, its detonation wave traveling at 8.8 km/s can traverse the length of the 0.4064 m test article in about 46.2 μ s. The atmospheric conditions and corresponding length and time scales for each event are provided in Table 4. Figure 11 illustrates the mid field for event E7 extends from 1.2–10.2 m. The camera captures the expansion well before and after the mid field. The shock detaches from the fireball about half way through the mid field.

Table 5. Fit Parameters from shock expansion and fireball drag

Event	Sedov-Taylor ($b=0.6$)		Sedov-Taylor Model					Drag Model				
	a	δa	a	δa	b	δb	RMSE	R_m (m)	δR_m (m)	k (s ⁻¹)	δk (s ⁻¹)	RMSE
E13	136	1	144	11	0.611	0.017	0.145	5.76	0.13	426	20	0.049
E5	138	3	159	19	0.631	0.025	0.185	4.90	0.12	527	38	0.122
E10	133	1	132	8	0.599	0.012	0.074	4.54	0.07	609	27	0.077
E8	136	2	135	26	0.599	0.037	0.198	5.57	0.13	422	27	0.121
E4	134	1	137	15	0.604	0.023	0.177	5.05	0.15	500	52	0.204
E17	136	2	156	15	0.629	0.020	0.183	5.31	0.11	455	27	0.128
E12	132	2	153	18	0.630	0.025	0.226	5.07	0.11	509	34	0.142
E16	134	4	188	12	0.674	0.014	0.138	5.08	0.08	431	20	0.096
E7	132	2	125	18	0.588	0.029	0.190	5.53	0.10	470	27	0.115
E11	130	2	165	9	0.651	0.012	0.107	5.66	0.15	360	26	0.172
E6	125	3	186	15	0.689	0.019	0.198	5.15	0.22	374	42	0.227
E15	122	3	186	12	0.693	0.014	0.114	4.31	0.24	457	39	0.143
E3	111	2	189	21	0.712	0.023	0.168	4.81	0.24	327	30	0.032

A fit of Eq. (1) to the observed shock expansion for event E7 is illustrated in Figure 11. The description is adequate throughout the mid field. The transition to a sonic shock, $M = 1$, in the far field is not well captured by the Sedov-Taylor model. The resulting fit parameters, a and b , and their associated uncertainties, δa and δb , for each event are reported in Table 5. The uncertainties are defined as half of the difference between the upper and lower intervals of the 95 % confidence bounds of the fit. Fits are also reported for the case where the exponent is constrained to $b = 0.6$ (the case for $n = 3$, $s = 1$). Table 4 also lists the fit parameters and uncertainties of the drag model fit to data. The drag model is defined by Eq. (9) in § 4.3.

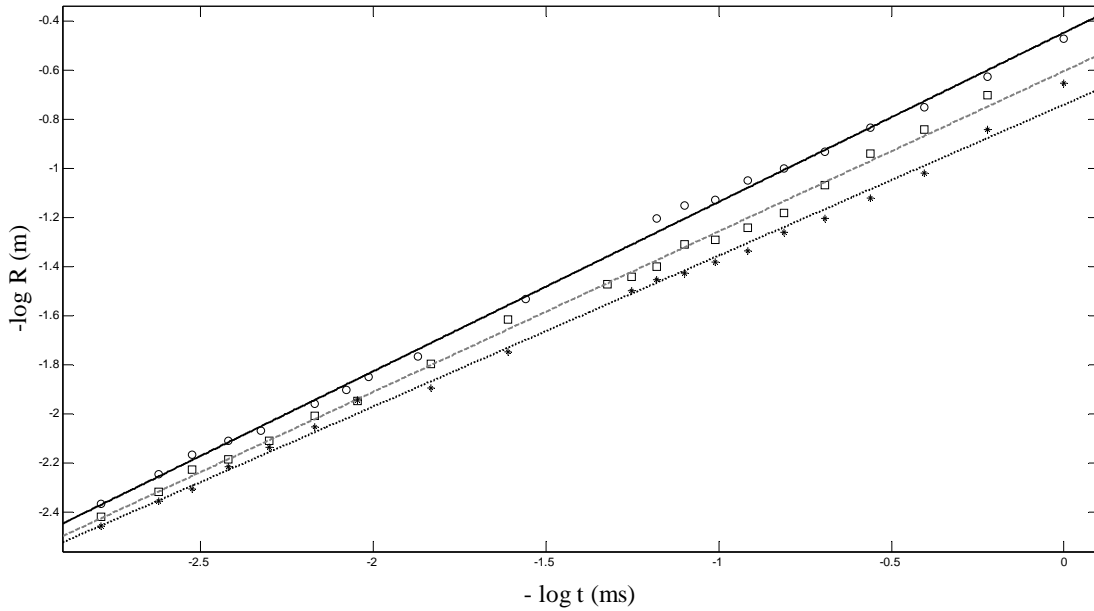


Figure 12. Log-log plot of shock expansion and the two-parameter power law fit for events (\square) E11, ($*$) E13, and (\circ) E15 showing the relative spread of the blast model fits for $t = 0$ –20 ms.

A log-log plot of the shock expansion for several events is provided in Figure 12. The small, but readily discernible variations in intercept and slope correspond to

variations in the two fit parameters. It is the trend in these slopes and intercepts with munitions characteristics, particularly the weight fractions, which is analyzed in the present work.

Table 6. Interpretation of shock dynamics

Event	Fix $s = 1$, $n = 3$			Fix $s = 0$		Fix $s = 1$					Fix $n = 3$			Calculated ΔH_d	
	dE_d/dt (GW)	E_d (MJ)	τ_{RDX} (ms)	E_d (MJ)	n	dE_d/dt (GW)	E_d (MJ)	τ_{RDX} (ms)	η	n	E_d (MJ)	η	s	RDX (MJ)	HE (MJ)
E13	57.05	8.07	1.07	20.41	1.27	48.28	6.83	1.26	0.11	2.91	9.46	0.16	1.06	60.99	126.59
E5	60.98	8.59	1.01	17.68	1.17	39.01	5.49	1.57	0.09	2.76	13.30	0.22	1.15	61.30	130.54
E10	51.37	7.68	1.44	23.79	1.34	52.20	7.80	1.42	0.11	3.01	7.47	0.10	0.99	74.05	138.28
E8	58.72	8.79	1.26	25.98	1.34	59.51	8.91	1.24	0.12	3.01	8.60	0.12	0.99	74.03	138.14
E4	57.40	7.38	0.86	19.12	1.31	53.69	6.90	0.92	0.14	2.97	7.76	0.16	1.02	49.14	104.59
E17	54.85	7.25	0.89	14.86	1.18	35.88	4.74	1.36	0.10	2.77	10.91	0.22	1.14	48.96	104.19
E12	52.54	7.22	1.13	15.75	1.17	34.16	4.70	1.74	0.08	2.76	11.10	0.19	1.15	59.33	110.80
E16	55.27	7.64	1.07	10.68	0.97	18.99	2.62	3.12	0.04	2.45	19.89	0.34	1.37	59.26	110.62
E7	52.55	7.22	1.13	23.71	1.40	63.27	8.69	0.93	0.15	3.10	6.06	0.10	0.94	59.15	110.40
E11	45.34	5.60	0.90	9.26	1.07	20.74	2.56	1.96	0.06	2.61	10.68	0.26	1.25	40.63	80.60
E6	38.77	3.98	0.64	4.01	0.90	9.13	0.94	2.71	0.04	2.35	10.59	0.43	1.45	24.71	52.60
E15	33.61	3.46	0.73	3.69	0.89	8.05	0.83	3.04	0.03	2.33	10.14	0.41	1.46	24.50	52.18
E3	22.37	2.43	1.32	2.93	0.81	4.93	0.54	5.98	0.02	2.21	9.85	0.33	1.56	29.51	55.14

The two fit parameters, a and b , are insufficient to fully determine the dimensionality, n , rate of energy release, s , and energy released, E_d . Several cases for interpreting the dimensionality and energy release constants are provided in Table 6. The case when the exponent is constrained to $b = 0.6$, yields detonation energies of 2.4–8.8 MJ. These solutions are constrained to $s = 1$ corresponding to rates of energy release of 22.4–61.0 GW, assuming the theoretical RDX detonation velocities and time scales of 0.11–0.15 ms reported in Table 4. However, one would expect considerably more energy release under ideal conditions, as the theoretical heats of detonation are reported in Table 6 as 24.5–74.1 MJ. One method of characterizing the efficiency would be to define a new time scale where the detonation energy is released over a longer period:

$$\tau_{RDX} \equiv \frac{\Delta H_{d_RDX}}{dE_d/dt} \quad (7)$$

Given a ΔH_{d_RDX} in Eq. (7), a large τ_{RDX} suggests that the rate of energy release, dE_d/dt , is small. Describing efficiency in terms of a time scale is thus reasonable since it is related to the rate of energy release in the detonation. Values for this time scale of 0.64–1.44 ms are considerably longer than the ideal RDX detonation time scales of 0.10–0.15 ms. Efficiency can thus be defined using a ratio of energies or a ratio of time scales:

$$\eta = \frac{E_d}{\Delta H_{d_RDX}} = \frac{\tau_o}{\tau_{RDX}} \quad (8)$$

It is worth noting presently that 100% efficiency or complete conversion of the theoretical heat of detonation into a blast wave is not possible. The detonation energy is partitioned into several processes that reduce the amount of energy available for the production of a blast wave. For cased charges, fragmenting the steel case, accelerating the case fragments, radiating photons, and heating the detonation products are examples of processes that can channel detonation energy away from blast wave production. As mentioned in Chapter II § 2, RDX detonation pressure is roughly two orders of magnitude greater than the case strength for a typical steel case. For the mild steel case in the present work, it is reasonable to assume that less than 1% of the detonation energy is required to rupture the steel casing material [45, p. 71]. The test articles in the present work are considered moderate to heavily cased charges since the 27.2 kg (~ 60 lb.) steel case in the present work gives case-to-charge mass ratios that range from 1.6–4. A case-to-charge mass ratio in this range could result in casing fragment kinetic energy that is about 50% of the detonation energy [45, p. 69]. In other words, up to about half of the

detonation energy could be used in propelling the case fragments. Less than 1% of the detonation energy is “lost in the form of thermal and visible radiation” [45, p. 75]. The remainder of the detonation energy is available to generate a blast wave. The detonation efficiencies resulting from this work may be under-estimating the actual efficiencies as we have not taken into account the precise energy losses due to casing fragment kinetic energy and thermal heating of the product gases.

The magnitude of the efficiencies depend upon the length, l_o , and time, τ_o , scale factors. Examination of the fit residuals for $b = 0.6$ shows that for some events (E3, 5, 6, 11, 15-17) the one-parameter power law over-estimates the blast wave radius in the first half of the mid-field region and under-estimates the radius in the last half of the mid-field region.

The uncertainty in the parameter b when unconstrained is rather small, about 5% or $\Delta b \cong 0.02$, and the variation across all events is considerably larger $b = 0.59\text{--}0.71$. Furthermore, the exponent systematically increases as high explosive weight decreases. Thus, the constraint $b = 0.6$ is not justified by the data. In an ideal point blast, $b = 0.4$ ($s = 0$ and $n = 3$). However, we observed $b = 0.59\text{--}0.71$ (± 0.02) indicating blast dimensionality $n < 3$ or non-instantaneous energy release $s > 0$. Misra and Thareja [43] report values for b ranging from 0.33–0.90. In laser-generated shock wave studies, they observed that b decreases as the initial energy increases and that b also decreases if the ambient atmospheric pressure is increased. In the present study, we did observe a similar decrease in b as the calculated theoretical heat of detonation increased.

For instantaneous energy release, $s = 0$, the fit parameters yield a dimensionality of $n = 0.81$ to 1.40 (i.e., somewhere between that of a planar and cylindrical geometry).

However, the observed images appear nearly hemispherical. Furthermore, the detonation energies are as high as 26 MJ, approaching 40% of the RDX heat of detonation. Previous studies have observed detonation efficiencies of 12–85 percent [8, 16, 35, 40, 43, 54, 60, 67] depending on test conditions. The most efficient cases involve laser ablation with a time-dependent delivery of initial energy such as a rising laser pulse [40] or an ideal point blast in ambient air atmosphere with a specific heat ratio of 1.4. [54] The limit of instantaneous energy release with a corresponding cylindrical dimensionality appears inconsistent with physical interpretation of the fit parameters.

When $n = 3$ (spherical shock wave) the energy release factor, s , ranges from 0.94–1.56 with a mean and standard deviation of 1.22 and 0.20 and the detonation energy ranges from 7.7–19.9 MJ. However, as will be discussed shortly in § 4.2, the detonation energy does not trend with the amount of high explosive present thus making the $n = 3$ condition suspect. For a constant energy release, $s = 1$, the dimensionality becomes more spherical as the values range from $n = 2.21$ – 3.10 with a mean and standard deviation of 2.68 and 0.28. We do anticipate a value of $n \leq 3$, due to ground interactions and the hemispherical expansion. Clearly, the present data is best described by a solution where $n \cong 3$ and $s \cong 1$. For the constraint $s = 1$, Table 6 provides rate of energy release of 4.9–63.3 GW corresponding to detonation energies of 0.54–8.9 MJ. The time scales for energy release from Eq. (7) are longer, $\tau_{\text{RDX}} = 0.92$ – 5.98 ms, than those defined by the RDX detonation velocity at TMD, of $\tau_0 = 0.11$ – 0.15 ms. For the $s = 1$ constraint, this is consistent with efficiencies of $\eta = 2$ – 15% .

4.2 Influence of liner and aluminum on detonation energy

The interpretation of the shock dynamics depends critically upon the assumptions regarding dimensionality of the expansion. The efficiency, η , and dimensionality, n , derived from the Sedov-Taylor model assuming a constant rate of energy release, $s = 1$, increases significantly as the fraction of the test article's weight allocated to high explosive increases, as shown in Figure 13. Event E3 with only 43% of the weight allocated to high explosive (36% RDX), exhibits a very low energy released with $E_d = 0.54$ MJ, relative to the RDX heat of detonation of 29.5 MJ. The efficiencies, $\eta = 2\text{--}15\%$, are low and may reflect the rather stable composition of the munitions. In general, the efficiency increases as more high explosive is present, and the fraction of the weight allocated to liner decreases. In this view, the liner appears to contribute little to the destructive shock effects.

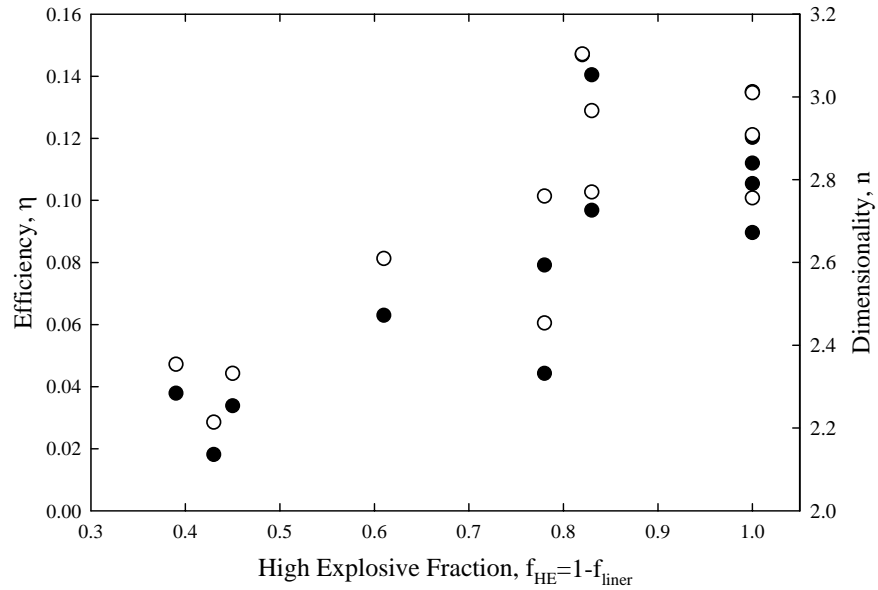


Figure 13. Dependence of shock parameters: (●) energy efficiency, η , and (○) dimensionality, n , on fraction of weight allocated to high explosive for constant energy release, $s = 1$.

Alternatively, the efficiency decreases with the fraction of high explosive when the dimensionality is constrained to $n = 3$. Figure 14 demonstrates larger efficiencies, $\eta = 10\text{--}43\%$ when the rate of energy release is allowed to vary from $s = 0.94\text{--}1.56 (\pm 0.2)$. However, open-air free-field detonations of conventional munitions suggests that although longitudinal symmetry may exist, blast waves are not spherical for typical warheads where overpressure and blast can vary greatly with the angle defined from the test item's longitudinal axis [1]. Figure 14 suggests that the efficiency can be as high as 43% yet the initial Mach speed as discussed in § 4.3 is a factor of 3-4 lower than the peak theoretical shock speed. Thus, we prefer a blast wave interpretation of $s = 1$ as it is still consistent with the overall present analysis.

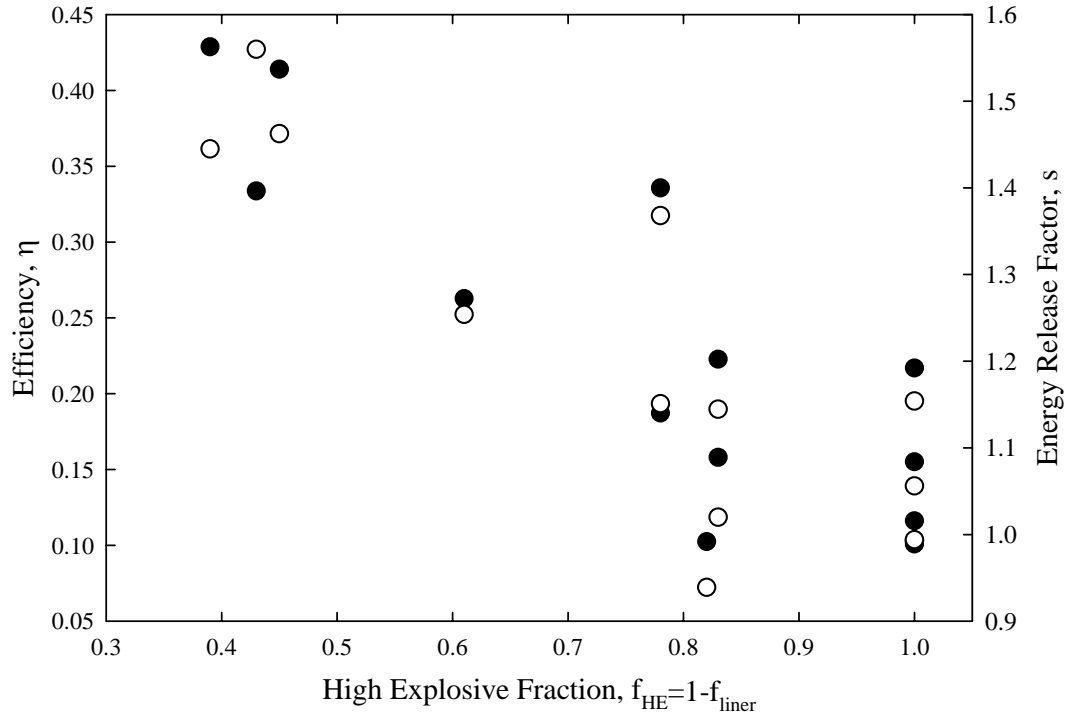


Figure 14. Dependence of shock parameters: (●) energy efficiency, η , and (○) energy release factor, s , on fraction of weight allocated to high explosive for spherical expansion, $n = 3$.

We can examine the influence of the liner and aluminum further by noting from Table 3 that in the present test item configurations, total weight percent aluminum increases as the liner weight increases. There is an 88% correlation between liner weight and total weight percent aluminum in the test articles. Analysis can be approached from both points of view. Analyzing the test articles using liner weight (via its complementary fractional relation to the HE weight, $f_{\text{HE}} = 1 - f_{\text{liner}}$) allows a more intuitive interpretation of detonation energies and efficiencies. This is important in light of our initial assumption that the HE participates fully in the detonation reaction whereas the liner does not and that the liner contributes mostly to the post-detonation combustion.

Subcategorizing the detonation energies using liner volume percent may be an alternative approach. At constant energy release, $s = 1$, three test articles (event E6, E15, and E3) with the highest liner volume at 60% produced the lowest detonation energies. This may suggest that the liner does not play a large active role in the detonation reaction. This might be because a large volume displaces a proportionate amount of HE needed for detonation or perhaps the anisotropy created between the HE and the annular liner in the munition fill hinders the detonation. Events with no liner present generally tended to produce the highest blast wave energies. Test articles with 20% liner volume provided the widest spread in detonation energies when the events were subcategorized by percent liner volume.

One might anticipate that aluminum content would contribute more to the afterburning than the detonation shock. Aluminum in the HE tends to react at a later time when it burns favorably with detonation products especially in the presence of atmospheric oxygen [9]. If aluminum reacts later, then the rate of energy release (dE/dt)

is less thus resulting in a slower shock front. The heat release from aluminum might be realized later during the post-detonation combustion phase.

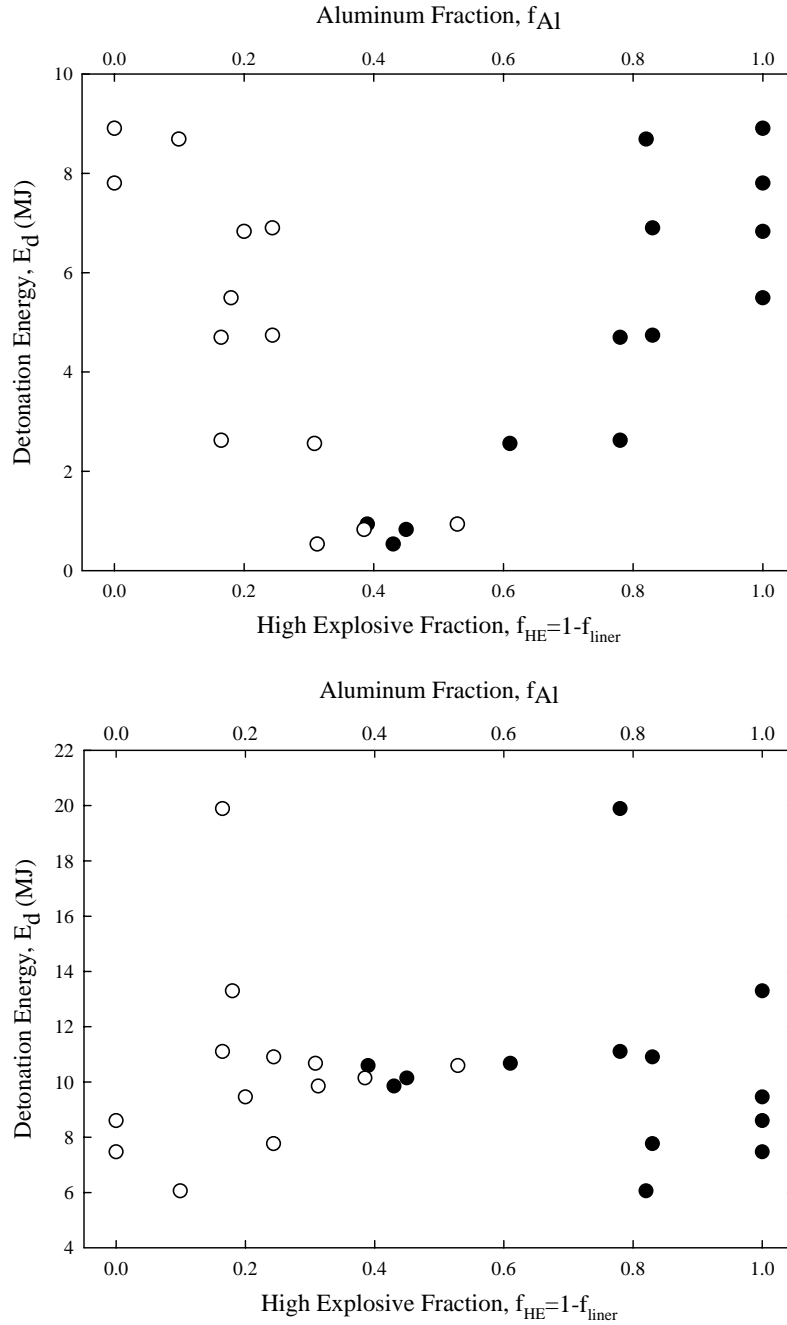


Figure 15. Scaling of detonation energy with (●) HE and (○) aluminum weight fractions for (a) $s=1$ and (b) $n=3$.

The influence of aluminum content is further explored in Figure 15. The inverse relationship between shock energy and total weight percent aluminum when the $s = 1$ constraint is imposed reinforces the notion that there is a tradeoff between the amount of HE and the amount of aluminum in the test article. On the other hand, when the dimensionality is constrained to $n = 3$, the shock energy is rather independent of both HE and overall aluminum content in the test article. As discussed above, a purely spherical ($n = 3$) interpretation of the blast dimensionality is not supported by previous field detonations of typical conventional munitions, of which the present test articles are surrogates. We thus prefer the $s = 1$ constraint when analyzing the present work.

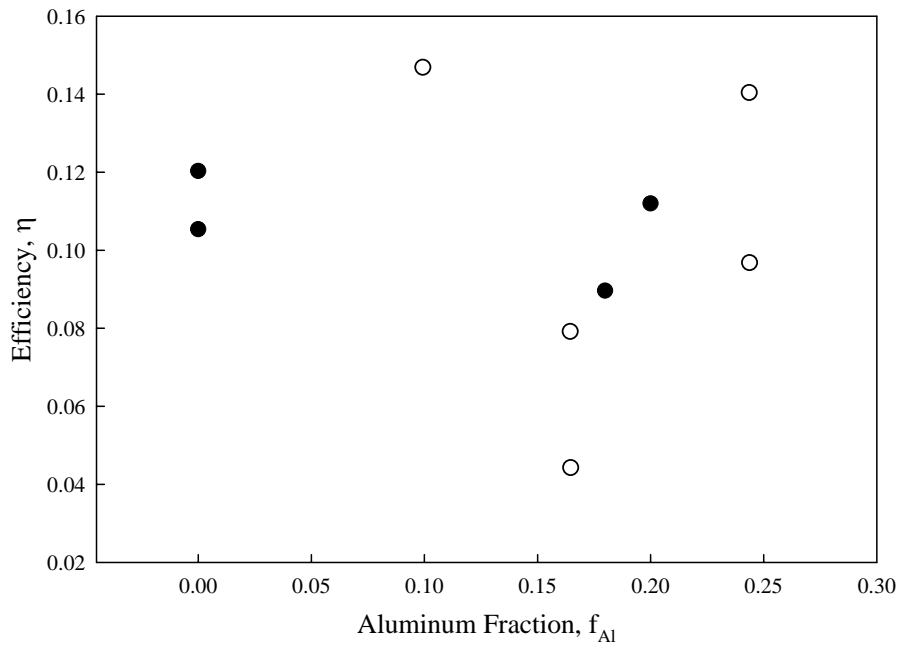


Figure 16. Influence of aluminum content for events with (●) no liner and (○) 17–22 % liner by weight.

To further study the influence of aluminum on efficiency, we examine those events with HE fractions of about 0.8 and 1.0. The resultant analysis in Figure 16 shows

no clear relationship between overall aluminum fractional weight and efficiency for these selected events. It is possible that the distribution of the aluminum content to both the HE and liner is responsible for this lack of correlation.

4.3 Fireball dynamics

The drag model [22] is chosen to study the behavior of the fireball size:

$$R_f(t) = R_m(1 - e^{-kt}) \quad (9)$$

where

R_m = stopping distance

k = drag coefficient

Table 7. Interpretation of fireball dynamics

Event	Fireball Initial Speed				Fireball Speed at l_o			Fireball Lofting Speed		
	$v_o = R_m k$ (km/s)	v_o / v_{RDX}	a (m/s)	M_o	$t(l_o)$ (ms)	$R_m k e^{-kt}$ (km/s)	$M(l_o)$	H_1 (m)	H_2 (m)	Loft Rate (m/s)
E13	2.45	0.28	343	7.15	0.57	1.92	5.60	11.89	14.32	11.1
E5	2.58	0.29	340	7.59	0.55	1.93	5.67	11.48	13.02	7.2
E10	2.77	0.31	338	8.18	0.56	1.96	5.81	12.38	14.75	10.9
E8	2.35	0.27	339	6.92	0.64	1.79	5.29	12.94	14.95	8.3
E4	2.53	0.29	332	7.61	0.51	1.96	5.91	11.77	14.19	11.4
E17	2.41	0.27	345	7.00	0.54	1.89	5.47	12.24	14.31	9.7
E12	2.58	0.29	333	7.74	0.54	1.96	5.89	12.73	15.27	11.9
E16	2.19	0.25	336	6.52	0.64	1.66	4.96	12.21	14.40	10.4
E7	2.60	0.30	334	7.79	0.52	2.03	6.08	12.77	14.72	9.3
E11	2.04	0.23	342	5.95	0.59	1.65	4.81	13.35	15.71	10.9
E6	1.92	0.22	333	5.78	0.52	1.59	4.76	11.98	14.35	11.3
E15	1.97	0.22	336	5.87	0.52	1.56	4.63	12.36	14.78	11.1
E3	1.57	0.18	333	4.72	0.68	1.26	3.78	11.38	13.69	10.8

The observed fireball size is fit to Eq. (9) and compared to the shock wave expansion for event E7 in Figure 11. Tracking the fireball front is key to shock wave analysis since the early fireball front and shock wave front are coincident up until shock wave detachment

from the fireball. Thus at early times immediately after detonation and before shock wave detachment, the fireball front in the mid-field region is used to represent the shock wave front during the Sedov-Taylor blast model fit.

Results of the drag model fit for each event are provided in Table 5 and interpreted in Table 7. The maximum fireball radii range from 4.3 to 5.8 m with an average of 5.1 m. Initial analysis of infrared spectra from previously analyzed Fourier transform spectroscopy signatures established emissive radii ranging from 3.69 to 7.17 m with an average maximum fireball emissive-radius of 5.80 m. The average maximum emissive-radius and the average drag model radius agree to within $\sim 12\%$. The fireball size quickly approaches its maximum value within 30–50 ms after initiation, with witness camera video showing a fairly constant fireball size by 150–200 ms.

Shock wave detachment times range from 1.9 to 3.4 ms with an average detachment time of 2.7 ms corresponding to an average radial distance of about 3.7 m from detonation origin. Recent radiometer analysis of improvised explosive device (IED) detonations [57] suggests that the shock wave may be detaching from the luminous IED fireball at around 1.1–1.5 ms.

The dependence of initial velocity and stopping distance on HE weight is provided in Figure 17. The detonation velocity for RDX at theoretical maximum density (TMD) is 8.8 km/s [14] whereas the initial detonation velocities obtained from drag model analysis ranges from 1.57 to 2.77 km/s (Mach 4.6 to 7.5). The test article initial velocities increase significantly with high explosive weight and are about a factor of three lower in magnitude than the detonation velocity of RDX at TMD. In addition to steel confinement, the presence of aluminum and wax in the HE as well as the presence of the

aluminized PE annulus surrounding the HE may influence the non-ideality of the detonation. Since the detonation energy is defined as the sum of the kinetic energy and thermal energy in the explosion [54, 60], a factor of three decrease in detonation velocity will likely result in a proportional decrease in efficiency according to Eq. (8). This may partially explain the low energy efficiencies observed in Table 6.

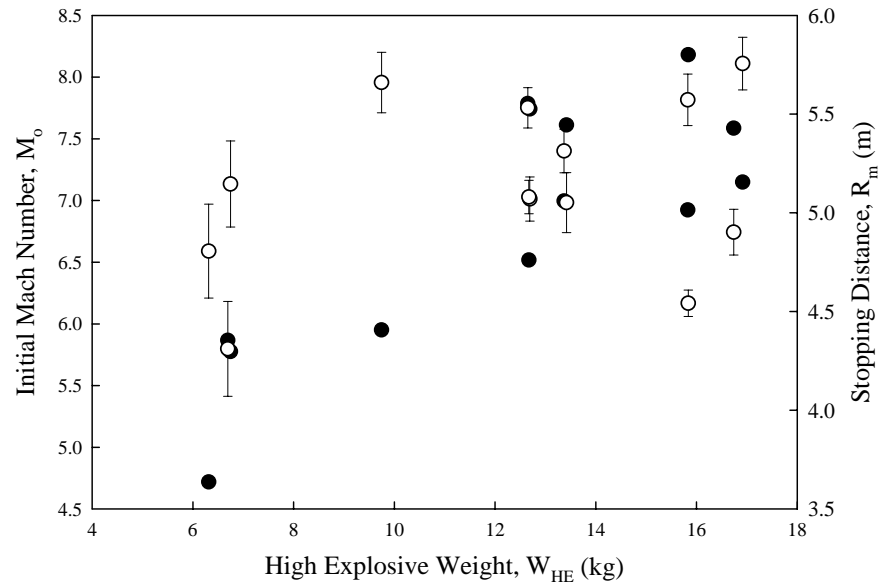


Figure 17. (●) Initial velocity and (○) stopping distance for the emissive fireball.

At longer times, $t \sim 0.3$ s, the fireball lofts as illustrated in Figure 10. The fireball size remains about 4–6 m in diameter as the combustion proceeds and the fireball cools. The height of the fireball is measured from the detonation origin to the top of the PDPC plume. The rate of fireball rise approaches a constant value at about 0.25 s as illustrated in Figure 18. These lofting rates for each event are summarized in Table 7. This phenomenon is possibly related to buoyancy of the fireball. As will be discussed further in Chapter V § 3.3, there is a 75% correlation between the PDPC rise slope and the

empirical model fit parameters describing the fireball temperature suggesting a relationship between rise slope and fireball temperature. However, the data set is too sparse and the variability in the atmospheric wind speeds is too great for a definitive examination.

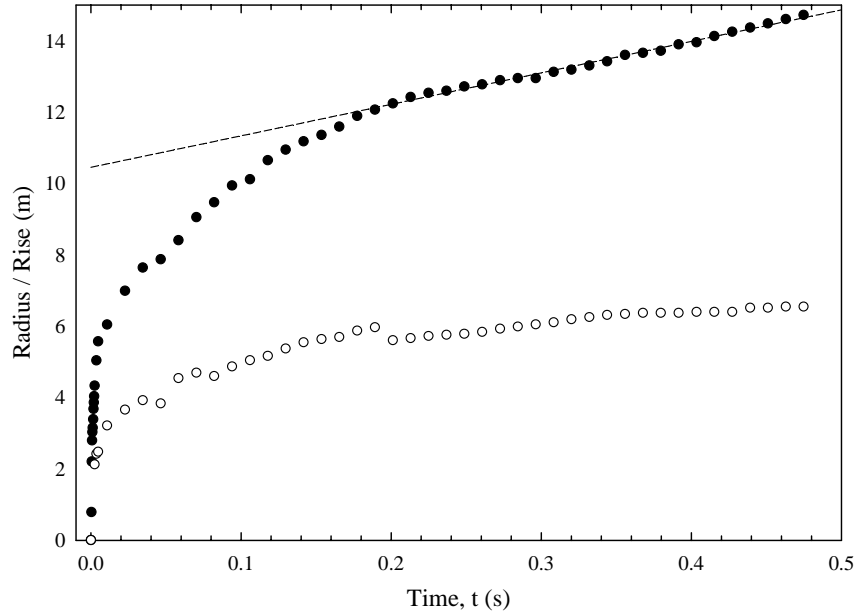


Figure 18. Temporal evolution of the fireball: (○) radius and (●) loft height at longer times. The fireball rise begins to approach a constant rate beginning at approximately 0.25 s.

5. Concluding remarks

Fireball and shock wave analysis allows the extraction of key features of the detonation event. The drag model gives a good estimate of the fireball radius as 5 m as well as shows the rapid growth of the fireball upon detonation. Subsequent study of the post-detonation combustion emissivity may benefit from the assumption of a rapid growth to a constant size fireball. Analysis of the shock wave using the Sedov-Taylor blast wave theory is essential to estimating the shock energy and corresponding energy

conversion efficiency of the detonation. Key to the proper interpretation of the blast model energy parameter is the use of the characteristic length scale, l_o , and time scale, τ_o . Directly related to shock energy is the initial velocity of the shock wave. The fit-derived initial velocity is roughly a factor of three lower in magnitude than the theoretical detonation velocity of the main HE constituent, RDX, and may help explain why the blast energies are low. The Sedov-Taylor blast model fit to data is best interpreted using a constant energy release factor, $s = 1$, occurring within the first 1–6 ms after detonation with blast dimensionality approaching but not equal to a spherical geometry. Fraction of high explosive correlated with efficiency favors the $s = 1$ vice the $n = 3$ interpretation since the positive correlation between HE fraction and detonation energy is more intuitive and consistent with the other findings in the analyses. Liner fraction is favored over aluminum content as the preferred means by which to sub-categorize and discriminate between blast energies and efficiencies in the present work.

V. Evolution of Fireball Temperature after the Detonation of Aluminized RDX

Overview

Mid-wave infrared spectra ($1,800\text{--}10,000\text{ cm}^{-1}$) have been observed and analyzed to characterize the evolving temperature of fireballs resulting from the detonation of aluminized RDX. The field detonations of 12 high explosive compositions of RDX with varying aluminum and liner volumes were remotely observed with a suite of imagers, spectrometers and radiometers. Both a radiative transfer model and two-band radiometry have been used to determine fireball temperatures from the infrared spectra. The temperatures decay from initial values of $1290\text{--}1850\text{ K}$ to less than 1000 K during a 1 s interval. Secondary maxima are observed in the temperature profiles indicating significant post-detonation combustion. The rates for radiative cooling and post-detonation combustion are determined from an empirical model of the evolving temperatures. The observed heat released in the secondary combustion is well correlated with the high explosive and liner theoretical heats of combustion with an average efficiency of about 50%. Combustion and heat release increases as the fraction of the explosive weight allocated to the liner increases. Fireball lofting rates increase by more than 50% for events where the combustion heat release increases by a factor of two.

1. Introduction

Optical forensics of explosion events is important not only to the military but to civilian safety as well. It can play a vital role in tracking the chain of events leading to a detonation event by possibly identifying key spectral characteristics and even molecules in the fireball that may serve as the fingerprint for a particular

explosive type used. To this end, our research group has developed methods and models [20, 28-32, 47] able to differentiate between trinitrotoluene (TNT)-based versus enhanced novel explosives, cased versus uncased detonations, and air-dropped versus static detonations.

Aluminized explosives are another class of explosives that are becoming ubiquitous in modern munitions and as such deserved further study. The presence of aluminum in a high explosive (HE) is desired due to its large heat release during oxidation reactions [64]. Carney et al. [9] suggest that aluminum acts as an additional fuel in the explosion reaction beyond the detonation and that its oxide transients react favorably with detonation products especially when external atmospheric oxygen is present. Thus, it is widely believed that the addition of aluminum in HEs leads to improved performance.

Previous experimental works have extracted the temporal temperature profiles of open-air field explosions [3, 31-32, 34, 46]. Recent work by Wilkinson et al. [64] and Lewis and Rumchik [42] have noted post-detonation temperature trends using two-color pyrometry from chamber detonations of 20–40 g samples of octogen (HMX, $C_4H_8N_8O_8$) and cyclotrimethylene-trinitramine (RDX, $C_3H_6N_6O_6$). However, little work has been done on modeling the post-detonation temperature profile so that physically meaningful fit parameters can be extracted and translated into useable classification variables.

To improve the robustness of the currently available classification scheme, methods are needed to further differentiate between detonation fireballs resulting from explosives based solely upon a single explosive type. This chapter presents an

empirical approach able to model the temperature profiles from the post-detonation combustion fireballs of RDX-based enhanced novel munitions. Fourier-transform infrared signatures with a temporal resolution of 12–18 ms are collected from field detonations of enhanced novel munitions. The munitions are RDX-based aluminized high explosives surrounded by an aluminized plastic-bonded spin-cast liner all inside a steel munitions tube. The rate of change of temperature in the post-detonation combustion fireballs are modeled using a radiative cooling term and a double exponential combustion source term. Confidence in the physical meaning of the fit parameters is established through comparison with expected theoretical values and correlations to expected physical phenomena.

2. Experimental setup and explosive materials

A set of 22 novel aluminized munitions was detonated at a Department of Defense test site in Florida. Details of the test site have been reported previously. [26] The test items are 16” in. (0.41 m) tall mild steel tubes with 1/2” in. (0.013 m) thick walls and a 7” in. (0.18 m) inner diameter. The steel tubes are lined with an aluminized polyethylene (PE) annulus in the inner diameter and filled with melt-cast RDX-based high explosives (HE) with varying amounts of aluminum and paraffin wax binder. The test items are detonated 1.25 m above ground level atop a sacrificial wooden test stand. Table 8 specifies the amount of material present in the test items. The events in Table 8 and subsequent tables in this chapter are listed from least to most total number of moles in the test articles. The event nomenclature, E#, denotes chronological order in the test

sequence. Paraffin wax in the HE and PE in the liner are used as reasonable surrogates for the actual binders.

Table 8. Composition of test articles

Event Description	Moles of Material							
	RDX	Al HE	Wax	HE Total	PE	Al Liner	Liner Total	Total
E8 - SN19	59.19	0.00	7.64	66.83	0.00	0.00	0.00	66.83
E13 - SN21	48.77	33.19	7.69	89.65	0.00	0.00	0.00	89.65
E5 - SN20	49.02	29.54	8.09	86.65	0.00	0.00	0.00	86.65
E16 - SN03	47.38	0.00	6.12	53.50	31.75	26.25	58.00	111.50
E7 - SN07	47.30	0.00	6.11	53.41	44.71	15.04	59.75	113.16
E9 - SN11	39.17	23.62	6.46	69.25	31.75	26.25	58.00	127.25
E4 - SN15	39.29	23.71	6.48	69.48	44.71	15.04	59.75	129.23
E17 - SN14	39.15	23.62	6.46	69.23	44.71	15.04	59.75	128.97
E11 - SN01	32.49	8.59	4.72	45.79	77.92	39.73	117.65	163.44
E1 - SN04	23.80	0.00	3.08	26.88	95.09	78.34	173.43	200.32
E6 - SN13	19.76	11.92	3.26	34.94	95.09	78.34	173.43	208.37
E3 - SN08	23.60	0.00	3.05	26.65	133.81	44.93	178.74	205.39

The heat capacity, heat of detonation, and heat of combustion for each event are computed using reaction stoichiometry and NIST-JANNAF Thermochemical Table heats of formation and are summarized in Table 9.

Table 9. Thermodynamic properties of test articles

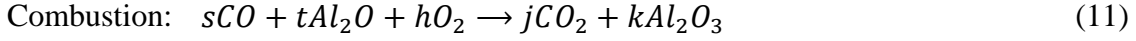
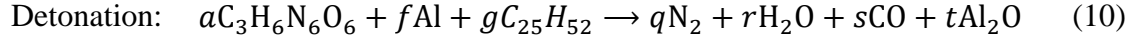
Event Description	Heat Capacity		Heat of Combustion, ΔH_c				Detonation, ΔH_d		Theoretical T_o
	$C_{p,c}$ (J/K)	$C_{p,d}$ (J/K)	RDX (kJ)	HE (kJ)	Liner (kJ)	Total (kJ)	RDX (kJ)	HE (kJ)	$\Delta H_{d,RDX} / C_{p,d}$ (K)
E8 - SN19	21.06	31.66	49.97	103.72	0.00	103.72	74.03	138.14	2338
E13 - SN21	21.50	29.55	41.17	120.29	0.00	120.29	60.99	126.60	2064
E5 - SN20	21.88	30.21	41.38	120.56	0.00	120.56	61.30	130.54	2029
E16 - SN03	25.05	29.51	40.00	83.06	64.27	147.33	59.26	110.62	2008
E7 - SN07	26.94	30.46	39.93	82.90	71.98	154.87	59.19	110.40	1943
E9 - SN11	25.65	28.28	33.06	96.28	64.27	160.55	48.98	104.21	1732
E4 - SN15	27.64	29.37	33.17	96.63	71.98	168.60	49.14	104.59	1673
E17 - SN14	27.57	29.28	33.05	96.26	71.98	168.24	48.96	104.19	1672
E11 - SN01	31.35	27.98	27.42	67.07	136.86	203.93	40.63	80.60	1452
E1 - SN04	32.98	25.19	20.09	41.76	192.26	234.02	29.77	55.61	1182
E6 - SN13	33.31	24.62	16.68	48.59	192.26	240.85	24.71	52.60	1004
E3 - SN08	38.64	28.08	19.92	41.41	215.35	256.75	29.51	55.14	1051

In order to reasonably estimate stoichiometric quantities of the detonation products for the secondary combustion phase, it was hypothesized that due to the geometry of the liner, only the HE completely participates in the detonation and explosion reaction and that the liner is fragmented but only partially participates in the explosion phase. The liner does, however, fully participate in the combustion phase of the explosion. This is not an unreasonable hypothesis as analysis of high speed visible imagery in Chapter IV suggests that the energy transferred to the shock wave of the explosion constitutes only about 2–15% of the expected RDX heat of detonation, assuming a constant release of energy.

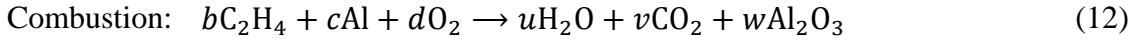
We can treat the combustion of the HE detonation products and combustion of the liner as two distinct processes, calculate their respective heats of combustion, and sum the two quantities to arrive at an overall heat of combustion for the event. Heat capacities are determined from reaction product species.

There are many elementary reactions and pathways that a reaction can take to get to the final products and the liberation of heat energy. As a simplifying assumption, we will only look at the overall reaction stoichiometry in order to determine the heats of detonation and combustion as well as product heat capacities. The temperature of 1300 K is selected as a reasonable temperature at which to use tabulated heats of formation from the NIST database [12] as this temperature is common to all detonation events. Following Cooper's [14] reaction product hierarchy rules of thumb and assuming a composite RDX-Al-wax HE surrounded by a PE-Al liner, the reaction stoichiometries are:

RDX-Al-wax HE



PE-Al Liner



To determine the heat of combustion, pounds of material are converted into equivalent moles and tabulated NIST heats of formation at 1300K are used in order to get:

$$\begin{aligned} \Delta H_{c(HE)} &= \# \text{ moles} * \Delta H_f^o(\text{products}) - \# \text{ moles} * \Delta H_f^o(\text{reactants}) \\ &= [j * \Delta H_f^o(CO_2) + k * \Delta H_f^o(Al_2O_3)] \\ &\quad - [s * \Delta H_f^o(CO) + t * \Delta H_f^o(Al_2O) + h * \Delta H_f^o(O_2)] \\ \Delta H_{c(Liner)} &= \# \text{ moles} * \Delta H_f^o(\text{products}) - \# \text{ moles} * \Delta H_f^o(\text{reactants}) \\ &= [u * \Delta H_f^o(H_2O) + v * \Delta H_f^o(CO_2) + w * \Delta H_f^o(Al_2O_3)] \\ &\quad - [b * \Delta H_f^o(P.E.) + c * \Delta H_f^o(Al) + d * \Delta H_f^o(O_2)] \end{aligned}$$

The detonation product heat capacity is computed using:

$$\begin{aligned} \sum n_i Cp_{i,1300K} &= (q \text{ moles} * Cp_{N_2}) + (r \text{ moles} * Cp_{H_2O}) + (s \text{ moles} * Cp_{CO}) \\ &\quad + (t \text{ moles} * Cp_{Al_2O}) + (b \text{ moles} * Cp_{C_2H_4}) + (c \text{ moles} * Cp_{Al}) \end{aligned}$$

and the combustion product heat capacity is computed using:

$$\sum n_i Cp_{i,1300} = [(j + v) \text{ moles} * Cp_{CO_2}] + [(k + w) \text{ moles} * Cp_{Al_2O_3}] + (u \text{ moles} * Cp_{H_2O})$$

Assuming RDX as the only HE constituent and neglecting the binder and aluminum content, the detonation and subsequent combustion process are partitioned according to the available oxygen:

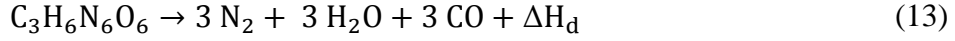


Table 9 shows the combustion product heat capacities, $C_{p,c}$, increase even as the amount of RDX in Table 8 decreases for each respective event. This is because the overall total number of moles increases as more PE-Al liner material is taken into account in the combustion stoichiometry. The displacement of a proportionate amount of HE as liner volume increases also explains the trends in the heats of detonation and combustion in Table 9.

An instrumentation suite consisting of an 82 Hz Fourier-transform spectrometer (FTS), 100 kHz four-band radiometer, high speed digital camera operating at 3000–4200 fps, and a standard witness audio-visual digital camera collected signatures from an unobstructed standoff distance of 335 m. FTS signatures are the primary data set used for the analysis in this chapter. The FTS was fitted with a 75 mrad telescope giving a 25 m diameter field-of-view (FOV) at the target. Bore-sighted video indicated that fireballs at peak area occupied only about 15 percent of the FOV and had a dwell time of about 1 s before ascending or migrating out of the FOV due to wind gusts. Meteorological conditions were recorded prior to each detonation event throughout the two-week data collection phase and are reported in Table 4. Of the 22 scheduled detonations, only 13

high speed digital camera signatures were successfully collected and only 12 of those 13 detonation events netted useable FTS spectra.

The ABB-Bomem MR-254 FTS operated at 82 Hz with a spectral resolution of 16 cm^{-1} ($\Delta\tilde{\nu} = 7.71 \text{ cm}^{-1}$) using InSb (1800–10,000 cm^{-1}) and InGaAs (5600–10,000 cm^{-1}) detectors. Some interferograms were collected at 8 cm^{-1} resolution at a rate of 56 Hz. The interferograms were oversampled at half-HeNe wavelengths putting the Nyquist frequency at 15,802 cm^{-1} . This is well beyond the response of the InSb and InGaAs detectors and thus sufficiently avoiding aliasing of the signal reconstruction during Fourier transformation. Only the mid-infrared spectra from the InSb detector are reported in the current work.

The FTS was calibrated in the field following a method detailed by Gordon et al. [26] and Gross [2628]. A low-temperature (283-353 K) wide-area blackbody (BB) source and a high-temperature (1523 K) cavity blackbody source were used to calibrate the FTS detector. The wide-area BB was positioned a few centimeters from the FTS entrance aperture and over-filled the FOV. Since instrument self-emission is important between 1750–2500 cm^{-1} , blackbody measurements enabled an accurate determination of both detector response (gain) and instrument self-emission (offset) between 1750–3000 cm^{-1} . An absolute scale for the relative gain curve between 3000–10,000 cm^{-1} was established by comparison with the gain curve previously found using the low temperature BB source where they overlap near 3000 cm^{-1} .

3. Results

3.1 Spectra

The infrared spectrum for event E9, with a temporal resolution of 12.1 ms, is illustrated in Figure 0a. A broadband emission, attenuated by the atmosphere, initially increases as the fireball grows and temperature increases.

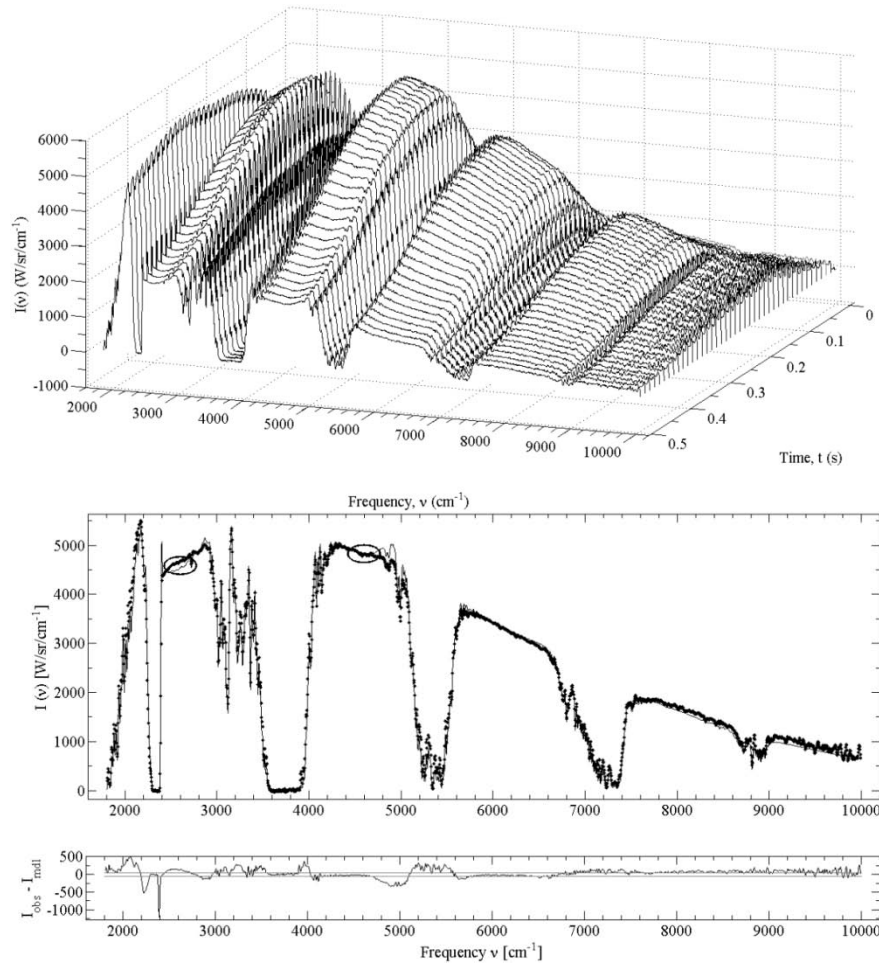


Figure 19. (a) Temporally-resolved spectra for event E9, and (b) the FTS observed spectral intensity (\bullet) of event E9 at 0.28 s after detonation. Two spectral regions: 2500–2700 and 4500–4700 cm^{-1} , of continuum radiation are indicated for the two-color temperature determination. A fit of the observed spectra (—) to the radiative transfer model of Eq. (15) yields fit residuals of $\sim 3.7\%$, except in the vicinity of the CO_2 4.3 μm band.

The subsequent decay is relatively long lived, > 1 s, and depends on spectral component. For example, the emission from CO_2 near 2360 cm^{-1} decays more slowly than the broader continuum. The 16 cm^{-1} resolution of the single spectrum at 0.28 s after detonation in Figure 0b is sufficient to discern gas phase emission from CO_2 and H_2O from the gray-body signal from soot, even in the presence of significant atmospheric attenuation. There are approximately 2126 spectral samples illustrated as individual data points.

A low-dimensionality radiative transfer model has previously been developed [28] to describe the fireball's source radiance. Assuming local thermodynamic equilibrium (LTE), negligible effects of scattering, cubic fireball geometry, fireball and atmospheric homogeneity, and large standoff distance, leads to the apparent source radiance:

$$I(\nu) = \tau_{atm}(\nu) r^2 \varepsilon(\nu) B(\nu; T) \quad (15)$$

where

$B(\nu; T)$ = Planckian distribution at temperature, T

$r^2 = A$ = fireball projected area

τ_{atm} = atmospheric transmission

$\varepsilon(\nu)$ = source emissivity

Absorption cross-sections, σ_i , for H_2O , CO_2 and CO at $T = 275 - 3000$ K are obtained from the HITRAN database [52] to express emissivity as:

$$\varepsilon(\nu) = 1 - \exp \left[-r \left(\kappa_p + \sum_i \zeta_i \sigma_i(\nu; T) \right) \right] \quad (16)$$

where

κ_p = particulate absorption coefficient

ζ_i = molecular concentration of specie i

The Boltzmann factor is included in the definition of the absorption cross-section since, under LTE, the line-strength defining the absorption cross-section varies with temperature according to the Boltzmann distribution [28, p. 55]. The simplified radiative transfer spectral model is realized by multiplying the source spectrum by the atmospheric transmittance and convolving it with the FTS instrument line shape. The state of the atmosphere and weather conditions has been previously reported in Table 4.

A fit of Eq. (15) to the spectrum is provided in Figure 0b, establishing a best estimate for the model parameters of $T = 1800 \pm 3.3$ K, $r = 4.7 \pm 0.04$ m, $\zeta_{CO_2} = 4.36 \pm 0.9 \times 10^{17} \text{ cm}^{-3}$, $\zeta_{H_2O} = 6.20 \pm 0.6 \times 10^{17} \text{ cm}^{-3}$, and $\kappa_p = 1.33 \pm 0.03 \times 10^{-3} \text{ cm}^{-1}$. The median relative error in the fit is 3.7%. The fireball radius extracted from the infrared spectrum compares favorably with the size previously determined from Chapter IV from high speed visible imagery of $R = 5.1 \pm 0.4$ m. The full temporal dependence of the fireball temperature determined from these spectral simulations for several events are provided in Figure 20.

For the present work, the spectral simulations are not necessary for an accurate determination of the temperatures. Figure 0b highlights two bands in the continuum region (Band1=2500–2700 cm^{-1} and Band2=4500–4700 cm^{-1}) of the measured spectrum where spectral intensities are compared to a theoretical Planckian distribution to determine the two-color temperature. The two-color best fit Planckian is numerically determined using the following relation:

$$\left(\frac{I(\nu; T)_{B2}}{I(\nu; T)_{B1}} \right)_{\text{th}} - \left[0.005 * \left(\frac{I(\nu; T)_{B2}}{I(\nu; T)_{B1}} \right)_{\text{th}} \right] \leq \left(\frac{I(\nu; T)_{B2}}{I(\nu; T)_{B1}} \right)_{\text{meas}} \leq \left(\frac{I(\nu; T)_{B2}}{I(\nu; T)_{B1}} \right)_{\text{th}} + \left[0.005 * \left(\frac{I(\nu; T)_{B2}}{I(\nu; T)_{B1}} \right)_{\text{th}} \right]$$

The measured spectral intensity ratio of Band 2 over Band 1 from the collected spectrum is compared to a theoretical spectral intensity ratio at the same spectral bands. As shown above, once the FTS-measured intensity ratio is within 1% of the theoretical Planckian intensity ratio, the temperature corresponding to the theoretical Planckian distribution is assigned to the FTS-measured spectrum at the respective time step. Temporal iteration of this process leads to the $T(t)$ profiles depicted in Figure 20. The chosen intensity ratio exhibits a nearly linear dependence of temperature in the range $T = 800\text{--}1900$ K, as shown in Figure 21. These two continuum region bands are chosen because they are both outside the atmospheric absorption bands as well as the emission bands from fireball plume and atmospheric constituents such as H_2O and CO_2 . The ratio of the FTS-measured intensities in Figure 0b is 1.0313 ± 0.005 corresponding to a temperature of 1828 ± 9.1 K.

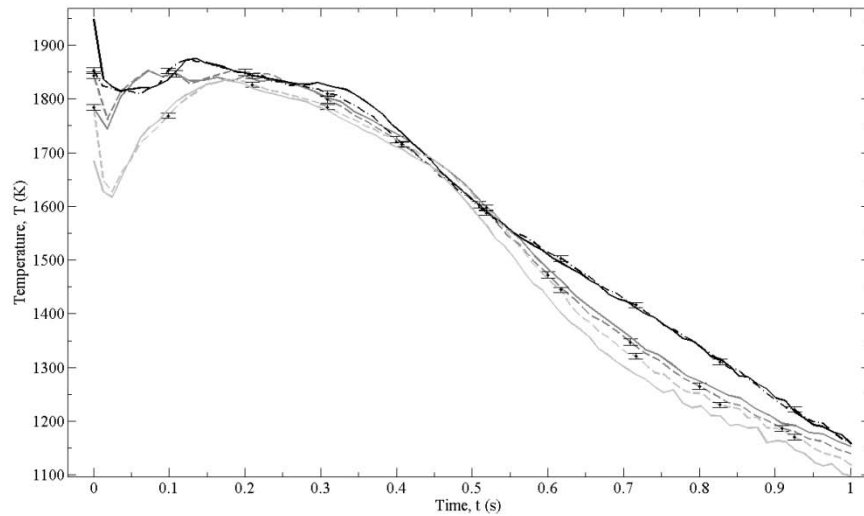


Figure 20. Comparison of temperature profiles from: (---) the spectral model of Eq. (15) and (—) the two-color Planckian method for events: (—) E9, (---) E4 and (---) E17.

Recall that the RDX-based HEs in the present work are under-oxidized. Upon detonation, heated carbonaceous soot and other particulates further undergo oxidation reactions in the turbulent fireball. However, the concentrations of these particulates appear to decay slowly enough in the 1 s time-window after detonation so that an assumption of blackbody emissions from the fireball is still applicable. This notion seems to be validated by comparison of the temperature profiles in Figure 20 where the two-color best-fit Planckian profile closely trends with the spectral model-derived temperature profile. Because of this slow decay, the measured spectra sufficiently exhibit blackbody behavior and thus allow a valid means for comparison of measured spectral intensity ratios with calculated theoretical Planckian intensity ratios. The FTS temporal resolution of 12 ms is not fine enough to allow monitoring of the extremely rapid temperature rise immediately after detonation.

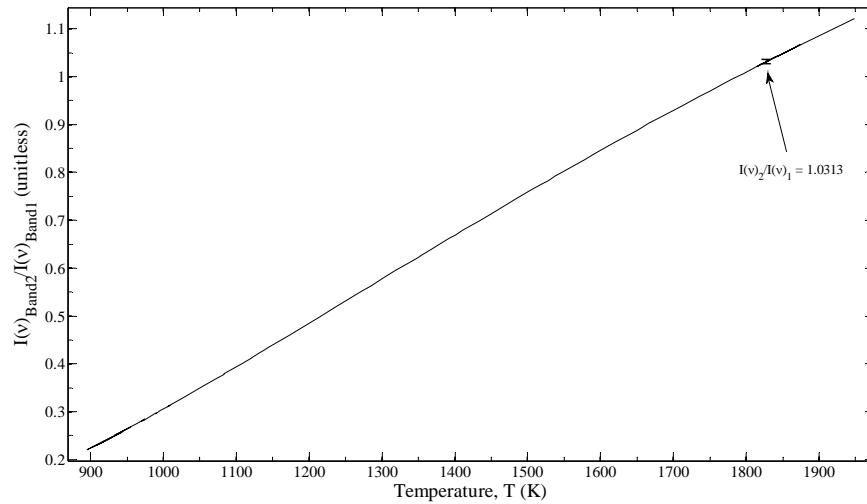


Figure 21. Ratio of band integrated intensities for the regions 2500–2700 and 4500–4700 cm^{-1} as a function of temperature. The intensity ratio for event E9 specifies a temperature of $T = 1828 \text{ K}$. Linearity of the relationship implies the fractional error in temperature is the same as the relative error in the observed intensity ratio, assuming blackbody behavior within the first 1 s after detonation.

3.2. Temperature dynamics

The dynamics of the fireball temperature are dictated by: (1) a sudden initial temperature rise given by the energy released from the detonation into heating, (2) rapid ($t < 5\text{ms}$) expansion of the fireball, (3) radiative cooling, (4) turbulent mixing of the atmosphere with the detonation by products, (5) secondary combustion of detonation by-products with atmospheric oxygen. A thorough analysis of the fluid dynamics, chemical kinetics and radiative process does not lead to the extraction of key features for classification. Instead, we chose a global, empirical model for the fireball temperature:

$$\frac{dT}{dt} = -a (T^4 - T_{atm}^4) + b [\exp(-c t) - \exp(-d t)] \quad (17)$$

The initial temperature, T_o , should be proportional to the heat of detonation, ΔH_d , relative to the total heat capacity for the detonation products, $C_{p,d}$:

$$T(t = 0) = T_o \propto \frac{\Delta H_d}{C_{p,d}} \quad (18)$$

The radiative cooling is described by the Stefan-Boltzmann law where:

$$a = \frac{(\varepsilon A) \sigma_{SB}}{C_{p,c}} \quad (19)$$

and $\sigma_{SB} = 5.67 \times 10^{-8} \text{ W/m}^2 \text{ K}^4$. The ambient temperature is low and may be neglected in the first term on the right hand side of Eq. (17). The high explosive is under-oxidized and the second term in Eq. (17) represents the combustion of detonation products upon mixing with atmospheric oxygen. We employ the heat capacity of the combustion products, $C_{p,c}$ to describe the temperature evolution.

The release of the heat of combustion, ΔH_c , is not rapid and the first exponential term in Eq. (17) accounts for the rate of turbulent mixing. As the detonation products are fully consumed no additional heat is released and the second exponential represents this decay of combustion reagent concentration. The total heat released during secondary combustion is obtained from the time integral of the second term in Eq. (17) and should be proportional to the heat of combustion:

$$\Delta H_c \propto C_{p,c} \int_0^{\infty} b [\exp(-c t) - \exp(-d t)] dt = b C_{p,c} (1/c - 1/d) \quad (20)$$

Further justification for the use of the empirical Eq. (17) is provided in the following discussion of the experimental results.

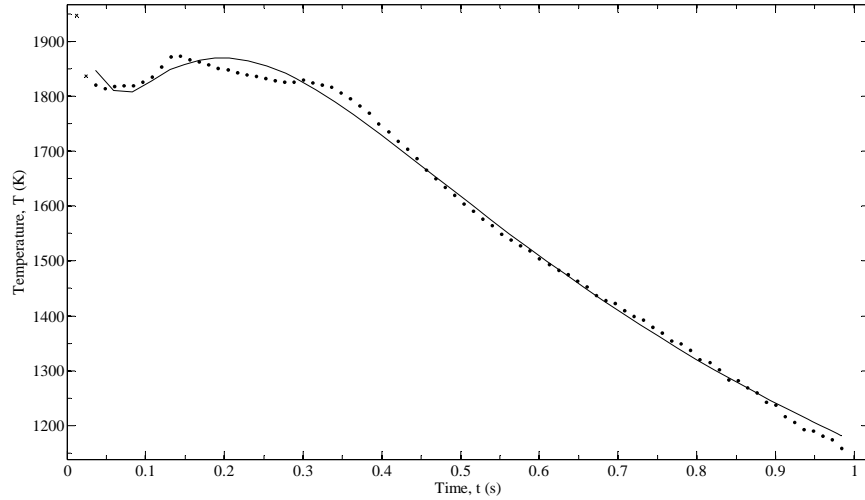


Figure 22. (■) Temperature profile observed for event E9 and (—) fit of the numerical solution to Eq. (17) yielding the fit parameters provided in Table 10.

An example fit of the numerical solution to Eq. (17) for the temperatures extracted for event E9 is illustrated in Figure 22. The resulting fit parameters, T_o , a , b , c , d and their associated uncertainties for each event are reported in Table 10.

The observed initial temperatures, $T_o = 1290\text{--}1848$ K, do not appear to correlate well with the composite HE heat of detonation, as illustrated in Figure 23. This important finding suggests that the empirical model-derived T_o is not a good parameter for event classification. Thus, it seems that it is only the minor details of T_o that may aid in the classification effort. As reported in the previous chapter, we have observed that the efficiency of converting the heat of detonation into the shock front to decrease with increased aluminum and liner content. It is not surprising that the observed initial temperatures are about 30-85% of the HE detonation energy predictions.

Table 10. Fit parameters for numerical solution to Eq. (17)

Event Description	ODE Empirical Model				
	T_o (K)	a ($\times 10^{-10}$ ($\text{s}^{-1} \text{K}^{-3}$))	b ($\times 10^4$ (K s^{-1}))	c (s^{-1})	d (s^{-1})
E8 - SN19	1290.4 ± 34.5	8.01 ± 0.9	2.40 ± 0.7	6.25 ± 0.0003	13.85 ± 3.0
E13 - SN21	1758.1 ± 13.8	5.65 ± 0.6	3.93 ± 0.9	4.74 ± 0.0001	7.55 ± 0.6
E5 - SN20	1723.6 ± 53.2	5.66 ± 0.8	1.52 ± 0.4	5.26 ± 0.0003	18.33 ± 6.1
E16 - SN03	1631.4 ± 22.5	8.53 ± 1.1	8.40 ± 1.0	7.21 ± 0.5826	9.62 ± 0.2
E7 - SN07	1489.5 ± 32.8	7.46 ± 1.1	1.00 ± 0.2	3.24 ± 0.0001	18.64 ± 5.0
E9 - SN11	1848.3 ± 18.3	5.08 ± 0.3	2.04 ± 0.4	4.21 ± 0.4088	10.32 ± 1.6
E4 - SN15	1813.4 ± 36.7	5.08 ± 1.0	2.91 ± 1.3	4.86 ± 0.0002	9.09 ± 1.8
E17 - SN14	1673.7 ± 29.4	5.80 ± 1.2	8.11 ± 6.9	6.08 ± 0.0002	7.80 ± 1.4
E11 - SN01	1685.1 ± 62.4	5.90 ± 1.7	1.28 ± 0.6	3.65 ± 0.0002	13.56 ± 5.5
E1 - SN04	1603.7 ± 40.9	7.47 ± 1.5	2.63 ± 1.2	5.29 ± 0.0013	14.70 ± 11.7
E6 - SN13	1805.1 ± 27.3	4.62 ± 0.8	3.97 ± 1.5	5.05 ± 0.0001	9.03 ± 1.4
E3 - SN08	1648.4 ± 35.6	7.07 ± 1.7	2.75 ± 1.2	4.51 ± 0.0002	9.96 ± 2.1

The magnitude of the radiative cooling parameter, $a = 4.6\text{--}8.5 \times 10^{-10} \text{ s}^{-1} \text{K}^{-3}$, is consistent with the fireball size and heat capacity. For a blackbody ($\varepsilon = 1$) and a typical fireball area of $A \approx 333 \text{ m}^2$, and the combustion product heat capacities of Table 9, Eq. (19) predicts the radiative cooling is described by $a = 4.9\text{--}9.0 \times 10^{-10} \text{ s}^{-1} \text{K}^{-3}$, depending

on the event heat capacity. Thus, it is estimated that time scale for the initial temperature decay is $aT_o^3 = 1.93\text{--}4.77 \text{ s}^{-1}$. Despite being in the same range of values, there is no clear correlation between the model fit parameter-derived a and calculated a values.

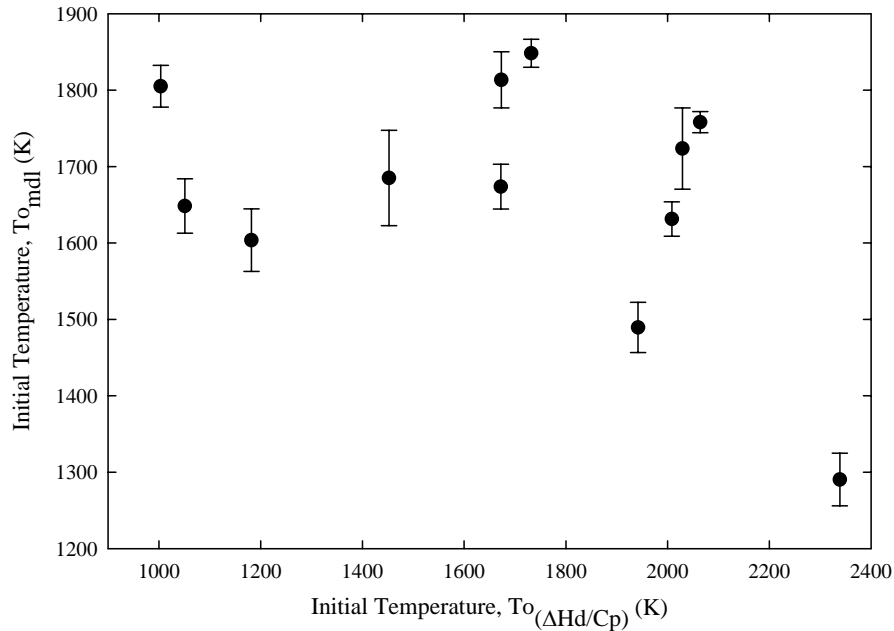


Figure 23. Scatter plot between empirical model predicted initial temperature and initial temperature predicted from thermodynamic properties. Lack of correlation suggests initial temperature is not a good variable for event classification.

A strong correlation, $r = 0.96$, is observed between the secondary combustion fit parameters b , c , d , and the thermodynamic properties, ΔH_c and $C_{p,c}$, as shown in Figure 24. The relationship of Eq. (20) is well supported by the experimental results and offers a potential event classification discriminator. By observing the effect for secondary combustion on the temperature decay profile, information related to the combustion heat release may be discerned. A linear fit to the data of Figure 24 provides a slope of 0.49 ± 0.1 , suggesting only half of the available energy is released in the fireball.

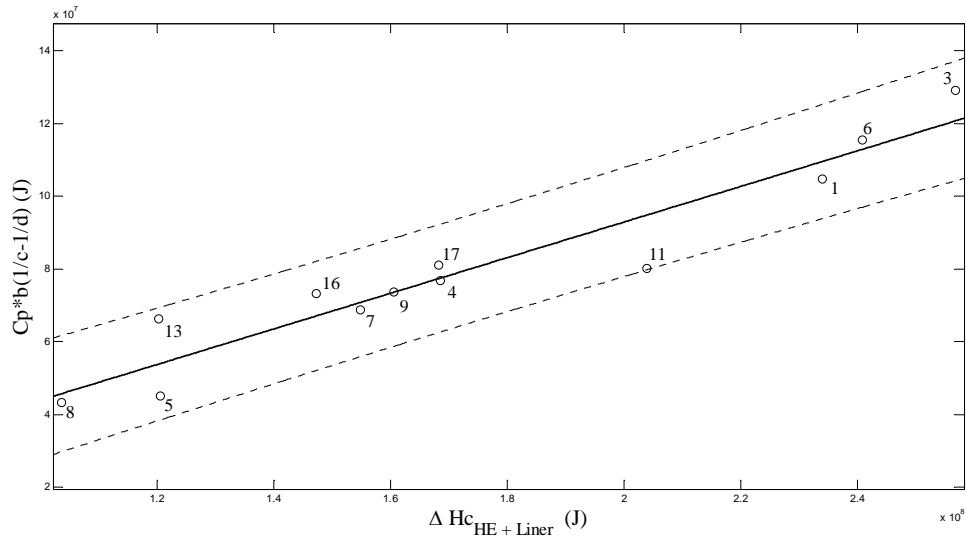


Figure 24. Correlation between predicted and observed heats of combustion with slope of 0.49 ± 0.1 and correlation coefficient of $r = 0.96$.

The liners exhibit a high heat of combustion. Figure 25 demonstrates that the model predicted heat of combustion increases as RDX is substituted for increased liner size and may contribute to the temperature rise.

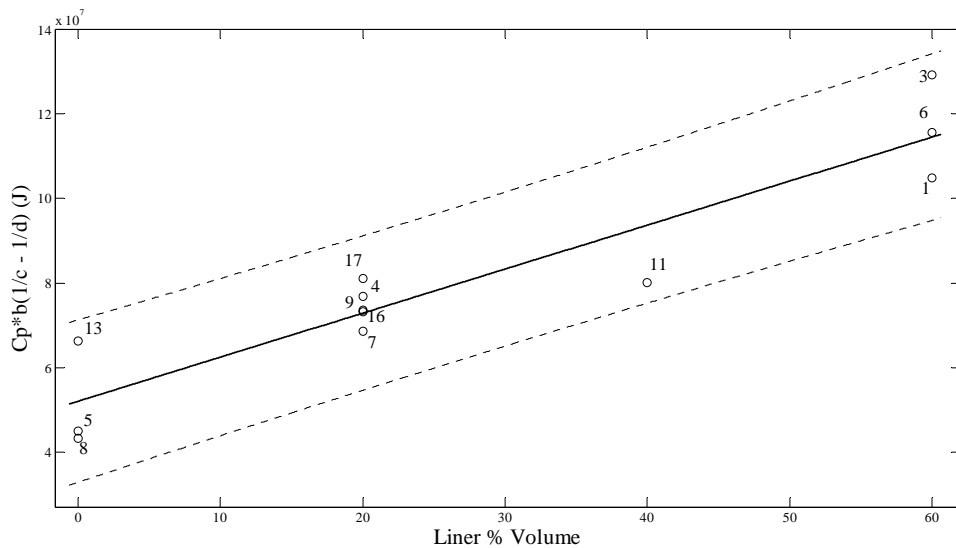


Figure 25. Dependence of observed heat of combustion on fraction of volume allocated to the liner, indicating correlation of $r = 0.93$.

This positive slope and its corresponding correlation, $r = 0.93$, suggests that perhaps the late-time energy release of the aluminum particles, coming mostly from the liner, is being realized. This notion is supported by the finding that the molar specific heat of combustion for the PE-Al liner is 1.3-1.4 times greater than the molar specific heat for RDX.

The efficiency of converting the heat of detonation into driving the explosive expansion of the shock front was recently analyzed in the previous chapter for the present events using the Sedov-Taylor model [54, 60]. The results are best described by a constant rate of energy release and near spherical expansion. The time scale for release of the detonation energy relative to the ideal RDX detonation wave velocity provides a measure of detonation efficiency.

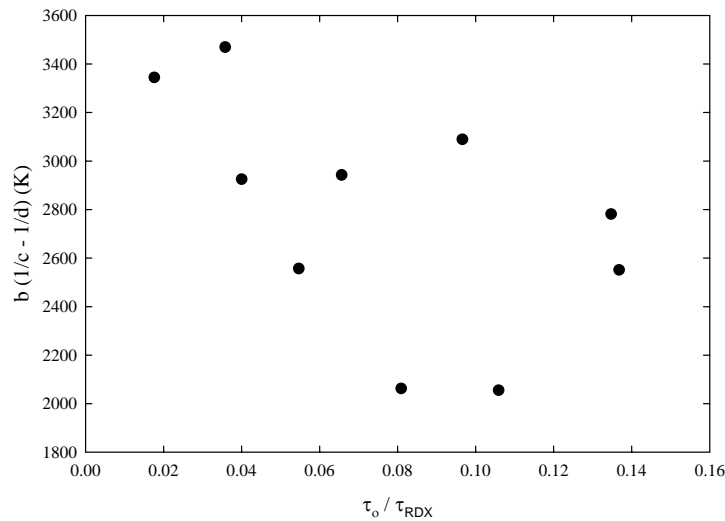


Figure 26. Scatter plot illustrating no significant relationship between combustion fit parameters and efficiency for converting heat detonation into shock expansion.

The observed efficiency ranges from 2–15% when liner or aluminum is substituted for RDX for those events with blast dimensionalities slightly less than spherical geometry.

Efficiencies are less than those typically found in the literature. One might expect the energy not converted to shock expansion to be available for secondary combustion increasing the temperature of the subsequent fireball. However, Figure 26 illustrates no significant relationship between the combustion fit parameters expressed in Eq. (20), $b(1/c-1/d)$, with shock efficiency. Apparently, the heat of detonation not converted to shock is not available for secondary combustion.

3.3 Fireball Rise

A study by Kansa concludes that the fireball rise depends upon the mass and initial temperature of the explosion as well as atmospheric and explosion-generated turbulence and the fireball's Richardson number [37]. Spatially integrating the fireball's mass, momenta, and total energy differential equations, he models the rise of 6.4-1019 kg TNT explosion fireballs from initiation to hundreds of meters in height. The main thrust of his efforts is the long duration rise profile of an explosion "puff," or what is referred to as the post-detonation particulate cloud (PDPC) in the present work. His analytical expression for buoyant velocity assumes the PDPC mass, density difference, dimensions, lateral and rise speeds, and turbulence parameters as slowly varying quantities. Unfortunately, these assumptions are not applicable at the very early times of an explosion, of which the present research is mostly concerned. He explains the eventual elliptical shape of the PDPC as arising from the hot gas imparting a vertical component of momentum to the existing radial momentum and thus distorting the initially spherical shape into a mushroom shaped cloud. During his model development, Kansa also expresses the vertical speed of the top boundary of the rising PDPC as [37]:

$$s_z^\pm = -(h^\pm / r)(dr/dt) \quad (21)$$

where

h^\pm = height of PDPC top (+) and bottom (–)

r = radius of the rising PDPC at the center

dr/dt = rate of change of radius

As reported in Chapter IV, we have recently characterized the rate of PDPC lofting from high speed visible imagery. A summary of these rates for each of the current events is included in Table 11. Using h , r , Δr , and Δt extracted from high speed imagery analysis, data and lofting rates for several events are compared with Eq. (21). The resulting vertical speeds (s_z^+) at the PDPC top have variances too large to provide meaningful insights into the PDPC rise phenomenon using this simplified relation for the test articles in the present work.

Table 11. Comparison of fit parameters to thermodynamic predictions.

Event Description	Detonation	Combustion			PDPC
	$\Delta H_{d,HE} / C_{p,d}$ (K)	$(A \sigma_{SB}) / C_{p,c}$ ($\times 10^{-10} (s^{-1} K^{-3})$)	$\Delta H_c / C_{p,c}$ (K)	$b (1/c - 1/d)$ (K)	Rise slope (m/s)
E8 - SN19	4363.87	8.96	4924.78	2054.77	8.29 ± 0.54
E13 - SN21	4284.43	8.78	5594.49	3089.38	11.58 ± 1.14
E5 - SN20	4320.79	8.63	5510.63	2062.52	7.18 ± 0.78
E16 - SN03	3748.88	7.54	5881.30	2924.79	10.40 ± 0.51
E7 - SN07	3624.51	7.01	5749.57	2551.03	9.27 ± 0.38
E9 - SN11	3684.64	7.36	6258.36	2871.18	8.16 ± 1.04
E4 - SN15	3561.06	6.83	6101.00	2781.39	11.01 ± 0.49
E17 - SN14	3558.57	6.85	6102.46	2942.47	9.66 ± 0.75
E11 - SN01	2880.83	6.02	6505.47	2556.62	11.03 ± 0.79
E1 - SN04	2207.68	5.73	7096.70	3179.21	none
E6 - SN13	2136.14	5.67	7229.97	3469.56	10.81 ± 1.30
E3 - SN08	1963.90	4.89	6644.54	3344.32	10.78 ± 0.97

As an alternative approach, we examine Kansa's assertion on the temperature dependence of the PDPC rise. The observed lofting rates are correlated with the present results for fireball initial temperature, T_o , and the combustion fit parameters representation of temperature, $b(1/c - 1/d)$, in Figure 27. The combustion fit parameters and the fireball rise have a significant correlation coefficient of $r = 0.75$. When T_o is correlated to PDPC rise, two outlier events (E5 and E9) are readily identified. If the two outlier events are excluded, the T_o and fireball rise are well correlated to within 94% and are consistent with Kansa's assertion. With the outliers included, the correlation is not significant at $r = 0.33$. Turbulence and atmospheric stability influence the rise height. However, the data set is too sparse and the variance in recorded wind speeds at the test site too great for a definitive investigation.

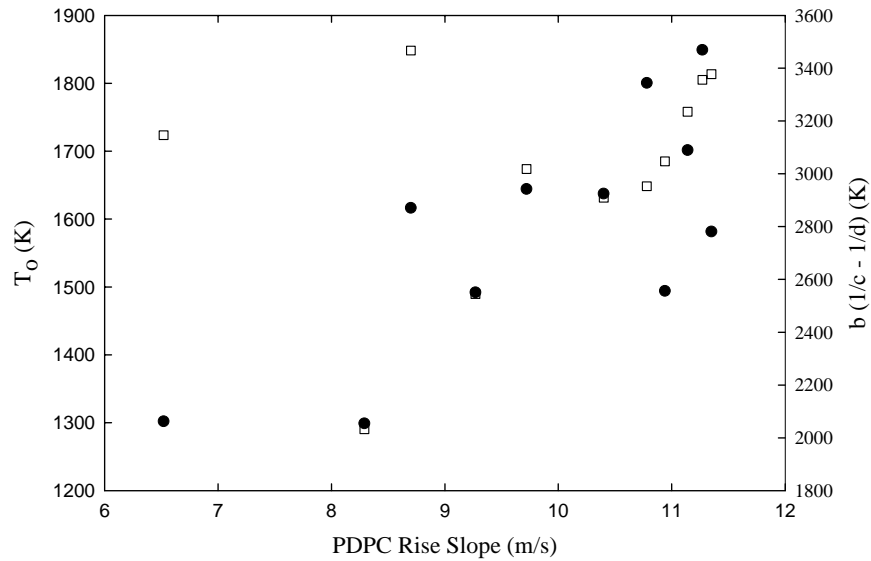


Figure 27. Relationship between lofting rate and (□) T_o and (●) combustion fit parameters.

Weil et al. [62, 63] and Bjorklund et al. [6] have also examined plume rise during their development of open burn and open detonation dispersion models for environmental impact studies. Although also primarily aimed at long duration plume and cloud rise occurring over hundreds of meters, their model attempts to address earlier time plume rise. Weil et al. express the initial cloud rise, Δh , as related to its initial momentum (M_τ) and buoyancy (F_τ) using the expression [62]:

$$\Delta h = 2.35(M_\tau t + F_\tau t^2)^{1/4} \quad (22)$$

where

$$M_\tau = \frac{4\pi}{3} * r_o^3 w_o \quad \text{and} \quad F_\tau = \frac{g Q_\tau}{c_p \rho_a \Theta_a}$$

They define w_o , r_o , and Q_τ as the initial velocity, radius, and heat content of the cloud. Also, g , c_p , ρ_a , Θ_a are the gravitational acceleration, specific heat of the air, ambient air density, and potential temperature. To compare the above model to the data in the present work, extracted radius and observed PDPC loft rate as well as heat of combustion and a fireball temperature of 1300 K for data PDPC loft heights above 10 m were inputted into Eq. (22). For several events tested, there was a 10–30% difference between the data and the model predicted cloud rise height, Δh , within the first 0.5 s after detonation. Eq. (22) appears more sensitive to PDPC radius and velocity and less so to heat content or PDPC temperature. Given the physical complexity of a rising fireball and the contributory effects of turbulence, atmospheric conditions, and the extensive variability in the data, finding a precise model to describe the lofting rate proved difficult. Nevertheless, a 75% correlation between empirical model fit parameter-derived temperature and PDPC rise suggests a possible relationship between buoyant fireball rise and temperature.

4. Conclusions

Mid-infrared spectra of the fireball resulting from the detonation of aluminized RDX explosives exhibit spectral features associated with CO_2 , CO , H_2O and soot emission. Two spectral bands, $2500\text{--}2700\text{ cm}^{-1}$ and $4500\text{--}4700\text{ cm}^{-1}$, have been identified with near unit emissivity to extract the evolving fireball temperature. The temperatures agree well with a simple radiative transfer model and decay from initial values of $\sim 1300\text{--}1850\text{ K}$ to about 1000 K over a one second interval. The temperature profiles are adequately described by: (1) radiative cooling and (2) secondary heat release due to combustion of the under-oxidized fuel during turbulent mixing with the atmosphere. Secondary maxima are observed in the evolution of the fireball temperatures and the temperatures in excess of the radiative cooling predictions are related to the available heat of combustion. Indeed a strong correlation exists between empirical model's estimate of the heat of combustion and the thermodynamic properties of the high explosive (RDX and aluminum) and liner. Test articles with higher aluminum and liner content exhibit higher fireball temperatures over an extended interval. Approximately 50% of the available energy is observed in fireball temperature. Furthermore, the empirical heat released increases linearly with the fraction of the volume allocated to the liner.

The increased understanding of remote optical signatures from detonation fireballs suggests possible information for classification of event type. The initial fireball temperature exhibits no significant correlation with the heat of detonation, confirming prior suspicions that the efficiency of high explosive detonation is highly variable. However, the relative temporal dynamics of the temperature profiles do appear useful for

classification. If an estimate for the heat of detonation could be determined, possibly from the shock dynamics, then the empirical value for the heat of combustion might specify the relative partitioning between high explosive content and aluminum or liner fraction. The present data samples a small selection of high explosive compositions with minimal repeatability in event type. Considerable further investigation is required to develop a complete set of key features for classification and to evaluate the probability distribution functions for various event classes.

VI. High-Speed Spectral Measurements of IED Detonation Fireballs

Overview

Several homemade explosives (HMEs) were manufactured and detonated at a desert test facility. Visible and infrared signatures were collected using two Fourier transform spectrometers, two thermal imaging cameras, a radiometer, and a commercial digital video camera. Spectral emissions from the post-detonation combustion fireball were dominated by continuum radiation. The events were short-lived, decaying in total intensity by an order of magnitude within approximately 300 ms after detonation. The HME detonation produced a dust cloud in the immediate area that surrounded and attenuated the emitted radiation from the fireball. Visible imagery revealed a dark particulate (soot) cloud within the larger surrounding dust cloud. The ejected dust clouds attenuated much of the radiation from the post-detonation combustion fireballs, thereby reducing the signal-to-noise ratio. The poor SNR at later times made it difficult to detect selective radiation from by-product gases on the time scale (~ 500 ms) in which they have been observed in other HME detonations.

1. Introduction

Improvised explosive devices (IEDs) in Iraq and Afghanistan have claimed the lives of many American and coalition forces. At the heart of many of these IEDs are powerful (HMEs) that can be manufactured using readily available commercial off-the-shelf chemicals such as ammonium nitrate (common fertilizer) and organic materials such as fuel-oil. When mixed with each other or with other simple additives, they can produce high explosives (HEs) able to deliver devastating blast effects. The current research presented in this chapter is part of a larger effort to develop optical techniques

capable of deriving forensic information from the emitted radiation that accompanies the detonation of a high explosive. Optical forensics could complement standard forensics techniques and might enable collection of key information when standard forensic techniques are impractical. Our research group has previously developed a physics-based phenomenological model able to interpret the collected spectra in terms of temperature, area, and several molecular species concentration profiles. Current research efforts are aimed at improving the understanding of the fluid dynamical and chemical kinetic phenomena so that the information contained in the temporal evolution of the measured spectra can be properly extracted. With this understanding, a more robust identification and classification of HME signatures may be possible. This chapter shall limit itself to the detonation and post-detonation combustion (PDC) signatures of these HMEs.

The HMEs manufactured for the current research effort were primarily ammonium nitrate based explosives. Originally used as a high-nitrogen fertilizer for agriculture, ammonium nitrate (NH_4NO_3) is easily exploited as an oxidizer in an explosion reaction. Ammonium nitrate and various organic materials were manufactured into explosive devices at a desert test site allowing the research teams to study the effects of the various constituents on the signatures from these HMEs.

The detonation of a conventional explosive unleashes a powerful shock wave which is used to inflict damage to the intended target. Intense visible and infrared radiations are also observed and are the result of thermal emission from the detonation by-products. As most explosives are under-oxidized, the detonation by-products can fuel additional combustion. This post-detonation combustion fireball is much longer lived, as it is sustained by the availability of atmospheric oxygen brought into the fireball by

processes such as turbulent mixing. For the purpose of optical forensics, the midwave infrared region of the spectrum is an area of interest because many combustion by-products (e.g., CO, CO₂, H₂O, etc.) emit at these energies. With this in mind, our battlefield optical forensic efforts are focused on collecting MWIR spectra primarily using InSb semi-conductor detectors that exhibit the best sensitivity at these photon energies. By interrogating the spectra temporally, it is hoped that certain spectral features become more apparent and discernible so that inherent chemical kinetic processes can be further understood and lead to improved classification of these events.

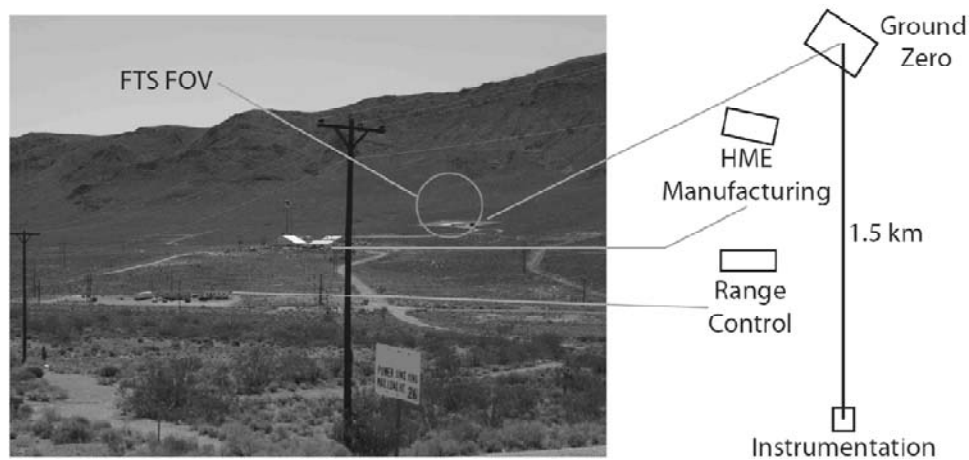


Figure 28. Unobstructed line-of-sight view of the test range from the instrumentation, matched to an overhead schematic of the site.

Spectral features of the detonation fireballs have previously been examined [26, 28, 32, 47]. Those studies focused on features of the spectra at specific wavenumbers that could allow differentiation between TNT-based and RDX-based HEs, static and air-dropped munitions, and cased and un-cased explosives. High-speed imagery has also been used to begin understanding the temporal and spatial evolution of the detonation

fireball [59]. Differentiation between detonations of similar HE types with similar chemistries (i.e., RDX-based) becomes challenging. We think that through the study of the kinetic behavior of PDC molecular species, a more robust method of event classification can be found. The ultimate aim of the present ongoing research effort is to develop an empirical kinetics-based model to characterize and predict the observed time-evolution of the selective emitter concentrations, particulate concentrations, temperature profiles, and fireball radius profiles and then subsequently augment or incorporate it into the current physics-based model developed by AFIT's Remote Sensing Group.

2. Experimental

Tests were conducted to study the signatures from the detonation of HMEs. The tests were conducted in the summer of 2009 at a desert test site. The Air Force Institute of Technology (AFIT) participated in the signature collection efforts. Seven different HME types were produced and were subsequently disposed of via eleven separate detonation events. Four of these detonations (Events 4a-4d), each containing 10 kg of a specific HME, were initiated specifically to exploit repeatability during the signatures analysis phase. Table 12 provides a brief overview of the HME types and AFIT's deployed instrumentation suite used to collect the signatures.

The desert test site presented a challenging location for the deployment of AFIT's scientific laboratory-grade instruments. Ambient temperatures regularly reached 39°C (102°F) during the daytime and occasionally peaked at 43°C (109°F). The instruments were encapsulated in an air-conditioned environmental shelter maintained at a nominal 21°C (70°F). Detonation signatures of homemade explosives were collected using two

interferometers, a radiometer, two thermal imagers, and a digital video camera.

Detonation fireball radiation was attenuated by the ensuing dust cloud that enveloped the explosion and post-detonation combustion. Consequently, high-fidelity identification of radiation from selective emitters using the FTS data set proved difficult. The relative intensities of the detonation events had short dwell times in the collected FTS spectra. Upon detonation, the initial relative intensities appeared robust but quickly degraded to weak and diffused signals. The radiometer's 100 kHz sampling rate was able to observe phenomena in the earliest part of the HME explosions. The FTS and FLIR data sets for the present research may prove to be of greater utility upon continued in-depth examination. The key to understanding the kinetic behavior and classification of the HMEs tested may lie in further analysis of the temporally-rich radiometer data set that was acquired at 100 kHz. Figure 0 shows the view of the detonation test from the point-of-view of the instruments. The instruments were placed at a standoff distance of about 1.5km from ground-zero with a direct unobstructed line-of-sight at an elevation angle of approximately $-5 \leq \theta \leq 0$ from the horizontal.

Table 12. Summary of manufactured HMEs and AFIT's data acquisition instruments. The peak temperature and time-to-peak columns were based on an analysis of calibrated, high-speed radiometric measurements made by the CI Systems radiometer. [56, 57]

EXPLOSIVE				INSTRUMENTATION			
Event #	Weight (lbs)	Peak Temp [K]	Time-to-Peak [sec]	Instrument	Manufacturer	Resolution	Fore-Optics
1	98	3000	0.04	FTS (MCT/InSb)	ABB-Bomem	82 Hz at 16 cm ⁻¹	75 mrad
2	80	3260	0.25	FTS (Si/InGaAs)	ABB-Bomem	82 Hz at 16 cm ⁻¹	75 mrad
3	53	—	—	IR FPA (InSb)	FLIR	320x256 @ 430 Hz	200 mm
4a	22	—	—	IR FPA (InGaAs)	FLIR	320x256 @ 430 Hz	180 mm
4b	22	—	—	4-channel radiometer	CI Systems	100 kHz	40 mrad
4c	22	—	—	Witness video camera	Canon	60 Hz (interlaced)	—
4d	22	—	—	Weather Station	Weather Hawk	T, P, rel hum @ 1 Hz	—
5	50	2875	0.09				
6	93	3100	0.05				
7	66	—	—				
8	98	2850	0.1				

The key temporal and spectral resolutions of the various instruments during signature collection are summarized in Table 12b above. LWIR and MWIR interferograms were collected using an ABB-Bomem MR-304LN FTS using HgCdTe (MCT) ($667\text{--}2500\text{cm}^{-1}$) and InSb ($1,800\text{--}10,000\text{ cm}^{-1}$) detectors, with the InSb channel fitted with an optical density (OD) filter. Visible and NIR interferograms were collected using an ABB-Bomem MR-304SC FTS using Si ($10,000\text{--}14,000\text{cm}^{-1}$) and InGaAs ($6,000\text{--}10,000\text{cm}^{-1}$) detectors, respectively. Both interferometers were fitted with a 76 mrad telescope providing a 116 m diameter field-of-view (FOV) at ground-zero. All detonation events significantly under-filled the FTS FOV. In retrospect, the 28 mrad telescope providing a 43 m diameter FOV would have been a better choice. A CI Systems ColoRad four-channel radiometer acquired integrated intensity data using Si, InGaAs, InSb, and MCT detectors, each fitted with a narrow optical density filter. MWIR thermal imagery was collected using a FLIR Systems ThermoVision SC6000 FPA camera using an InSb detector outfitted with a band-pass filter and 0.7 OD filter. The InSb FLIR operated in super-framing mode using 0.01ms, 0.1ms, and 1ms integration times. Subsequent images were captured at different integration times. NIR thermal imagery was acquired via a FLIR ThermoVision SC6000 InGaAs FPA camera. All InGaAs FLIR data were saturated. No filters were used. The Canon XL-1 3CCD digital video camera was used as a witness camera. Additionally, a WeatherHawk weather station provided wireless meteorological information at the instrument site. A second WeatherHawk was intended to be placed near the detonation site at ground-zero, but was disapproved because its wireless signal had the potential to interfere with the explosives initiation.

Additionally, several signatures were not acquired by the radiometer or the FLIR cameras due to mis-communicated detonation times/locations.

The MCT/InSb FTS was calibrated using an Electro Optical Industries low-temperature small-area blackbody (BB) source. The small-area BB source was placed within 4 cm of the FTS entrance aperture and over-filled the FOV. Low-temperature BB measurements were taken at 100, 80, 60, and 40°C the day before the detonation tests. The low temperature measurements allow the detector to be calibrated to apparent radiance between 1800 cm^{-1} and 3000 cm^{-1} . At higher wavenumbers, the source radiance at these temperatures is not sufficient for adequate calibration. Calibration measurements at the same four temperatures were taken prior to both Event 1 and Event 2 the day of the detonation tests. However, lack of adequate time between successive shots precluded low-temperature BB measurements after the remaining events. Unfortunately, there was not adequate power to run the high-temperature cavity BB. As a result, laboratory measurements of a high-temperature cavity blackbody were used to extend the FTS detector response beyond 3000 cm^{-1} . The use of a low-temperature BB and high-temperature cavity BB to calibrate the FTS is described in more detail in a previous paper. [26] In this paper, only the raw, un-calibrated spectra are presented.

3. Results and Discussion

FTS, FLIR, and witness camera signatures

The energetic nature of detonation events are such that they are amenable to optical observation by commercial-off-the-shelf sensors and their spectra exploited for optical forensic analysis. In the present research, signal obscuration due to ejected ground

dirt and dust from the detonations resulted in low signal-to-noise emissive signatures. Figure 29 from a witness camera illustrates this. In the upper left panel, a detonation fireball forms as the detonation transitions to an explosion. Continuum emission from particulate material typically dominates this early stage and its broadband, Planckian-like nature is evident in the collected FTS spectra, as will be discussed shortly. Note also the circular whitening on the ground as the shock wave propagates hemispherically outward from the center and perturbs the soil and dust. The top middle panel shows the continuing transition to the combustion phase. At this stage, residual fuels often remain due to incomplete oxidation, typically because the high explosive is under-oxidized. Turbulent mixing entrains atmospheric oxygen into the plume, and under the right conditions, continued combustion can occur. In previous detonation fireball measurements, the continuum radiation from particulate material began to subside, revealing selective emission from the gaseous combustion by-products. [28, 32]

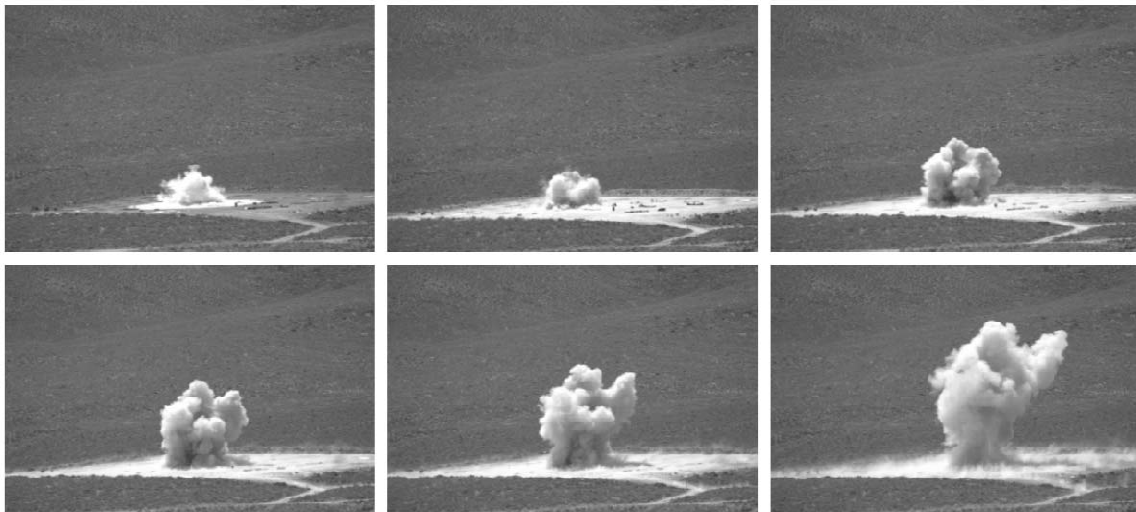


Figure 29. Sequence at ground-zero showing signal obscuration immediately after detonation. Optical attenuation from dust resulted in relatively weak infrared signatures reaching the FTS at the standoff distance of 1.5 km.

During the present test, signal attenuation from the dust cloud becomes problematic at about this point. The witness camera reveals a darker gray sooty plume in the middle of the explosion surrounded by what appears to be reddish-gray dust (possibly lime stone and other minerals) being ejected into the surrounding air by the detonation. The characteristic spectral signatures from lime stone and other minerals were not analyzed in the present research but may be of worth for future work. In the upper right-most panel, note that the shock wave has fully traversed across the bare soil test area as evidenced by the whitened ground throughout the image as compared to the first panel. As the explosion and combustion progresses in the succeeding panels in Figure 29, it is increasingly difficult to differentiate between the combustion plume and the dust cloud being kicked-up into the air. This presented measurement challenges to the deployed instruments.

The attenuation effect resulted in spectral measurements by the FTS with a low signal-to-noise. Figure 30 shows the spectrum from the 10 kg HME detonation of Event 4a. The left panel shows the fireball LWIR (HgCdTe) and MWIR (InSb) spectra measured by the FTS immediately after the detonation. The relative intensity is uncalibrated, but a background subtraction has been performed to extract the characteristic spectra from the detonation event. The broadband intensity distribution indicates continuum emission, likely from hot particulate material (soot) within the fireball. Since dust is not a constituent of the exploding HME but only an external particulate disturbed by the transient shock wave, it is not expected to contribute in any significant way to the fireball. (We assume it has not been heated significantly by the detonation.).

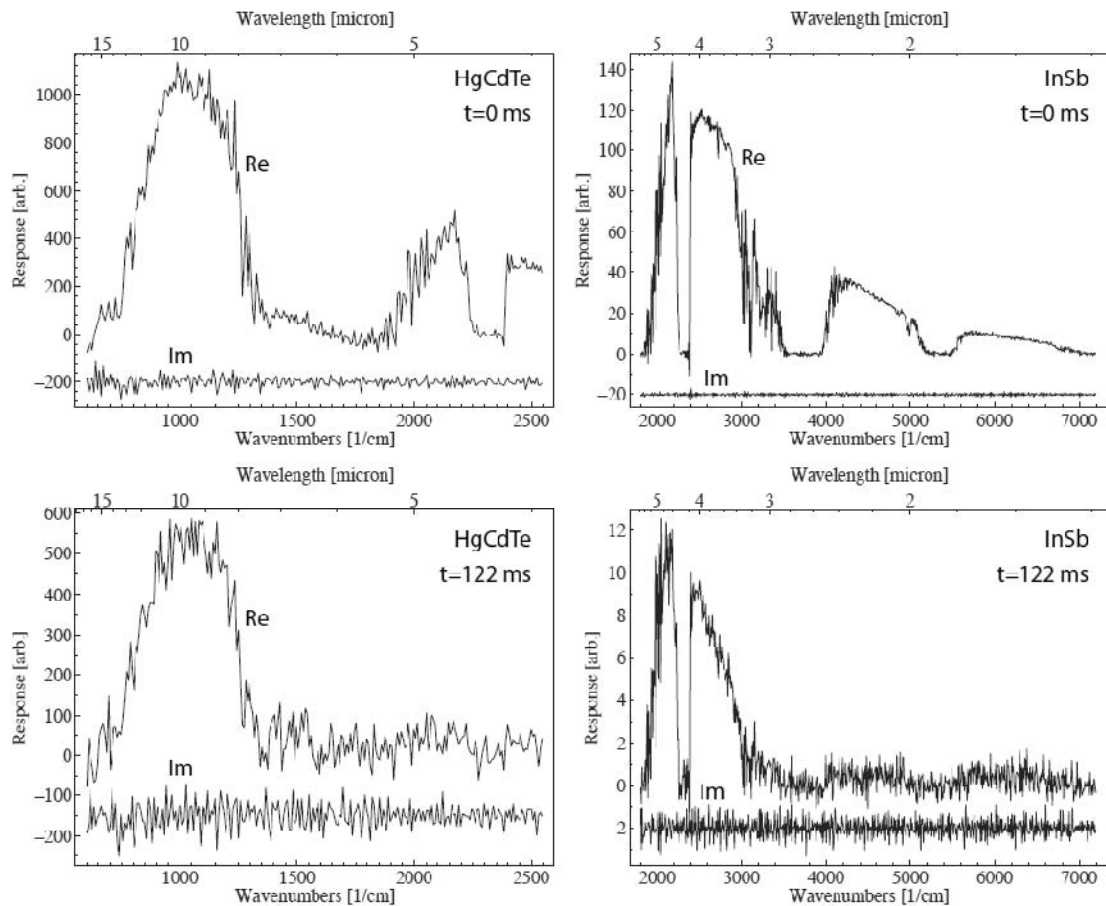


Figure 30. Raw spectra from the two infrared FTS channels for Event 4a. (The spectral response of the individual detectors have not been removed from the data.) The real and imaginary components are denoted Re and Im, respectively. *Top panel:* LWIR (left) and MWIR (right) spectra immediately after detonation. *Bottom panel:* LWIR (left) and MWIR (right) spectra 122ms after detonation.

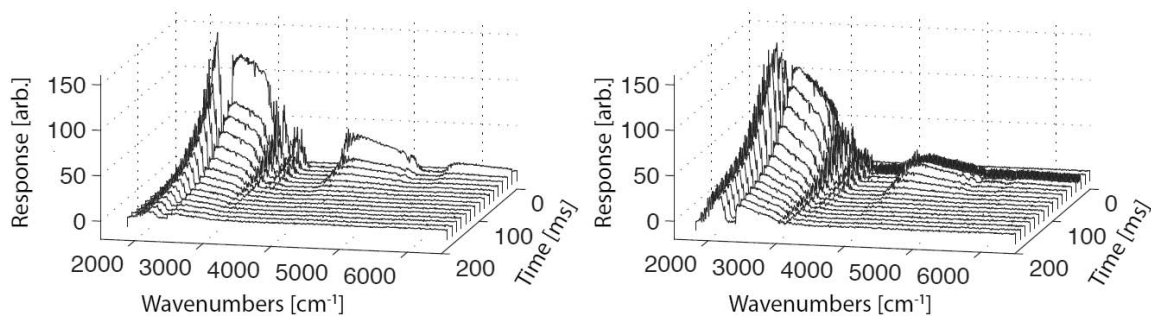


Figure 31. Waterfall plots of the un-calibrated MWIR (InSb) spectra for Event 4a (left panel) and Event 5 (right panel). Again, note the rapid decrease in relative intensity of the Event 4a HME. While the spectra are un-calibrated, both events were collected under identical instrument conditions, permitting relative intensity comparisons.

Note also the negative radiance present in the top MWIR (InSb) spectrum at the edge of the $4.3\text{ }\mu\text{m}$ CO_2 atmospheric absorption band (near 2400 cm^{-1}). As no apodization function was applied to the spectra presented in Figure 30, the instrument line shape is a sinc function. Thus, small negative intensities can occur that are not associated with instrument noise. The bottom panel in Figure 30 shows the same event approximately 122 ms later. Here the spectrum is much noisier and the MWIR intensity has experienced a ten-fold decrease in magnitude. In addition to a reduced signal due to a cooling plume, the attenuation from the surrounding dust cloud results in the low SNR of the measured radiant emissions from the explosion and combustion processes. Unfortunately, the temporal evolution of the selective emitters previously used for event classification were not discernible, even at later time steps where the selective emitters typically become more pronounced after the particulate matter emissions subside due to oxidation and/or settling.

The imaginary components of the spectra—denoted Im —are also provided in Figure 30. Ideally, the imaginary component represents a snapshot of the instrument noise. Since a Fourier-transform spectrometer is observing a rapidly varying source, the introduction of spectral artifacts due to systematic variations in the source intensity is possible. This problem was discussed in general by Kick et al. [39] and it was found that under many measurement conditions the imaginary part of the spectrum is much more sensitive to scene-change artifacts (SCAs) than is the real part. Examination of the imaginary spectra in Figure 30 suggests SCAs are not significant given their lack of systematic structure. In a companion paper, the issue of SCAs is carefully considered for detonation

fireballs dominated by Planckian radiation. [33] Surprisingly, it was found that minimal artifacts were introduced into the real part of the spectrum when an FTS looked at a Planckian source that cooled from 2130 K to 1530 K during the acquisition of a single interferogram.

Comparison of the FTS spectra presented in Figure 31 reveals some interesting points. The weight of the HME associated with the spectrum shown in the left panel of Figure 31 is roughly twice the explosive weight of the HME associated with the spectrum shown in the right panel of Figure 31. Note however that the peak relative intensities are roughly the same. This may suggest that the HME for Event 4a has a larger energy flux per unit area per unit HME mass than the HME for Event 5. Calculation of heats of detonation from reaction stoichiometry should help provide an answer. Also, the signal duration of the larger Event 5 HME is slightly longer than the smaller Event 4a mixture. This is consistent with expectations as previous work on classification of explosives has shown that explosions from larger conventional HEs typically last longer than smaller ones. A specific reason as to why the 22.7 kg Event 5 was not more intense in the midwave infrared than the 10 kg of Event 4a cannot be readily explained at this time. (Experience has taught us that absolute intensity is not a particularly reproducible signature. Relative spectral intensities are much more reproducible.) Again, an answer may lie in the detonation stoichiometry and enthalpies of the respective HMEs. Additionally, although the ejection of a large volume of dust should not influence the very early stages of the explosion, it has yet to be determined what its overall affect is on the characteristic signature of the event at later times.

Despite signal obscuration by the ejected dust clouds, the various instruments were able to collect signatures that can be analyzed in greater detail as the research progresses. Figure 32 gives a quick look at the signatures collected by the four primary instruments in the present research. The four primary instruments are: digital video camera, thermal imaging camera, FTS, and a radiometer. The top left panel shows the detonation of 10 kg of a specific HME in the visible range of the spectrum as recorded by a witness camera. Note the dark gray particulate cloud nestled in the middle of the reddish-gray dust cloud. The top right panel shows the same event at roughly the same time period but in the MWIR region of the spectrum using the InSb FLIR focal plane array. The InSb FLIR camera gives a 2-D image of the MWIR intensity distribution in the PDC fireball, not the temperature distribution. As stand-alone instruments, the FTS and thermal imagers can provide high-fidelity data sets. However, when thermal imagery is coupled with interferograms collected by the FTS, the instrument combination could function as a crude ad-hoc imaging FTS and can offer a more robust look at the temporal evolution of a detonation event.

The bottom left panel of Figure 32 is an overlap plot of the total FTS spectra from the explosion of the same 10 kg of HME. The FTS operating at 16cm^{-1} spectral resolution is sufficient to resolve the presence of selective emitters, but the short duration and noisy decay of the infrared signature makes classification using selective emitters a challenge. The bottom right panel represents the temporal evolution of the radiometer response of the same event acquired at 100 kHz. The semi-log plot provides greater temporal insight into the irradiance spike seen immediately upon detonation. As seen from the semi-log perspective, the initial irradiance spike appears to be a smooth, albeit

swift, evolution. The resultant collected data set from the four primary instruments is a multi-spectral array of signatures able to span across a broad range of the visible and infrared spectrum.

Analysis of the radiometer signatures reveals further insight into the phenomenology of the disparate HMEs. The intensity profiles show an initial rise in peak intensity and subsequent rapid decay for nine detonation signatures collected by the radiometer. These observed short-lived integrated intensities corroborate the FTS measurements of rapid infrared signal degradation within the first 200–300 ms after

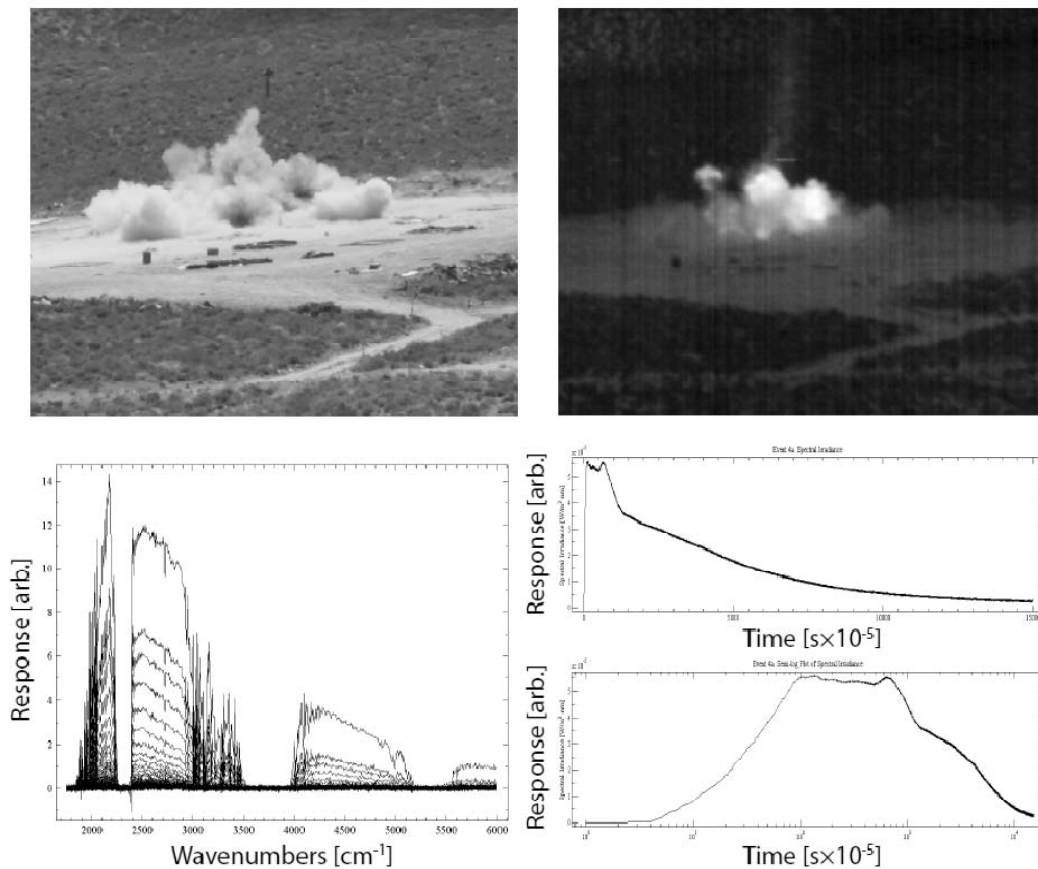


Figure 32. Comparison of measured signatures for the same detonation event (Event4a –10 lbs of a specific HME). Top-left panel: visible image from witness camera. Top-right panel: MWIR FLIR thermal image. Bottom-left panel: Time sequence of MWIR FTS spectra. Bottom-right panel: comparison of integrated intensity and its semi-log equivalent from InSb channel of radiometer.

detonation. A more complete discussion of the phenomenology of the initial detonation inferred from the high-speed radiometer is presented in a companion paper [57]. In that study, it is demonstrated that the initial detonation fireball is well described by a single-temperature Planckian radiator. The supersonic fireball expansion is estimated using the Planckian intensity and compared to simple shock and drag models.

4. Conclusions

Detonation signatures of homemade explosives were collected using two interferometers, a radiometer, two thermal imagers, and a digital video camera. Detonation fireball radiation was attenuated by the ensuing dust cloud that enveloped the explosion and post-detonation combustion. Consequently, high-fidelity identification of radiation from selective emitters using the FTS data set proved difficult. The relative intensities of the detonation events had short dwell times in the collected FTS spectra. Upon detonation, the initial relative intensities appeared robust but quickly degraded to weak and diffused signals. The 100 kHz sample rate of the radiometer enabled the observation of detonation phenomena in the earliest part of the HME explosions. The FTS and FLIR data sets for the present research may prove to be of greater utility upon a more in-depth examination. The key to understanding the kinetic behavior and classification of the HMEs tested may lie in further analysis of the temporally-rich radiometer data set.

VII. Conclusion

1. Summary of Key Findings

Temporally rich visible and infrared signatures from the detonation of RDX-based novel munitions have been analyzed. The shock wave is fit to the Sedov-Taylor point blast model and the fireball propagation is fit to a drag model. Additionally, a new five-parameter, physics-based empirical model is developed to characterize the temperature profiles of post-detonation combustion fireballs.

Analysis of high speed visible imagery reveals the fireball approaches an average peak radius of about 5 m after 50 ms upon detonation. Later imagery shows this fireball to maintain a fairly constant size after 150–200 ms. Spectral analysis reveals emissive areas in the mid-wave region peaking between 160–240 ms while temperature data reveals peak secondary combustion temperatures occurring at roughly 180–250 ms.

As the fireball rises, it begins to exhibit a fairly constant rate of ascent at about 250 ms. The constant rate of ascent of this post-detonation particulate cloud may be attributed to a fireball that has consumed available fuels and is no longer accelerated by a rising temperature resulting from an infusion of large amounts of heats of combustion.

The initial velocity of the blast wave in this work ranges from 1.6–2.8 km/s. The blast wave is best interpreted assuming a constant release of energy ($s = 1$) commensurate with a shock front propagating with a nearly spherical ($n \cong 3$) geometry. This constraint results in blast wave energies of 0.5–8.9 MJ corresponding to energy conversion efficiencies between 2–15% of RDX heat of detonation. The resultant blast model derived energies are dependent not only upon the blast dimensionality but also upon a characteristic length and time defined, respectively, as the radial distance to the start of

the mid-field region and the time required for an ideal RDX detonation wave to traverse this same length. No clear relationship is found between the total amount of aluminum in the test article and the blast wave energy.

A new global empirical model is developed to characterize the temperature evolution of the post-detonation combustion fireball. The empirical model is an ordinary differential equation based on a radiative cooling term and a double exponential source term. Fitted numerical solutions to the empirical model successfully describe the spectrometer-observed temperature profiles. There is a 96% correlation between model predicted heat of combustion and calculated theoretical heat of combustion. There is a 93% correlation between liner volume percent and the model predicted heat of combustion implying a statistically significant role that liner volume plays in secondary combustion in the present work. A statistically significant correlation of 77% between the rate of fireball rise and model predicted temperature hints at the driving influence of temperature on fireball buoyancy.

The empirical model derived radiative cooling parameter, a , is in the same range of values as the theoretically expected values. However, no clear correlation exists between the model predicted a fit parameter and the calculated a parameter. Lack of correlation between model predicted initial temperatures, T_o , and calculated initial temperatures from thermodynamic properties suggests initial temperature is not a good quantity for event classification. The strong correlation ($r = 0.96$) between model predicted and theoretically calculated heat of combustion offers a new potential discriminator for event classification.

FTS analysis of several HMEs detonated at ground level revealed spectral emissions dominated by continuum radiation and decaying in total intensity by an order of magnitude within approximately 300 ms after detonation. Signal attenuation by ground dust ejecta resulted in reduced signal-to-noise- ratios thus making it difficult to detect and classify emissions of selective radiation from detonation product gases at later times. The study of HME field detonations, especially at early times, is more robust using the 10 μ s temporal resolution of the radiometer data set.

2. Concluding Discussion of Key Findings

Analysis of fireball dynamics suggests a rapid growth to a fairly constant fireball size. This finding is a boon in the study of the temporal dependence of the fireball emissive area since we can further support the notion that emissivity is largely the cause of the time-varying emissive area. Previous studies have shown that characterization of observed infrared signatures from explosive events can lead to classification of different explosive types. Spectral features have been studied but little has been done to understand the temporal dependence in the extracted spectral features. Analysis of temporal dependence is important because it aids in improving the knowledge of the underlying kinetics of these features. This work is a step toward understanding the temporal dynamics of the temperature in a post-detonation combustion fireball. The derived detonation energy efficiencies in Chapter IV are negatively correlated with the heats of combustion in Chapter V suggesting that lower detonation efficiencies may result in more fuel available for post-detonation combustion at later times. The development of the empirical model fit parameters is based upon physical phenomena that considered

reaction rate kinetics, combustion fuel concentration, heat capacities, and vortex rotation rates and may tie these phenomena to the temperature extracted from spectral analysis. Although not singularly definitive as a classification scheme, the newly developed empirical model for temperature profiles of post-detonation combustion fireballs and the accompanying fireball and shock wave analyses have advanced the current state of optical forensics of field detonations from RDX-based aluminized novel munitions.

3. Future Efforts

The data set of 13 detonation events for this work is small and has little repeatability in the data. Improvements to this empirical model might benefit from application of this model to a data set with a much greater number of repeated events so that more robust correlations could be made between the physical quantities under observation and the model fit parameters.

Detailed examination of the oscillatory nature of the empirical model fit residuals may provide additional insight into phenomenology not presently addressed by the model. Also, evolution of the fireball emissive-area should be modeled using a low-dimensionality physics-based approach. The temporal dependence of fireball emissivity or area may reveal more information about the underlying kinetics of the explosion.

In-depth analysis of the 100 kHz radiometer data set is needed. The ratio of spectral irradiance or spectral intensity at two radiometer bands in the continuum region of the spectra may be used to corroborate temperature profiles used in the empirical model development. Unlike the spectrometer's 12 ms temporal resolution, the 10 μ s temporal resolution of the radiometer data set may offer a glimpse at the phenomenology

influencing the temperature spike that occurs at the first millisecond after detonation. Additionally, treatment of the fireball as a blackbody radiator allows estimation of the fireball projected area using radiometer intensity data. Consequently, analysis of fireball and shock front dynamics may be possible at early times after detonation. Exploitation of information harbored in discrete radiometric bands could lead to more reliable and portable sensor platform solutions.

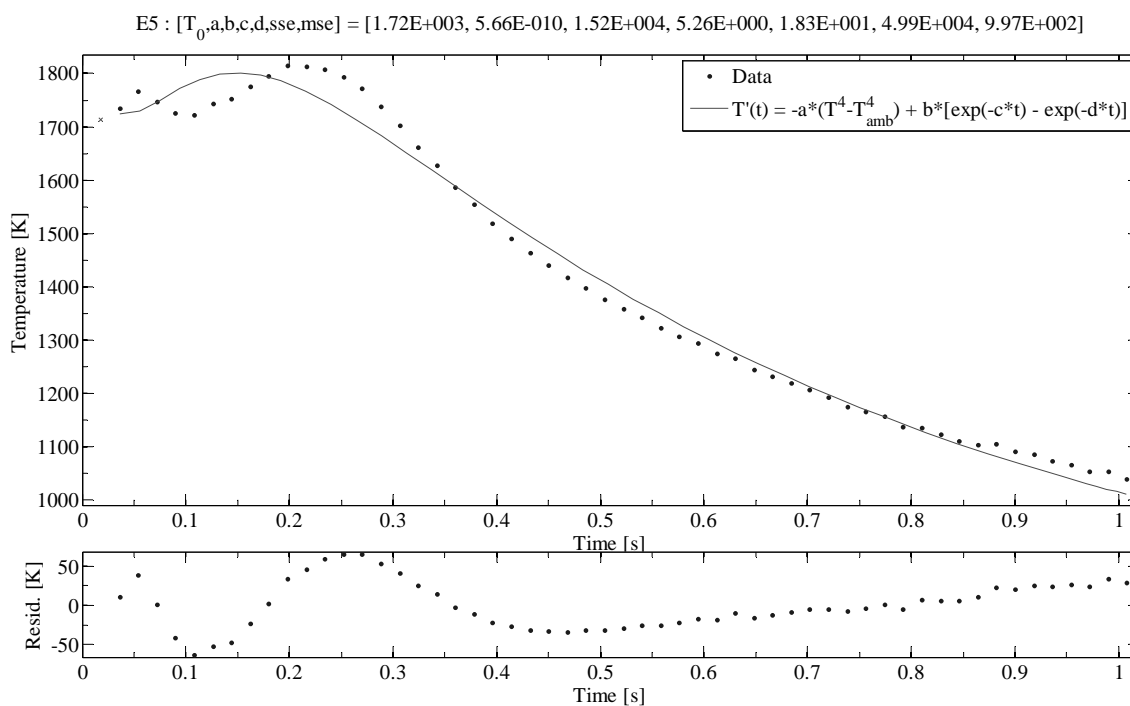
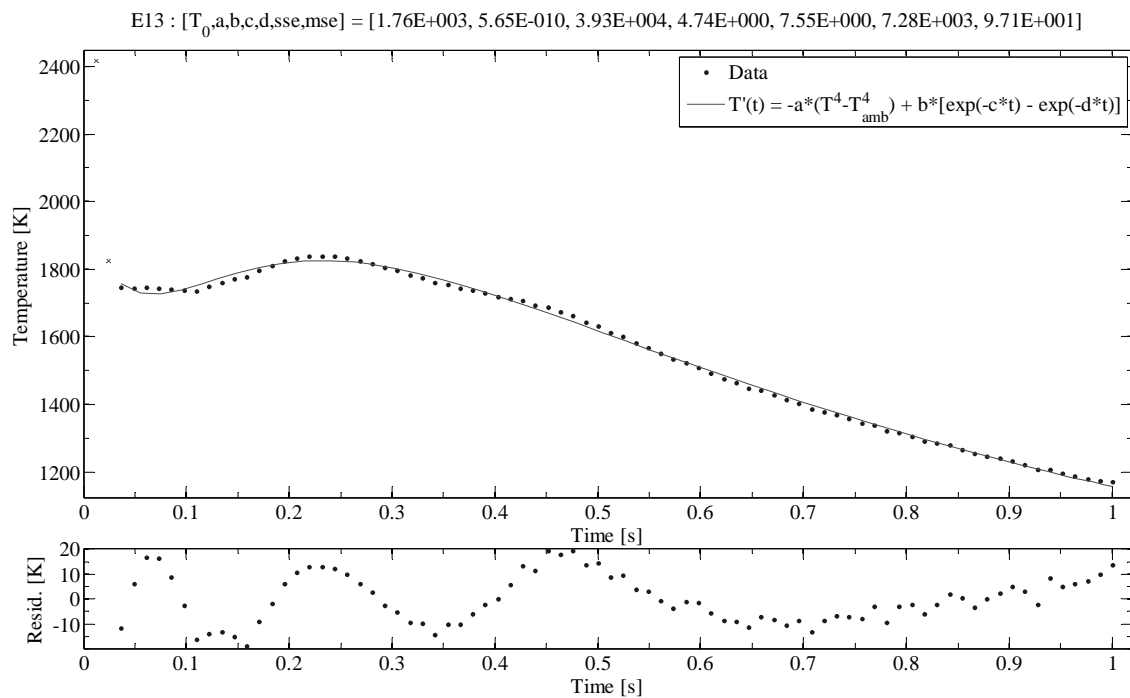
Appendix A. Empirical Model Fit to Data

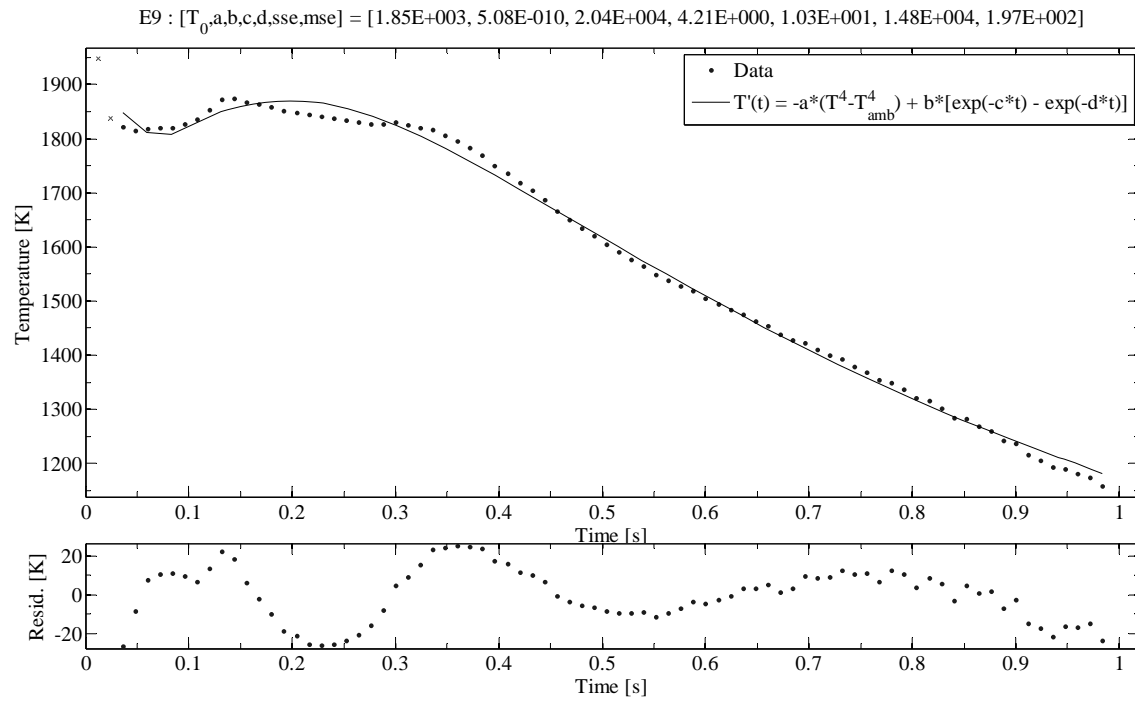
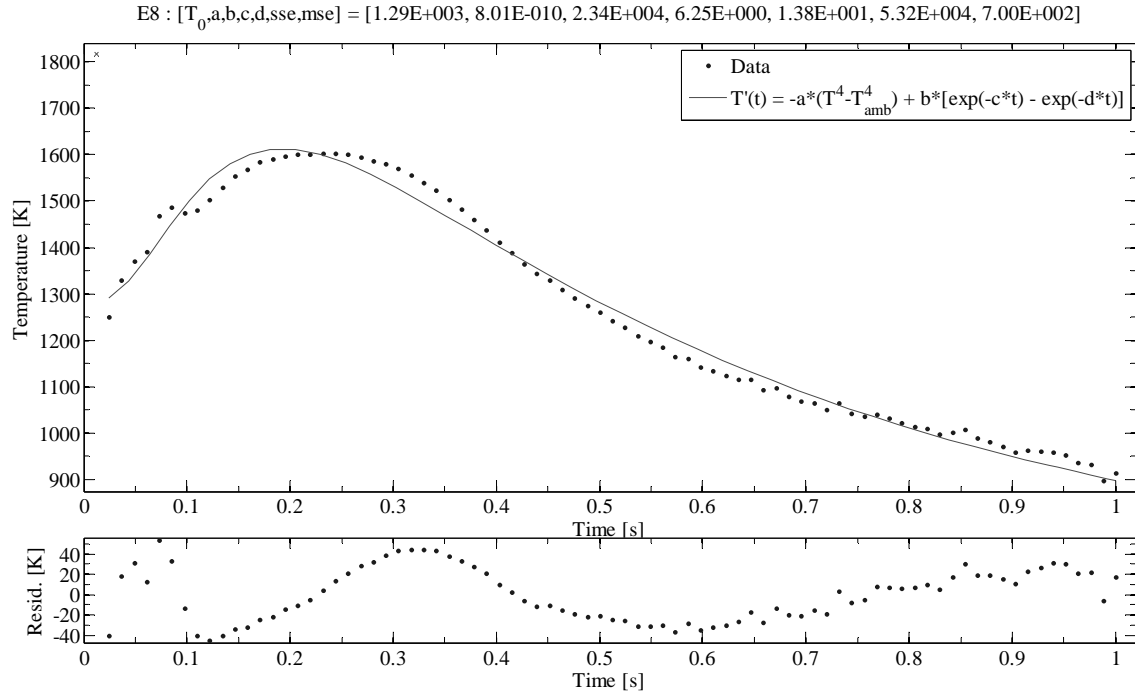
This appendix lists the plots of the five-parameter, physics-based empirical model, Eq. (17), fitted to data. The events are listed from highest-to-lowest amount of HE fill and are equivalent to listing them from least-to-most amount of liner. The individual points represent the temporally-resolved temperature data extracted from FTS spectra using the two-color best fit Planckian approach discussed in § 3.1. The solid line is the fitted numerical solution to Eq. (17), shown below, from § 3.2.

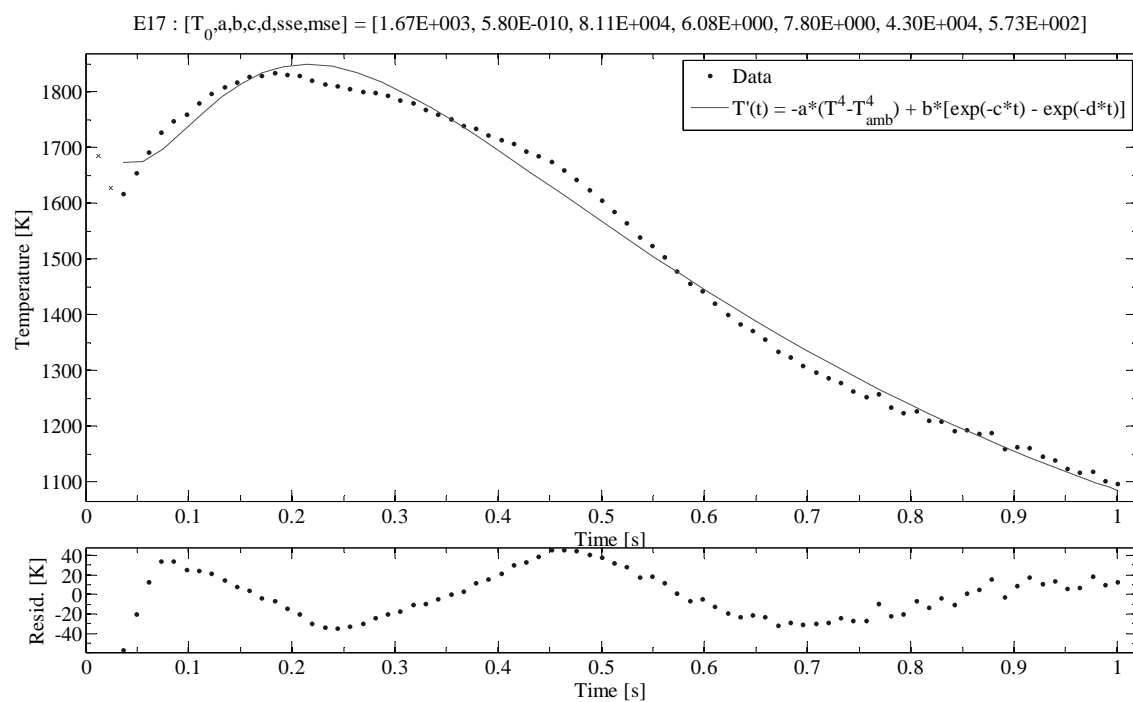
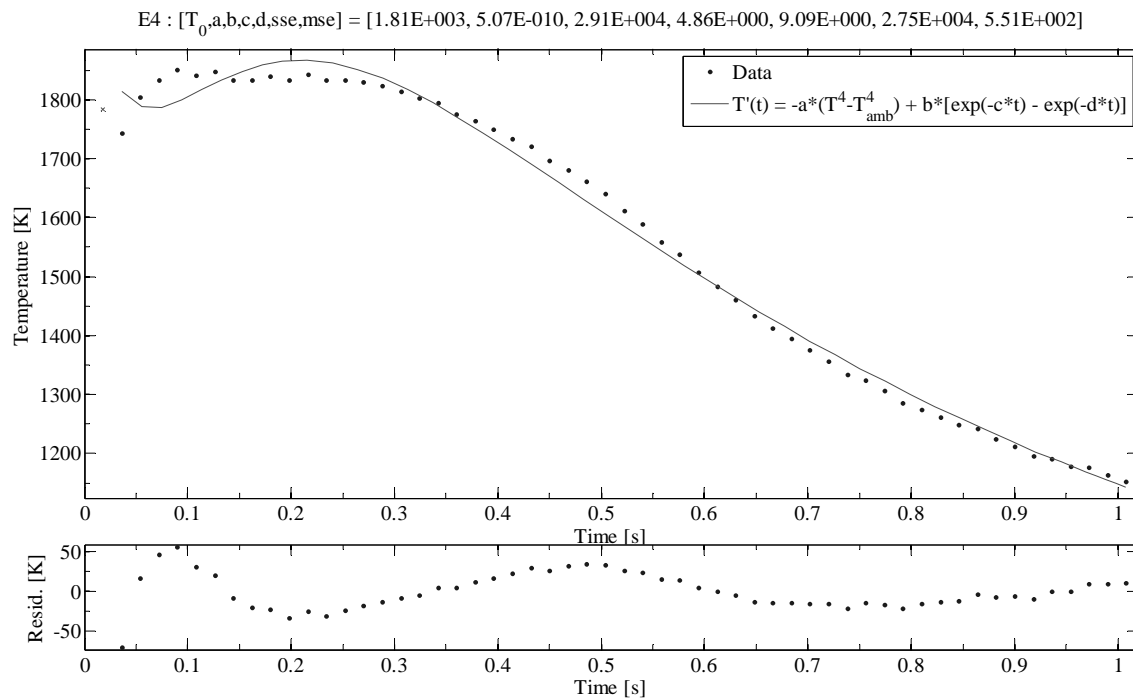
$$\frac{dT}{dt} = -a (T^4 - T_{atm}^4) + b (e^{-c t} - e^{-d t})$$

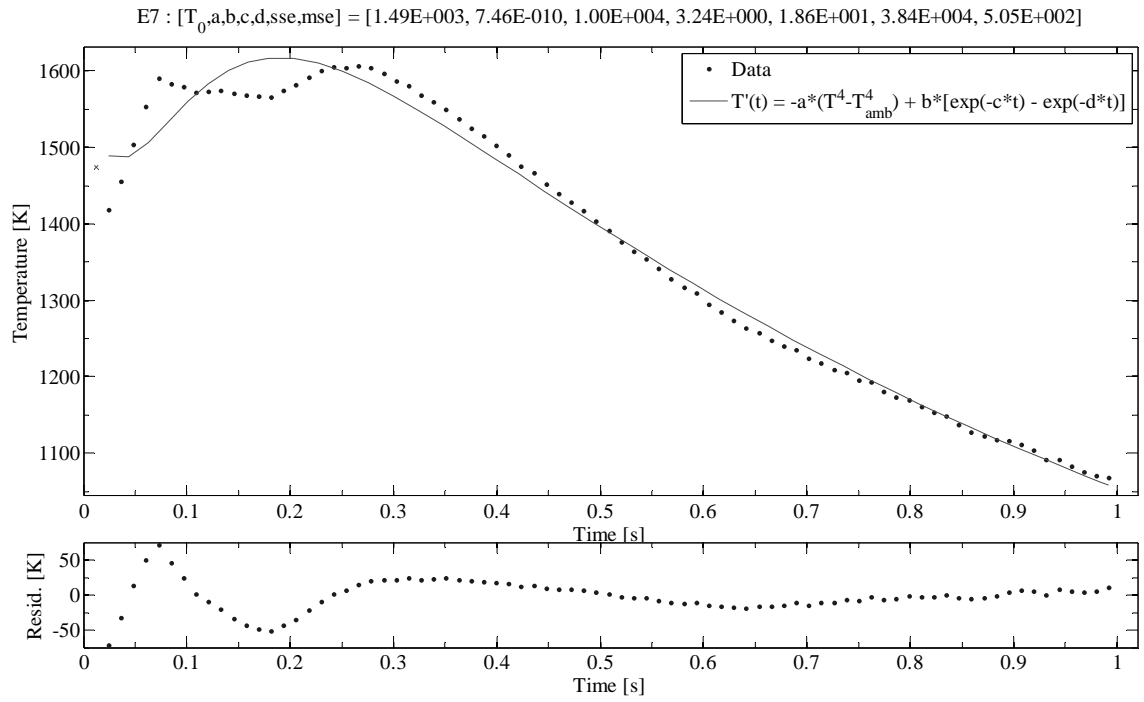
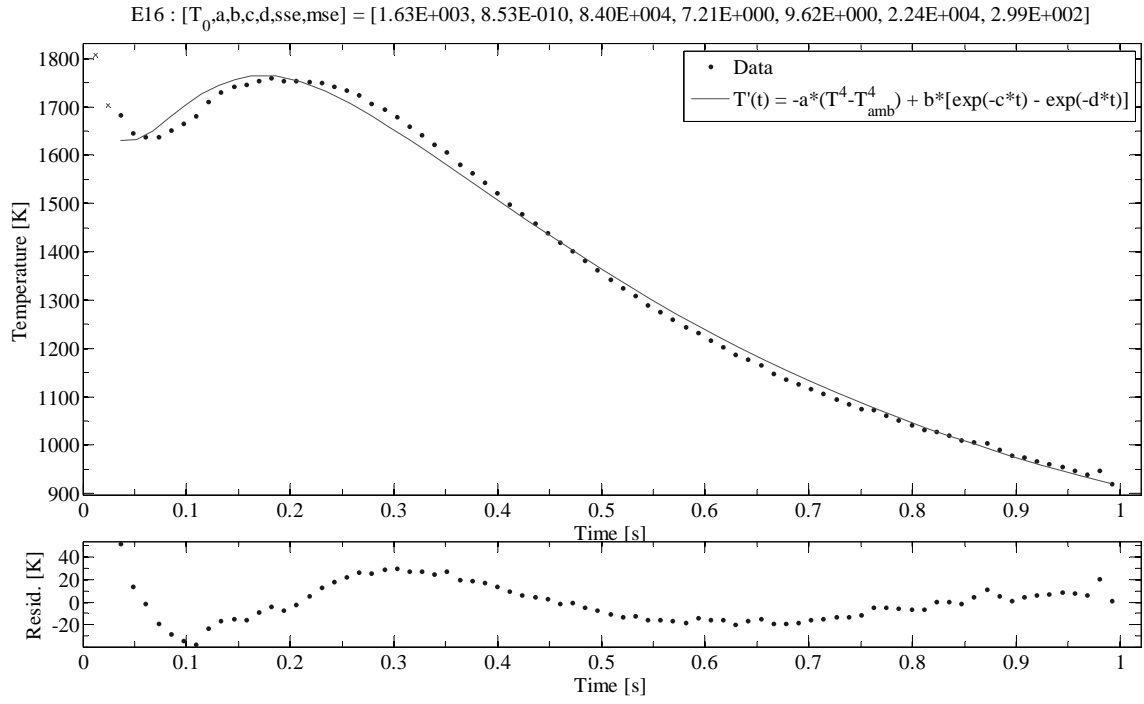
The five parameters are: (T_o) initial temperature, (a) radiative cooling coefficient, (b) combustion source coefficient, (c) and (d) exponential combustion source terms and are displayed at the top of each plot along with the sum of square error (sse) and mean square error (mse). The bottom panel of each plot represents fit residuals in a 95% confidence interval. The oscillatory nature of the fit residuals was not examined in detail although fireball vortices, turbulence, atmospheric conditions, and non-ideal detonation and combustion are likely contributors.

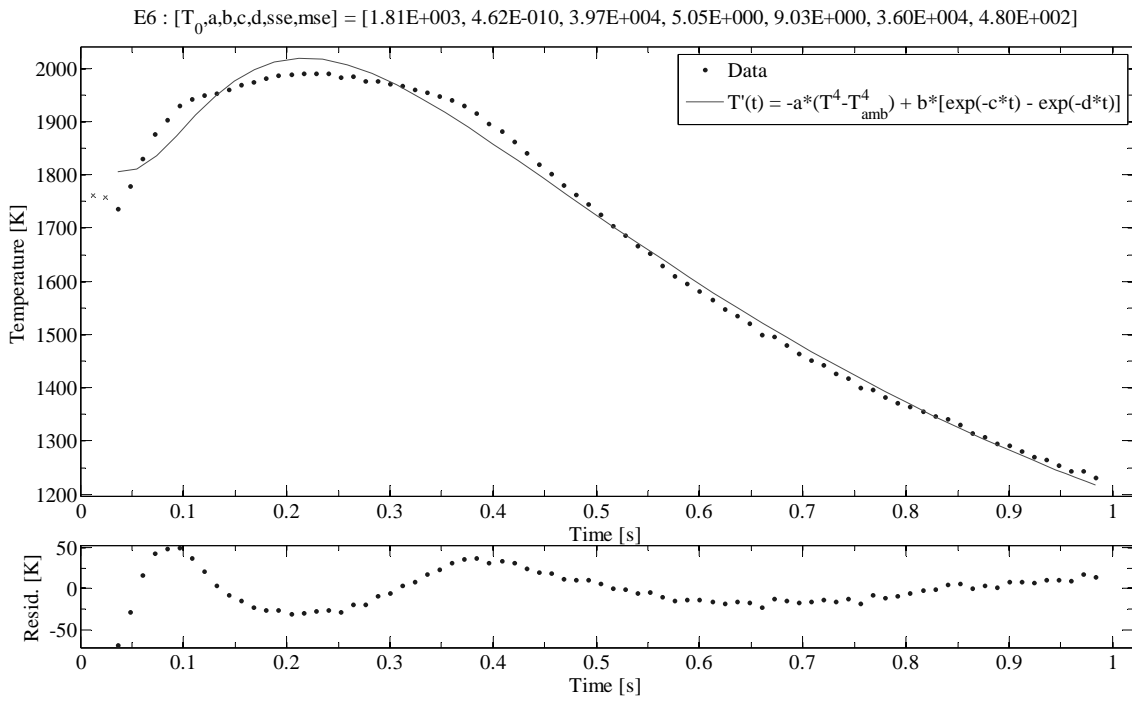
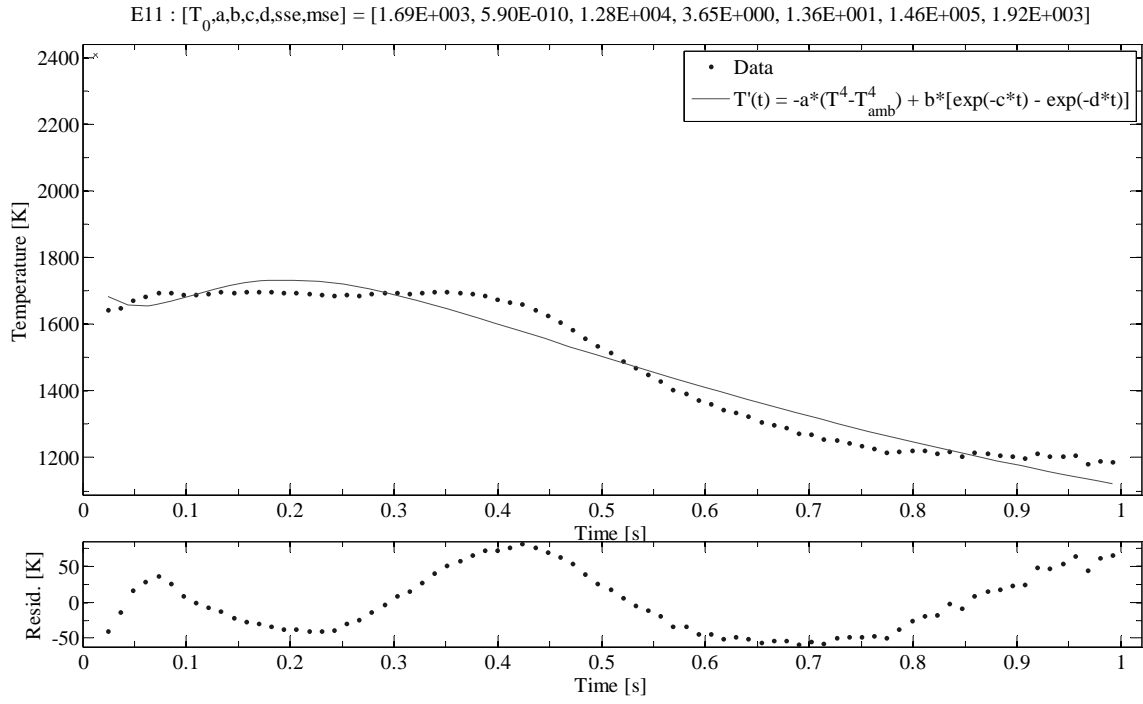
The first 1–2 data points (denoted with an “x”) are not included in the model fit as the present global empirical model is not suitable for describing the phenomenology immediately after detonation. Additionally, the validity of the first data point in the FTS-acquired signature may be suspect because the initial detonation happens much more quickly than the 12 ms temporal resolution of the FTS. Thus, one cannot be confident if the observed immediate temperature spike or trough upon detonation is physically accurate using FTS data alone.

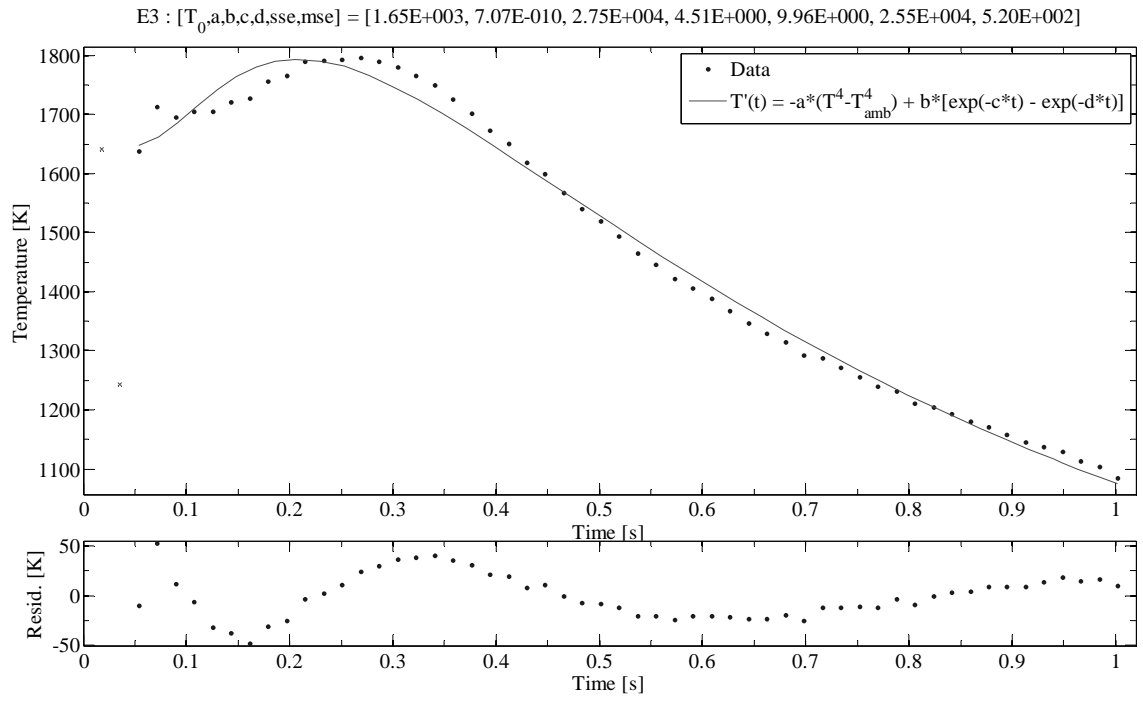
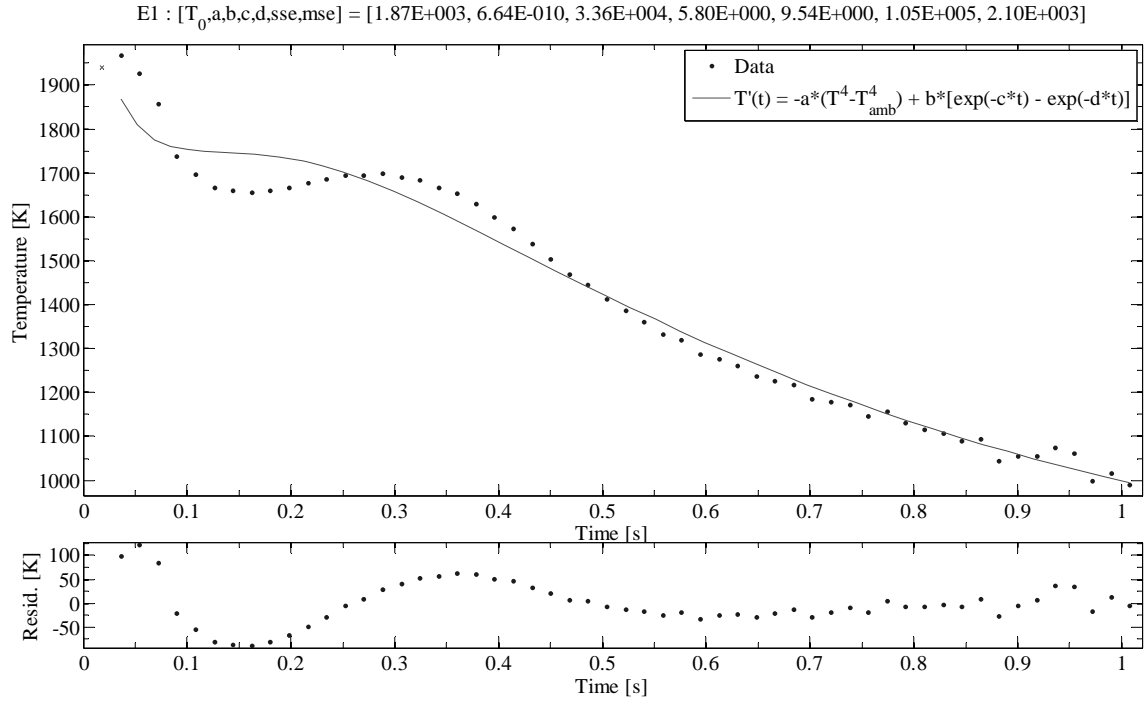












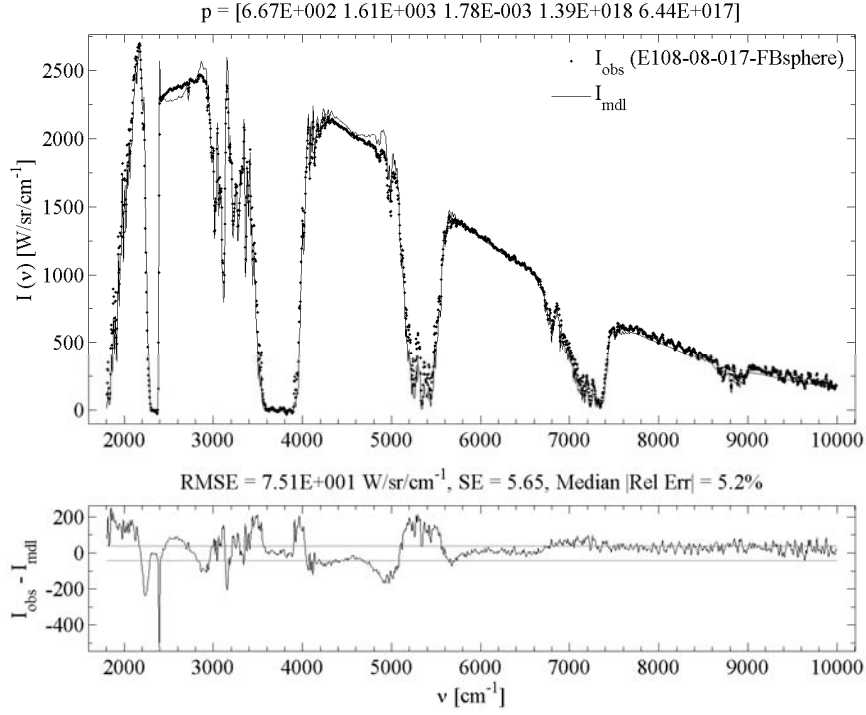
Appendix B. Gross Radiative Transfer Spectral Model Fit to Data

This appendix lists the Gross [28] radiative transfer spectral model, Eq. (15), fitted to the detonation fireball spectra of four representative events. The four events represent test articles whose total aluminum contents are: (E8) none, (E5) low, (E7) medium, and (E9) high. The Gross model is compared to spectra at about 200 ms and 800 ms to illustrate the temporal evolution of the detonation fireball, as well as highlight the model's ability to robustly describe 500–2000 points of spectral data using only a 5–7 parameter physics-based model.

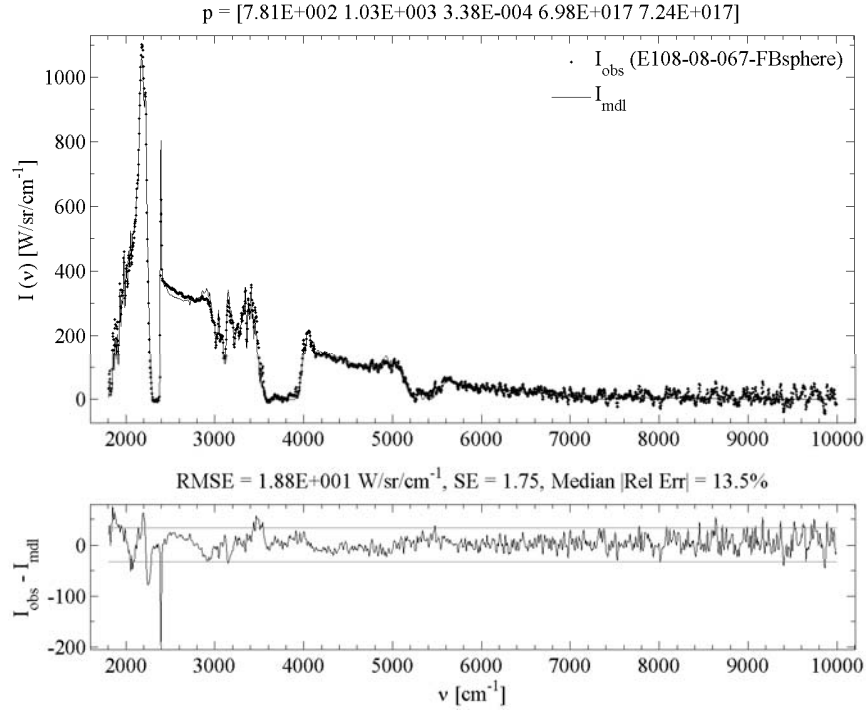
The model fit parameters are listed at the top of each plot and represent fireball emissive area, temperature, particulate (i.e., soot) absorption coefficient, CO₂ concentration, and H₂O concentration, respectively. The bottom panel of each plot represents the fit residuals in a 95% confidence interval. The root-mean-squared-error, standard fit error, and median magnitude of the relative error is listed above the fit residual panel.

The plots illustrate that at early times, the presence of selective emitters is largely masked by the blackbody behavior of the detonation fireball. As the fireball evolves, the presence of selective emitters in the wings of the atmospheric absorption bands is more readily discerned and the Gross spectral model is able to extract these characteristic discriminators for use in event classification.

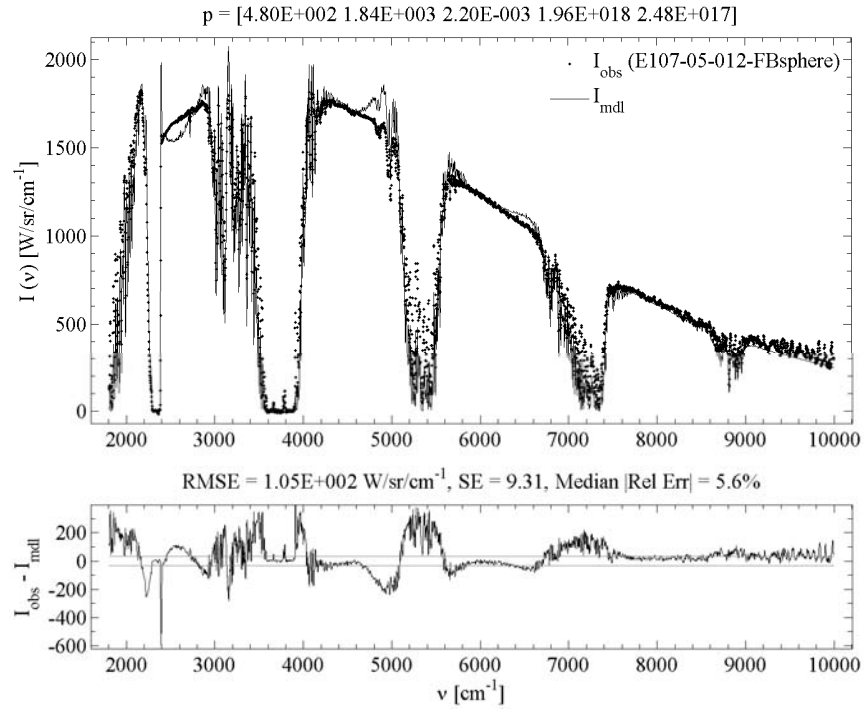
Event E8 at ~ 0.2 s



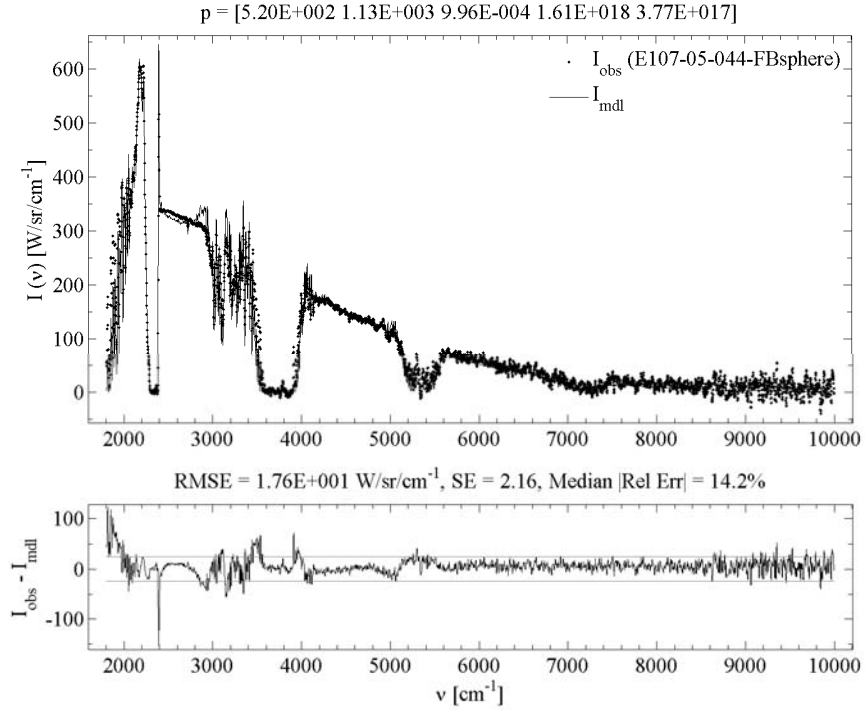
Event E8 at ~ 0.8 s



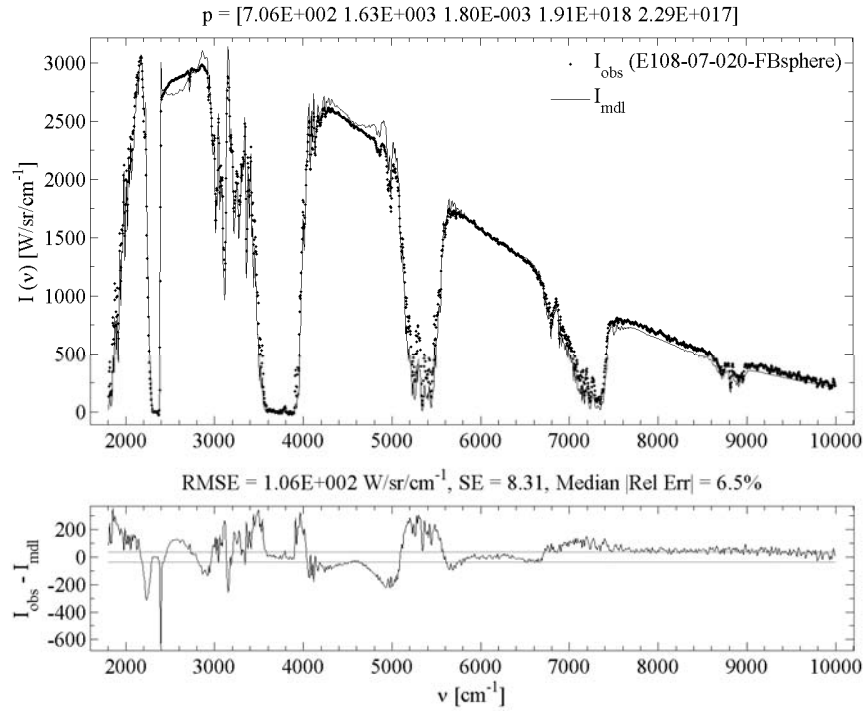
Event E5 at ~ 0.2 s



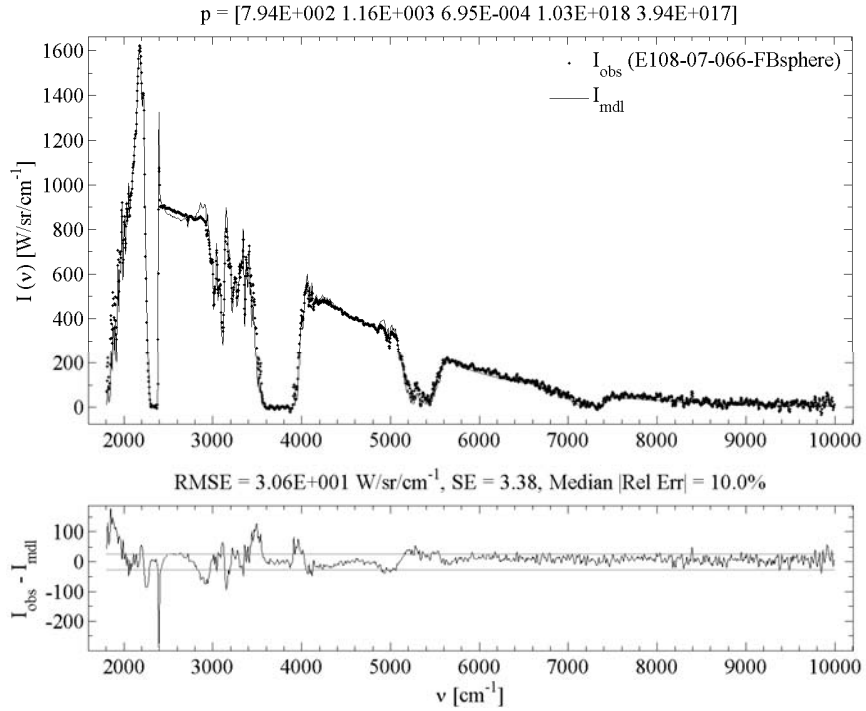
Event E5 at ~ 0.8 s



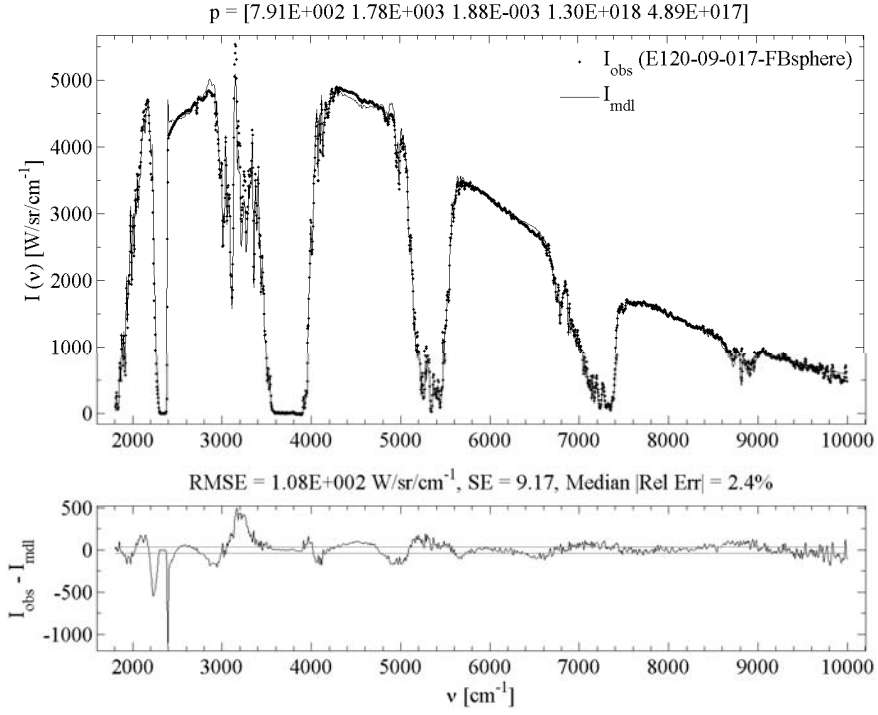
Event E7 at ~ 0.24 s



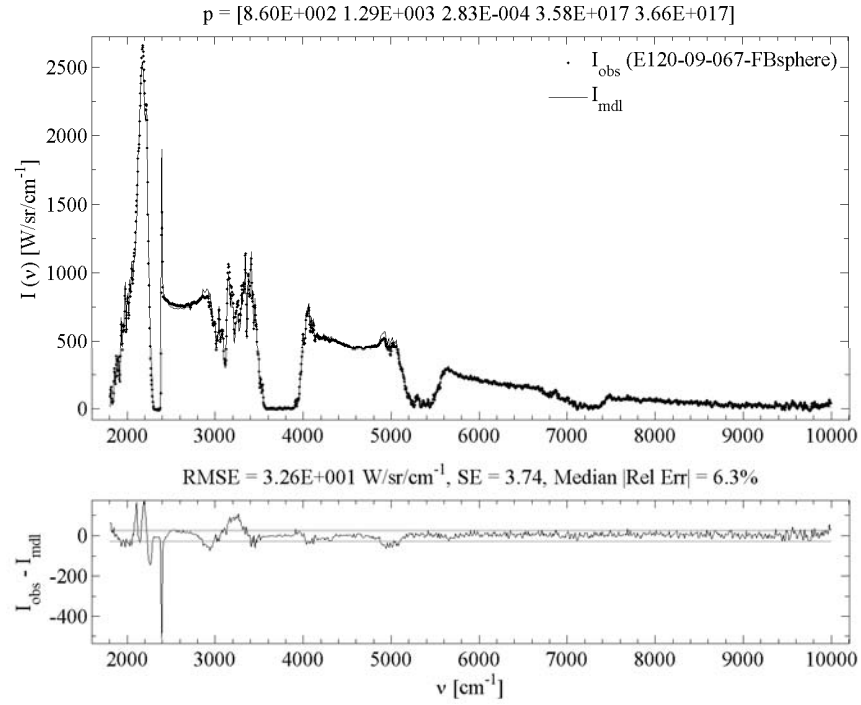
Event E7 at ~ 0.8 s



Event E9 at ~ 0.2 s



Event E9 at ~ 0.8 s



Appendix C. Theory

1. Spectrometer Basics

A spectrometer is an instrument that can measure the properties of photons in certain regions of the electromagnetic spectrum. At the heart of a spectrometer is an interferometer.

An interferometer, as the name suggests, measures the constructive and destructive interference of light. It is a device that collects beams of light, splits the beams into two using a beam splitter, temporally alters the path of one of the split beams using a moving mirror, and then re-combines or superimposes the two light beams at the beam splitter before they reach the detector where the constructive and destructive interference patterns are eventually displayed [55, p. 15]. Constructive interference occurs when the optical path difference (OPD) between the two split light beams is equal to multiples of the wavelength, λ . Destructive interference occurs when the OPD between the two beams is $1/2 \lambda$. For OPD other than λ or $1/2 \lambda$, a combination of constructive and destructive interference occurs and the beam intensity is somewhere between very bright and very dark. The variation of the observed intensity with OPD is detected as a cosine wave and the plot of light intensity versus OPD is called an interferogram. This interferogram can subsequently be Fourier transformed to produce a spectrum [55, p. 19]. This is where the name Fourier transform infrared spectrometer (FTS) comes from. A Michelson interferometer uses this principle and it is the type of FTS used in the instrument deployed to the field tests. Figure 33 below shows a diagram of a Michelson interferometer.

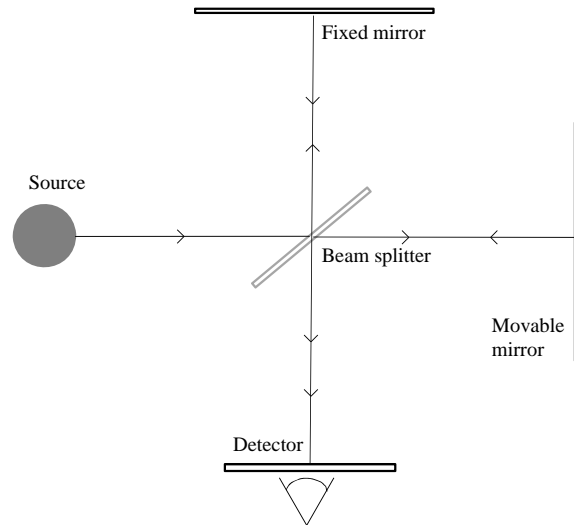


Figure 33. General schematic of a typical Michelson interferometer.

A spectrometer uses a semiconductor detector to detect certain wavelengths or frequencies of light, such as those in the midwave-infrared. The detector achieves this inherent photon sensitivity by exploiting the band gap properties of its respective semiconductor material (i.e., InSb, InGaAs, or HgCdTe). In this present research, an ABB Bomem MR-254 non-imaging spectrometer uses an InSb detector to sense photons in the 3–5 μm regions. An inbound photon of the required energy interacts with the InSb semiconductor band gap and produces a current which is then converted to a voltage and is subsequently interpreted as a detected signal.

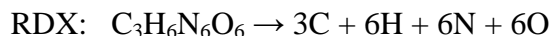
The Phantom v5.1 camera operates by using a complementary metal oxide semiconductor (CMOS) sensor to convert incoming light into an electrical charge using the photoelectric effect. The charge is accumulated on a capacitor in each pixel and thus converted into a voltage. Once accumulated, the voltage is then routed to a sensor output and the pixels are reset and the cycle repeats. This voltage signal is then digitized into a certain bit depth and stored into memory for display to the user.

2. Source of Blackbody Radiation

The emission of ro-vibrational spectra from select molecules (i.e., CO, H₂O, CO₂, etc) in the detonation fireball allows for the classification of a particular HE event. However, the problem of identification of these selective emitters is exacerbated by the presence of blackbody radiation in the detonation spectral signatures because the blackbody radiation effectively masks the presence of these emitters.

In the infrared spectra of an HE event, blackbody emission is likely due to the presence of soot in the detonation fireball. Soot can be defined as any carbonaceous by-product of the detonation. For example, one can take a simplified view of the detonation and represent the detonation event using a single component such as RDX (cyclotrimethylene-trinitramine). Determination of the detonation products and the stoichiometry of the reaction is then straight-forward.

Assuming ideal conditions and that the only source of oxygen is from the HE itself, we can progress through the oxidation reaction following certain “rules of thumb” [14, p. 22]:



- a) $6\text{N} \rightarrow 3\text{N}_2$
- b) $6\text{H} + 3\text{O} \rightarrow 3\text{H}_2\text{O}$ (3 O remaining)
- c) $3\text{C} + 3\text{O} \rightarrow 3\text{CO}$ (all the O is used up at this point; thus no CO₂ is formed)

Thus the stoichiometry of the overall detonation reaction is,



It is important to keep in mind that in the above simplified analysis, only detonation has occurred; combustion processes have not yet taken place. Recall that we are treating the detonation as ideal. In a non-ideal scenario, the carbon would not be completely

converted to CO in the detonation. In this case, carbonaceous by-products in the form of soot remain and it is this heated carbon soot that gives the fireball its characteristic blackbody signature.

In the initial stages of the HE event, this heated carbonaceous soot emits an overwhelming amount of blackbody radiation such that the spectral features from selective emitters (i.e., CO or CO₂) are masked. In other words, the FTS sees only the characteristic Planckian distribution of the soot's blackbody radiation at the detonation temperature. Figure 34 below shows this Planckian behavior roughly 20 ms after detonation of a high aluminum content test item. Only after combustion processes dominate and convert the carbon to CO₂ that the selective emitters begin to be discernable by the detector.

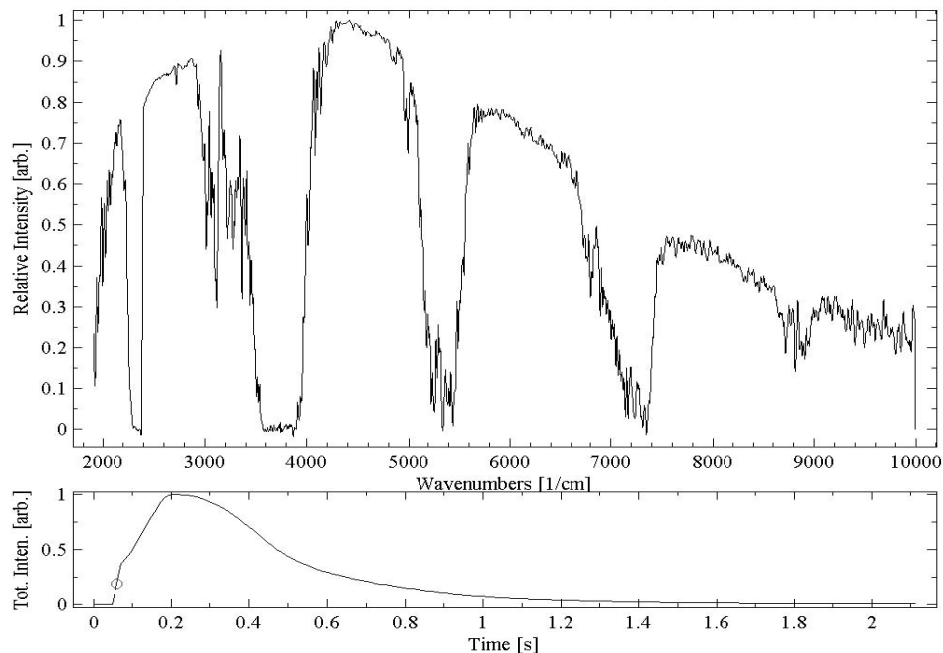


Figure 34. Early Planckian behavior of a detonation event. Note the circular reticle in the bottom plot of the integrated intensity indicating the temporal location of the above Planckian spectra.

There are likely other contributors to the overall observed blackbody radiation. They may come from the bomb casing material, asphaltic hot melt lining the walls of the munition, or perhaps from the aluminized munition liner.

3. Shock Wave Phenomenon

The shock wave phenomenon is a major consequence of the stress-strain relationship in a material (the general principle holds for solid, liquid, or gas). [14] Given a compressive stress-strain curve to very high stress level in Figure 35, one can see that in the elastic region, the sound velocity in the material is constant and the sound velocity, C , is proportional to the ratio of the change in pressure (P) with change in density (ρ) [14, p.

168]: $C = \frac{dP}{d\rho}$.

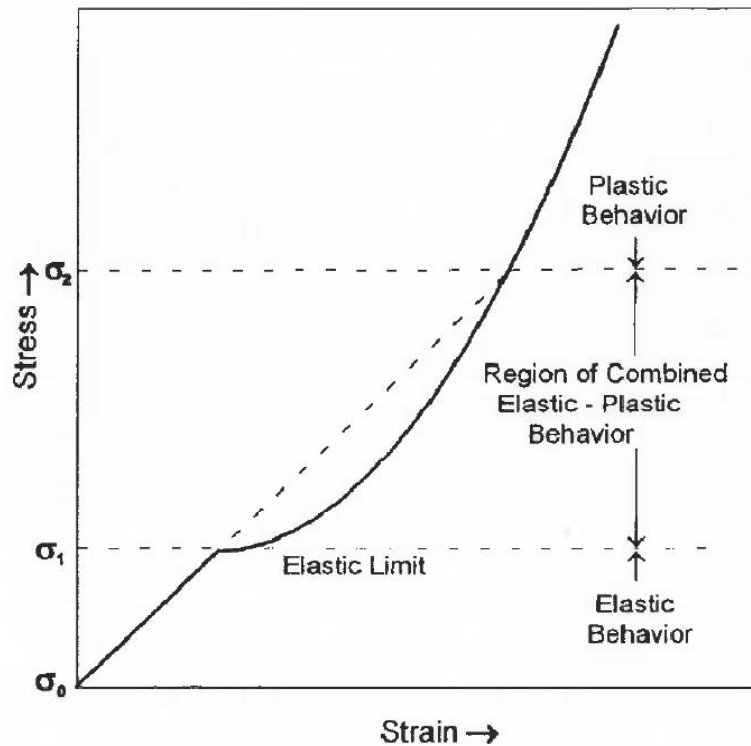


Figure 35. Typical compressive stress-strain curve to very high stress level [14, p. 168]

In the elastic region, P and ρ are linearly related, but above the elastic region sound velocity increases with pressure or density and P/ρ is no longer linear. This can be directly applied to a pressure wave (which will eventually be called the shock wave).

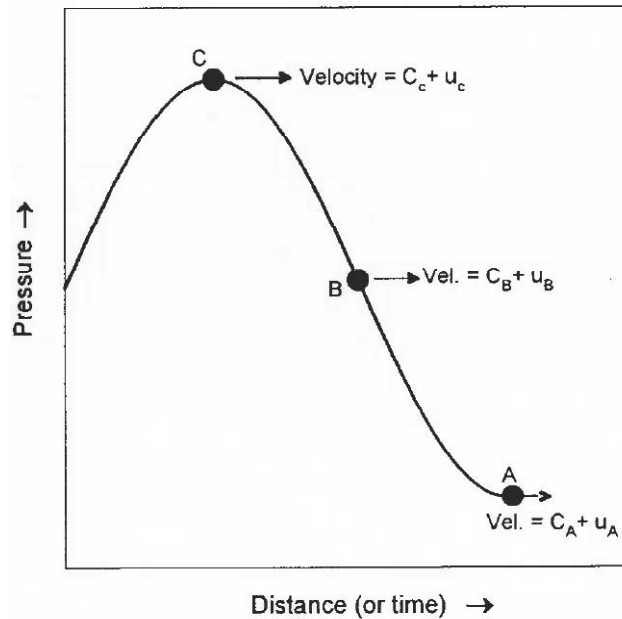


Figure 36. Pressure wave (or shock wave) at high pressure [14, p. 169]

Figure 36 above shows a pressure wave at high pressure like that to be found during an explosion. The crest of the wave is at low pressure in the wave front. The middle of the wave is higher than the crest of the wave, but the apex of the wave is higher in pressure than the middle part of the wave front. Since we are above the elastic limit (for an explosion event), the pressure velocity increases with increased pressure. So, the top of the wave moves faster than the middle of the wave which moves faster than the lowest

part of the wave. Thus at some distance (or point in time), the upper part of the wave will catch up with the lower part of the wave such that the waveform looks like a vertical line or front. When the wave has this characteristic vertical front, it is called a shock wave.

There is no smooth transition from one side of the shock front to the other and so we say that the matter “jumps” from the unshocked to the shocked state and is called a discontinuity. It is worth clarifying at this point that pressure velocity = shock wave velocity = sound velocity + particle velocity. [14, p. 171]

Of course the shock wave cannot propagate indefinitely. As the shock wave travels, it is attenuated from behind by a rarefaction wave [14, p. 174]. Another mechanism for the slowing of the shock wave is its decreasing energy density as a function of distance or time (i.e., an energy transfer from the shock front to the environment). As the shock wave expands, its surface area gets larger and larger. Given that its initial energy was of finite quantity, its energy per unit surface area will eventually become extremely small and approach ambient air values.

We can use the Taylor-Sedov blast wave theory to write the shock radius as a function of time using the following equation:

$$r(t) = \zeta_n \left(\frac{E_0}{\rho_{air}} \right)^{\frac{1}{5}} t^{\frac{2}{5}}$$

We can take the first derivative of the above to get the shock velocity:

$$v(t) = \zeta_n \frac{2}{5} \left(\frac{E_0}{\rho_{air}} \right)^{\frac{1}{5}} t^{\frac{-3}{5}}$$

Now, re-arranging the above for E_0 gives:

$$E_0 = [v(t)]^5 t^3 \rho_{air} \left(\frac{5}{2}\right)^5 \left(\frac{1}{\zeta_n^5}\right)$$

E_0 can give us an estimate of the actual energy released by the detonation. The above equations are valid only in the mid-field [22; 59, p. 20].

Appendix D. Sample Calculation

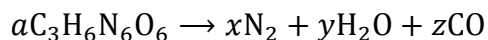
Recall our initial assumption that the liner does not participate in the detonation reaction of the HE, but does play a role in the post-detonation combustion. Thus, we can treat the combustion of the HE detonation products and combustion of the liner as two distinct processes, calculate their respective heats of combustion, and sum the two quantities to arrive at an overall heat of combustion for the event.

There are many elementary reactions and pathways that a reaction can take to get to the final products and the liberation of heat energy. As a simplifying assumption, we will only look at the overall reaction stoichiometry in order to determine the heats of detonation and combustion. The temperature of 1300 K has been selected as a reasonable temperature at which to use tabulated heats of formation from the NIST database [12] as this temperature is common to all detonation events.

We will follow Cooper's [14] reaction product hierarchy rules of thumb in order to determine the oxidation products used in the reaction stoichiometry.

1. Heat of Detonation (RDX only HE)

Detonation Stoichiometry:



$$\text{N: } 6a = 2x \quad \rightarrow \quad x = 3a$$

$$\text{H: } 6a = 2y \quad \rightarrow \quad y = 3a$$

$$\text{C: } 3a = z \quad \rightarrow \quad z = 3a$$

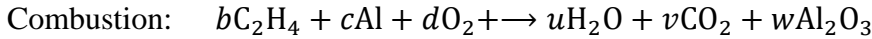
$$\text{O: } 6a = y + z$$

For event E4, we convert pounds of RDX into equivalent moles and use NIST tabulated heats of formation at 1300K to get:

$$\begin{aligned}
\Delta H_{d(RDX)} &= \# \text{ moles} * \Delta H_f^o(\text{products}) - \# \text{ moles} * \Delta H_f^o(\text{reactants}) \\
&= [x * \Delta H_f^o(\text{N}_2) + y * \Delta H_f^o(\text{H}_2\text{O}) + z * \Delta H_f^o(\text{CO})] - [a * \Delta H_f^o(RDX)] \\
&= \left[117.87 \text{ mols} * \left(0 \frac{\text{kJ}}{\text{mol}} \right) + 117.87 \text{ mols} * \left(-285.84 \frac{\text{kJ}}{\text{mol}} \right) \right. \\
&\quad \left. + 117.87 \text{ mols} * \left(-113.87 \frac{\text{kJ}}{\text{mol}} \right) \right] - \left[39.29 \text{ mols} * \left(61.55 \frac{\text{kJ}}{\text{mol}} \right) \right] \\
&= -49\,533 \text{ kJ}
\end{aligned}$$

2. Heat of Combustion (PE-Al Liner + RDX-Al-wax HE)

PE-Al Liner



$$\begin{aligned}
H: 4b &= 2u & \rightarrow & u = 2b \\
C: 2b &= v & \rightarrow & v = 2b \\
Al: c &= 2w & \rightarrow & w = c/2 \\
O: 2d &= u + 2v + 3w
\end{aligned}$$

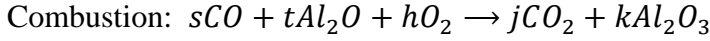
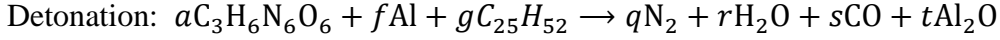
Now,

$$d = \frac{u + 2v + 3w}{2} = \frac{2b + 2(2b) + 3(c/2)}{2} = \frac{6b + (3/2)c}{2} = 3b + (3/4)c$$

For event E4, we convert pounds of liner material into equivalent moles and use NIST tabulated heats of formation at 1300K to get:

$$\begin{aligned}
\Delta H_{c(Liner)} &= \# \text{ moles} * \Delta H_f^o(\text{products}) - \# \text{ moles} * \Delta H_f^o(\text{reactants}) \\
&= [u * \Delta H_f^o(\text{H}_2\text{O}) + v * \Delta H_f^o(\text{CO}_2) + w * \Delta H_f^o(\text{Al}_2\text{O}_3)] \\
&\quad - [b * \Delta H_f^o(\text{P.E.}) + c * \Delta H_f^o(\text{Al}) + d * \Delta H_f^o(\text{O}_2)] \\
&= \left[89.4 \text{ mols} * \left(-249.47 \frac{\text{kJ}}{\text{mol}} \right) + 89.4 \text{ mols} * \left(-395.26 \frac{\text{kJ}}{\text{mol}} \right) \right. \\
&\quad \left. + 7.52 \text{ mols} * \left(-1690.19 \frac{\text{kJ}}{\text{mol}} \right) \right] - \left[44.71 \text{ mols} * \left(36.13 \frac{\text{kJ}}{\text{mol}} \right) \right. \\
&\quad \left. + 15.04 \text{ mols} * \left(0 \frac{\text{kJ}}{\text{mol}} \right) + 145.41 \text{ mols} * \left(0 \frac{\text{kJ}}{\text{mol}} \right) \right] \\
&= -71\,976.12 \text{ J}
\end{aligned}$$

RDX-Al-wax HE



$$\begin{array}{lll} C: s = j & \rightarrow & j = 3a + 25g \\ Al: 2t = 2k & \rightarrow & k = f/2 \\ O: s + t + 2h = 2j + 3k & \rightarrow & h = ((2j + 3k - s - t))/2 \\ & & h = [3a + 25g + 3(f/2)]/2 \end{array}$$

For event E4, we convert pounds of HE constituents into equivalent moles and use NIST tabulated heats of formation at 1300K to get:

$$\begin{aligned} \Delta H_{c(HE)} &= \# \text{ moles} * \Delta H_f^o(\text{products}) - \# \text{ moles} * \Delta H_f^o(\text{reactants}) \\ &= [j * \Delta H_f^o(CO_2) + k * \Delta H_f^o(Al_2O_3)] \\ &\quad - [s * \Delta H_f^o(CO) + t * \Delta H_f^o(Al_2O) + h * \Delta H_f^o(O_2)] \\ &= \left[279.92 \text{ mols} * \left(-395.26 \frac{\text{kJ}}{\text{mol}} \right) + 11.86 \text{ mols} * \left(-1690.19 \frac{\text{kJ}}{\text{mol}} \right) \right] \\ &\quad - \left[279.92 \text{ mols} * \left(-113.87 \frac{\text{kJ}}{\text{mol}} \right) + 11.86 \text{ mols} * \left(-183.47 \frac{\text{kJ}}{\text{mol}} \right) \right. \\ &\quad \left. + 151.81 \text{ mols} * \left(0 \frac{\text{kJ}}{\text{mol}} \right) \right] \\ &= -96\,636 \text{ kJ} \end{aligned}$$

Thus, the overall heat of combustion for event E4 is:

$$\begin{aligned} \Delta H_{c(E4)} &= \Delta H_{c(Liner)} + \Delta H_{c(HE)} \\ &= -71\,976 - 96\,636 \text{ kJ} \\ &= -168\,600 \text{ kJ} \end{aligned}$$

Bibliography

1. Anderson, J. G., G. Katselis, C. Caputo. *Analysis of a Generic Warhead Part I: Experimental and Computational Assessment of Free Field Overpressure*, DSTO-TR-1313. Australian Defence Science and Technology Organisation, Systems and Sciences Laboratory, Edinburgh, South Australia, 2002.
2. Askar'yan, G. A., M. A. Rabinovich, M. M. Savchenko, V. K. Stepanov, and P. N. Lebedev, "Optical breakdown fireball in the focus of a laser beam," *ZhETF Pis'ma* 5, vol. 5, pp. 150-154, 1967.
3. Bagby, W. F. *Spectral and temporal characterization of high-temperature events*. M.S. Thesis, AFIT/GAP/ENP/01M-01, Department of Engineering Physics, Air Force Institute of Technology, 2001.
4. Baker, W. E. *Explosions in Air*, Austin, TX, University of Texas Press, 1973.
5. Baum, F. A., K. P. Stanyukovich, and B. I. Shekhter. Translated by U.S. Army Research Information Service. *Physics of an Explosion*. Russian Book: FITZMATGIZ, Moscow, 1959.
6. Bjorklund, J. R., J. F. Bowers, G. C. Dodd, and J. M. White, *Open Burn / Open Detonation Dispersion Model (OBODM) User's Guide Volume II. Technical Description*, DPG Document No. DPG-TR-96008b, U.S. Army Dugway Proving Grounds, 1998.
7. Brousseau, P., H. E. Dorsett, M. D. Cliff, and C. J. Anderson, "Detonation properties of explosives containing nanometric aluminum powder," in *Int. Det. Symp.*, 2002.
8. Callies, G., P. Berger, and H. Hugel, "Time-resolved observation of gas-dynamic discontinuities arising during excimer-laser ablation and their interpretation," *J. Phys. D*, vol. 28, no. 4, pp. 794-806, 1995.
9. Carney, J. R., J. S. Miller, J. C. Gump, and G. I. Pangilinan, "Time-resolved optical measurements of the post-detonation combustion of aluminized explosives," *Rev. Sci. Instr.*, vol. 77, 2006.
10. Carney, J. R., J. S. Miller, J. C. Gump, and G. I. Pangilinan, "Atmospheric effects on the combustion of detonating aluminized explosives," in *Shock Compress. Cond. Matt.*, vol. 845, pp. 948-951, 2006.

11. Carney, J. R., J. Wilkinson, and J. M. Lightstone, "Time-resolved optical measurements of detonation and combustion products," in *Shock Compress. Cond. Matt.*, 2007.
12. Chase, M. W. Jr., (Ed.), *NIST-JANAF Thermochemical Tables (Journal of Physical and Chemical Reference Data Monographs)*, 4th Edition, American Institute of Physics, New York, 1998.
13. Cook, M. A., A. S. Filler, R. T. Keyes, W. S. Partridge, and W. Ursenbach, "Aluminized explosives," *J.Phys.Chem.*, vol. 61, no. 2, pp. 189-196, 1957.
14. Cooper, P. W. *Explosives Engineering*. VCH Publishers, New York, New York, 1996.
15. Cox, D. B., "Theoretical structure and spectrum of a shock wave in the interstellar medium: The Cygnu Loop," *Astrophys. J.*, vol. 178, pp.143-157, 1972.
16. Diaci, J. and J. Možina, "Investigation of blast waves generated by laser induced damage processes," *Opt.Commun.*, vol. 90, no. 1-3, pp. 73-78, 1992.
17. Dills, A. N., *Classification of battle space detonations from temporally resolved multi-band imagery and mid-infrared spectra*. Ph.D. Dissertation, AFIT/DS/ENP/05/-01, Department of Engineering Physics, Air Force Institute of Technology, 2005.
18. Dills, A. N., K. C. Gross, and G. P. Perram, "Detonation discrimination techniques using a Fourier Transform Infrared Spectrometer system and a Near-Infrared Focal Plane Array," in *Proc. of SPIE*, vol. 5075, pp. 208-216, 2003.
19. Dills, A. N., S. C. Gustafson, and G. P. Perram, "Detonation discrimination and feature saliency using a near-infrared focal plane array and a visible CCD camera" in *Proc. of SPIE*, vol. 5811, no. 1, pp. 123-132, 2005.
20. Dills, A. N., G. P. Perram, and S. C. Gustafson. "Detonation discrimination techniques using a near-infrared focal plane array camera," in *Proc. of SPIE*, vol. 5431, pp. 77-86, 2004.
21. Dokuchaev, V. I., "Self-similar spherical shock solution with sustained energy injection," *Astronomy and Astrophysics*, vol. 395, pp. 1023, 2006.
22. Geohegan, D. B., "Fast intensified-CCD photography of YBa₂Cu₃O_{7-x} laser ablation in vacuum and ambient oxygen," *Appl. Phys. Lett.*, vol. 60, no. 22, pp. 2732-2734, June 1992.

23. Gilev, S. D. and V. F. Anisichkin, "Interaction of Aluminum with Detonation Products," *Combust., Expl., Shock Waves*, vol. 42, no. 1, 107-115, 2006.
24. Gogulya, M. F., A. Y. Dolgoborodov, and M. A. Brazhnikov, "Investigation of shock and detonation waves by optical pyrometry," *Int. J. Impact Eng.*, vol. 23, pp. 283-293, 1999.
25. Gonzalez, R. C., R. E. Woods, and S. L. Eddins, *Digital Image Processing Using Matlab*. Upper Saddle River, U.S.A.: Pearson Prentice-Hall, 2004.
26. Gordon, J. Motos, K. C. Gross, and G. P. Perram, "Temporally-resolved, infrared spectra from the detonation of advanced munitions," in *Proc. of SPIE*, vol. 7330, p. 733006, 2009.
27. Gordon, J. Motos, M. S. Spidell, J. Pitz, K. C. Gross, and G. P. Perram, "High speed spectral measurements of IED detonation fireballs," in *Proc. of SPIE*, vol. 7665, p. 76650S, 2010.
28. Gross, K. C. *Phenomenological model for infrared emissions from high-explosive detonation fireballs*. Ph.D. Dissertation, AFIT/DS/ENP/07-03, Department of Engineering Physics, Air Force Institute of Technology, 2007.
29. Gross, K. C., A. N. Dills, G. P. Perram, and R. F. Tuttle. "Phenomenology of Exploding Ordnance Using Spectrally and Temporally Resolved Infrared Emissions," in *Proc. of SPIE*, vol. 5075, pp.21 7-227, 2003.
30. Gross, K. C. and G. P. Perram, "The phenomenology of high explosive fireballs from fielded spectroscopic and imaging sensors for event classification." *Int. J. High Speed Electron. Syst.*, vol. 18, no. 1, p.19-29, 11p., 2008.
31. Gross, K.C.; G. P. Perram, R. F. Tuttle, "Modeling infrared spectral intensity data from bomb detonations" in *Proc. of SPIE*, vol. 5811, no. 1, pp. 100-11, 2005.
32. Gross, K. C., J. Wayman, and G. P. Perram, "Phenomenological fireball model for remote identification of high-explosives" in *Proc. of SPIE*, vol. 6566, p. 656613, 2007.
33. Gross, K. C., A. M. Young, C. Borel, B. J. Steward, and G. P. Perram, "Simulating systematic scene-change artifacts in Fourier-transform spectroscopy," in *Proc. of SPIE*, vol. 7695, 2010.
34. Herr, K. C., D. K. Stone, and D. S. Urevig. *Infrared spectroscopy of high explosive detonations: the Sandia experiments*, Report Number ATR-82(7953)-1. Aerospace Corporation, Laboratory Operations, El Segundo, California, 1982.

35. Jamieson, G. E. and G.C., Jr. Wetsel, "Optical-Beam-Deflection Probing of Blast Waves Near Solid Surfaces," in *IEEE 1985 Ultrasonics Symp. Proc.*, pp. 451-456, 1985.
36. Jeong, S. H., R. Greif, and R. E. Russo, "Propagation of the shock wave generated from excimer laser heating of aluminum targets in comparison with ideal blast wave theory," *Appl. Surf. Sci.*, vol. 127-129, pp. 1029-1034, 1998.
37. Kansa, E. J., "A time-dependent buoyant puff model for explosive sources," Lawrence Livermore National Laboratory, UCRL-ID-128733 Rev. 1, 1997.
38. Keshavarz, M. H., H. Motamedoshariati, R. Moghayadnia, H. R. Nazari, and J. Azarniamehraban, "A new computer code to evaluate detonation performance of high explosives and their thermochemical properties, part I," *J. Hazard. Mater.*, vol. 172, no. 2-3, pp. 1218-1228, 2009.
39. Kick, H., V. Tank, and E. Lindermeir, "Impact of scene changes during data acquisition in Fourier spectroscopy," *J. Quant. Spectrosc. Radiat. Transfer*, vol. 92, pp. 447-455, 2004.
40. Lee, S. J., K. Imen, and S. D. Allen, "Shock wave analysis of laser assisted particle removal," *J. Appl. Phys.*, vol. 74, no. 12, pp. 7044-7049, 1993.
41. Lefrancois, A., G. Baudin, C. L. Gallic, P. Boyce, and J-P Coudoing, "Nanometric aluminium powder influence on the detonation efficiency of explosives," in *Int. Det. Symp.*, 2002.
42. Lewis, W. K. and C. G. Rumchik, "Measurement of apparent temperature in post-detonation fireballs using atomic emission spectroscopy," *J. Appl. Phys.*, vol. 105, 2009.
43. Misra, A. and R. K. Thareja, "Investigation of laser ablated plumes using fast photography," *IEEE Trans. Plasma Sci.*, vol. 27, no. 6, pp. 1553-1558, 1999.
44. Modest, M. F. *Radiative Heat Transfer*, McGraw-Hill, Inc. New York, New York, 1993.
45. Needham, C. E. *Blast Waves*, Springer-Verlag, Heidelberg, Germany, 2010.
46. Orson, Jay A. *Collection of detonation signatures and characterization of spectral features*. M.S. Thesis, AFIT/GSO/ENP/00M-01, Department of Engineering Physics, Air Force Institute of Technology, 2000.
47. Orson, J. A., W. F. Bagby, and G. P. Perram, "Infrared signatures from bomb detonations," *Infrared Phys. Tech.*, vol. 44, no. 2, p. 101, 7p., 2003.

48. Peucker, J. M., P. Lynch, H. Krier, and N. Glumac, "Optical depth measurements of fireballs from aluminized high explosives," *Optics Lasers Eng.*, vol. 47, no. 9, pp. 1009-1015, 2009.
49. Phelps, C., C. J. Druffner, G. P. Perram, and R. R. Biggers, "Shock front dynamics in the pulsed laser deposition of $\text{YBa}_2\text{Cu}_3\text{O}_{7-x}$," *J. Phys. D*, vol. 40, no. 15, p.4447-4453, 2007.
50. Raymond, J. C., "Shock waves in the interstellar medium," *Astrophys. J. Suppl. Series*, vol. 39, pp.1-27, 1979.
51. Rogers, E. H., R. L. Williams, E. N. Frazier, D. K. Stone, K. C. Herr, R. M. Young, and R. G. Robbins. *Infrared spectrometry and radiometry of high-explosive detonations: the Los Alamos experiments*, Report Number ATR-82(7991)-1. Aerospace Corporation, Laboratory Operations, El Segundo, California, 1982.
52. Rothman, L. S., C. P. Rinsland, A. Goldman, S. T. Massie, D. P. Edwards, J.-M. Flaud, A. Perrin, C. Camy-Peyret, V. Dana, J.-Y. Mandin, J. Schroeder, A. Mccann, R. R. Gamache, R. B. Wattson, K. Yoshino, K. V. Chance, K. W. Jucks, L. R. Brown, V. Nemtchinov, and P. Varanasi. "The HITRAN Molecular Spectroscopic Database And HAWKS (HITRAN Atmospheric Workstation): 1996 Edition," *Journal of Quantitative Spectroscopy & Radiative Transfer*, 60(5):665–710, 1998.
53. Sakurai, A., "Blast Wave Theory," Mathematics Research Center, United States Army, University of Wisconsin, Madison, Wisconsin, MRC Technical Summary Report #497, 1964.
54. Sedov, L. I., *Similarity and Dimensional Methods in Mechanics*, 4th Edition, M. Holt, Ed. New York: Academic Press, 1959.
55. Smith, B. C. *Fundamentals of Fourier Transform Infrared Spectroscopy*. CRC Press, Inc., Boca Raton, Florida, 1996.
56. Spidell, M. T., "High speed thermal, radius, and emissivity measurements of ammonia nitrate detonation fireballs," Master's Thesis, AFIT/GAP/ENP/10-M14, Air Force Institute of Technology, 2010.
57. Spidell, M. T., J. Motos Gordon, J. Pitz, K. C. Gross, and G. P. Perram, "High speed radiometric measurements of IED detonation fireballs," in *Proc. of SPIE*, vol. 7668, 76680C-1-76680C-10, 2010.

58. Steinfeld, J. I. *Molecules and Radiation: An Introduction to Modern Molecular Spectroscopy*, 2nd Edition. Dover Publications, Inc., Mineola, New York, 1985.
59. Steward, B. J. *Reproducibility, distinguishability, and correlation of fireball and shockwave dynamics in explosive munitions detonations*. M.S. Thesis, AFIT/GAP/ENP/06-19, Department of Engineering Physics, Air Force Institute of Technology, 2006.
60. Taylor, G. I., "The formation of a blast wave by a very intense explosion," in *Proc. Royal Soc. A*, vol. 201, pp. 159-74, 1950.
61. Warren, T. W. *Characterization of detonation phenomena observed in high-speed, visible imagery*. M.S. Thesis, AFIT/GAP/ENP/06-20, Department of Engineering Physics, Air Force Institute of Technology, 2006.
62. Weil, J. C., B. Templeman, R. Banta, R. Weber, and W. Mitchell, "Dispersion Model Development for Open Burn / Open Detonation Sources", in American Meteorological Society 9th Joint Conference on Applications of Air Pollution Meteorology, 1996.
63. Weil, J. C., B. Templeman, and W. Mitchell, "Progress in Developing an Open Burn / Open Detonation Dispersion Model," Air and Waste Management Association, 1996.
64. Wilkinson, J., J. M. Lightstone, C. J. Boswell, and J. R. Carney, "Emission spectroscopy of aluminum in post-detonation combustion," *Shock Compress. Cond. Matt.*, vol. 955, no. 1, pp. 1271-1274, 2007.
65. Yngve, G. D., J. F. O'Brien, and J. K. Hodgins, "Animating Explosions," in *SIGGRAPH '00: Proceedings of the 27th annual conference on computer graphics and interactive techniques*, New York, pp. 29-36, 2000.
66. Zel'dovich, Y. B., and Y. P. Raizer, *Physics of Shock Waves and High-Temperature Hydrodynamic Phenomena – Vol. I*, From Second Russian Edition, W. D. Hayes and R. F. Probstein, Eds. New York: Academic Press, 1966.
67. Zyung, T., H. Kim, J. C. Postlewaite, and D. D. Dlott, "Ultrafast imaging of 0.532- μ m laser ablation of polymers: Time evolution of surface damage and blast wave generation," *J. Appl. Phys.*, vol. 65, no. 12, pp. 4548-4565, 1989.

Vita

Lieutenant Colonel Joe Motos Gordon was born in Manila, Philippines and grew up in the rice farming town of Minalabac in the Camarines Sur province of the Bicol region on the island of Luzon in the Philippines. He emigrated from the Philippines to Los Angeles, California in January 1979 and soon after attended William Northrup Elementary and Ramona Elementary schools in Alhambra, California. He graduated from San Gabriel High School in San Gabriel, California with the Class of 1988. He attended California State Polytechnic University Pomona and participated in the Air Force Reserve Officer Training Corps for two years before receiving an appointment to the United States Air Force Academy where he graduated with the Class of 1994 with a Bachelor of Science degree in Basic Sciences.

He served as a B-1B and F-16 aircraft maintenance officer for eight years with assignments to Rapid City, South Dakota, Kunsan Air Base, South Korea, and Phoenix, Arizona. He served the following eight years as a scientist and acquisitions officer with assignments to the Air Force Research Laboratory in Dayton, Ohio and Niceville, Florida. In May 2005, he completed his Master of Materials Engineering degree from Auburn University in Auburn, Alabama. In 2007, he was selected for the Ph.D. program in Applied Physics at the Air Force Institute of Technology in Dayton, Ohio. Upon graduation, he will work for the Defense Threat Reduction Agency in Albuquerque, New Mexico.

He is married and has one daughter.

REPORT DOCUMENTATION PAGE					Form Approved OMB No. 0704-0188	
<p>The public reporting burden for this collection of information is estimated to average 1 hour per response, including the time for reviewing instructions, searching existing data sources, gathering and maintaining the data needed, and completing and reviewing the collection of information. Send comments regarding this burden estimate or any other aspect of this collection of information, including suggestions for reducing the burden, to Department of Defense, Washington Headquarters Services, Directorate for Information Operations and Reports (0704-0188), 1215 Jefferson Davis Highway, Suite 1204, Arlington, VA 22202-4302. Respondents should be aware that notwithstanding any other provision of law, no person shall be subject to any penalty for failing to comply with a collection of information if it does not display a currently valid OMB control number.</p> <p>PLEASE DO NOT RETURN YOUR FORM TO THE ABOVE ADDRESS.</p>						
1. REPORT DATE (DD-MM-YYYY) 24-03-2011		2. REPORT TYPE Doctoral Dissertation		3. DATES COVERED (From - To) May 2007 - December 2010		
4. TITLE AND SUBTITLE Shock Wave Dynamics of Novel Aluminized Detonations and Empirical Model for Temperature Evolution from Post-Detonation Combustion Fireballs				5a. CONTRACT NUMBER 5b. GRANT NUMBER 5c. PROGRAM ELEMENT NUMBER 5d. PROJECT NUMBER 5e. TASK NUMBER 5f. WORK UNIT NUMBER		
6. AUTHOR(S) Gordon, J. Motos, LtCol, USAF				8. PERFORMING ORGANIZATION REPORT NUMBER AFIT/DS/ENP/10-S03		
7. PERFORMING ORGANIZATION NAME(S) AND ADDRESS(ES) Air Force Institute of Technology Graduate School of Engineering and Management (AFIT/EN) 2950 Hobson Way WPAFB OH 45433-7765				10. SPONSOR/MONITOR'S ACRONYM(S) DTRA/RD-CXTT		
9. SPONSORING/MONITORING AGENCY NAME(S) AND ADDRESS(ES) Mr. Donald Gross Defense Threat Reduction Agency (DTRA/RD-CXTT) 1680 Texas Street SE Kirtland AFB, NM 87117				11. SPONSOR/MONITOR'S REPORT NUMBER(S)		
12. DISTRIBUTION/AVAILABILITY STATEMENT APPROVED FOR PUBLIC RELEASE; DISTRIBUTION UNLIMITED.						
13. SUPPLEMENTARY NOTES						
14. ABSTRACT This research characterizes the blast wave and temperature evolution of an explosion fireball in order to improve the classification of aluminized conventional munitions based on a single explosive type such as RDX. A drag model fit to data shows initial shock velocities of 1.6-2.8 km/s and maximum fireball radii ranging from 4.3-5.8 m with most of the radii reached by 50 ms upon detonation. The Sedov-Taylor point blast model is fitted to data where a constant release (s=1) of energy upon detonation suggests shock energies of 0.5-8.9 MJ with blast dimensionalities indicative of the spherical geometry (n~3) observed in visible imagery. An inverse correlation exists between blast wave energy and overall aluminum content in the test articles. Using a radiative cooling term and a secondary combustion term, a physics-based empirical model is able to reduce 82 data points to five fit parameters to describe post-detonation combustion fireballs. The fit-derived heat of combustion has a 96% correlation with the calculated heat of combustion but has a slope of 0.49 suggesting that only half of the theoretical heat of combustion is realized. Initial temperature is not a good discriminator of detonation events but heat of combustion holds promise as a potential variable for event classification.						
15. SUBJECT TERMS Empirical model, temperature evolution, post-detonation combustion, aluminized high explosive, fireball, shock waves, blast waves, classification, Sedov-Taylor, Fourier-Transform Spectroscopy						
16. SECURITY CLASSIFICATION OF:			17. LIMITATION OF ABSTRACT		18. NUMBER OF PAGES	
a. REPORT U	b. ABSTRACT U	c. THIS PAGE U	UU		157	
			19a. NAME OF RESPONSIBLE PERSON Perram, Glen P., Professor, AFIT/ENP			
			19b. TELEPHONE NUMBER (Include area code) (937) 255-6565, ext 4504 (glen.perram@afit.edu)			

Reset